

Titre: Highly Multiplexable Open-Space Microfluidics
Title:

Auteur: Pierre-Alexandre F. Goyette
Author:

Date: 2021

Type: Mémoire ou thèse / Dissertation or Thesis

Référence: Goyette, P.-A. F. (2021). Highly Multiplexable Open-Space Microfluidics [Ph.D. thesis, Polytechnique Montréal]. PolyPublie. <https://publications.polymtl.ca/9913/>
Citation:

 **Document en libre accès dans PolyPublie**
Open Access document in PolyPublie

URL de PolyPublie: <https://publications.polymtl.ca/9913/>
PolyPublie URL:

Directeurs de recherche: Thomas Gervais
Advisors:

Programme: Génie biomédical
Program:

POLYTECHNIQUE MONTRÉAL

affiliée à l'Université de Montréal

Highly multiplexable open-space microfluidics

PIERRE-ALEXANDRE F. GOYETTE

Institut de génie biomédical

Thèse en vue de l'obtention du diplôme de *Philosophiae Doctor*

Génie biomédical

Décembre 2021

POLYTECHNIQUE MONTRÉAL

affiliée à l'Université de Montréal

Cette thèse intitulée :

Highly multiplexable open-space microfluidics

présentée par **Pierre-Alexandre F. GOYETTE**

en vue de l'obtention du diplôme de *Philosophiæ Doctor*

a été dûment acceptée par le jury d'examen constitué de :

Frédéric LESAGE, président

Thomas GERVAIS, membre et directeur de recherche

Yves-Alain PETER, membre

Govind KAIGALA, membre externe

ACKNOWLEDGEMENTS

This PhD was a long journey, and I would not have completed it without being surrounded by amazing peoples.

First of all, I would like to thank my research director Thomas Gervais. Thank you for putting your trust in me, from an undergrad internship in which nothing worked (already 7 ago!?!), to my PhD. Your support has greatly helped me develop myself as a researcher. You always made me feel like you care not only about my project, but also as me as an individual, which I am grateful for.

I was lucky to have incredible colleagues at the μ FO lab. Amélie, thanks for making sure the lab doesn't autodestruct on a day-to-day basis. Most importantly, thanks for welcoming me in the engineering physics department and presenting me to everyone. You made my integration so much easier. You have been of tremendous help throughout by PhD. Special thanks to Alexandre for teaching me all the 3D sorcery that he knew. You probably help me save months of troubleshooting. Étienne, I feel truly lucky that I collaborated with you throughout this project. I would not have the comprehension of open-space microfluidic that I have right now if it weren't for you. Thanks to Maude for trusting me to supervise her internship two years in a row (especially after working an entire summer on an impossible project). You truly deserved your "intern in chief" title. You completed some quality work that I would never have found time for. Thank you, Dina, for your cheerful attitude throughout our collaborations, especially during the pandemic when everything looked grim.

Sandryne, Étienne and Oscar, without our daily discussion, coffee break, brainstorming and complaining session, my PhD would not have been the same. I now hope that by some chance we become colleague once more in the future.

Thanks to all my friends (and more particularly those who love karaoke) for keeping my life interesting outside of work.

A special thanks to my family, especially my parents. I am grateful for your constant support. Your projects of megalomaniac dimensions are why I am not afraid of big adventures. Your elvish fabrication skills made me the tinkerer that I am.

Last but not least, thanks to the unique and incredible Catherine for her constant support with all my projects for the last 10 years. Everything feels better when you are around.

RÉSUMÉ

La manipulation de liquide est le fondement de toute recherche en sciences de la vie. Malgré son importance, la majorité de la manipulation de liquide est toujours basée sur le pipetage de fluides, une méthode datant de plus d'un siècle. La vague d'automatisation massive qui a débuté dans les années 70 a grandement augmenté le débit de tests pouvant être effectués. Cependant, à mesure que le débit de tests requis augmente et que les volumes des tests diminuent, le pipetage de fluides devient de plus en plus problématique. L'importance relative des forces en jeu change lorsque l'échelle du système diminue. La viscosité et la tension de surface deviennent importantes, ce qui entraîne une augmentation des imprécisions des fluides pipetés.

Une méthode pour se sortir de cette « tyrannie du pipetage » est d'utiliser des puces microfluidique, qui sont conçues pour manipuler des fluides à l'échelle submillimétrique dans des réseaux de microcanaux afin de réaliser diverses tâches expérimentales. Les systèmes microfluidiques se libèrent du paradigme des plaques de puits. En effet, ils sont plutôt basés sur des circuits fluidiques dans lesquels les expériences prennent place. Procéder à des expériences dans des systèmes microfluidiques vient cependant avec son lot de difficultés et de défis. Une grande partie des échantillons en sciences de la vie sont des surfaces ouvertes, que ce soit des cultures 2D en Pétri, des tranches de tissu ou des puces à protéines. Injecter des échantillons dans des systèmes microfluidiques nécessite des modifications majeures aux protocoles habituels. De plus, certains échantillons sont incompatibles avec les systèmes microfluidiques, par exemple certains types de cellules particulièrement sensibles aux contraintes de cisaillement.

Le champ de recherche de la microfluidique sur surface ouverte s'attaque à ces problématiques. La microfluidique sur surface ouverte englobe une multitude de systèmes conçus afin d'interagir avec des surfaces. L'idée générale derrière ces systèmes est de permettre le dépôt localisé de fluides sur des surfaces, et donc de ne pas nécessiter l'insertion des échantillons dans le système. Les systèmes de microfluidique ouverte tels que les sondes microfluidiques, qui sont l'inspiration principale derrière ce projet de recherche, ont déjà démontré leur potentiel en traitement de surface. Ils ont notamment été utilisés pour le marquage immunohistochimique localisé et la lyse cellulaire sélective. Cependant, alors que les dispositifs de microfluidique sur surface ouverte permettent habituellement le contrôle extrêmement précis de fluides sur une surface, il n'y a pour l'instant

aucune manière viable de paralléliser ces dispositifs. Cela nuit largement à leur adoption puisqu'ils ne peuvent pas être utilisés pour des expériences nécessitant un grand débit de test.

Cette thèse porte sur la conception, la fabrication et l'évaluation d'une nouvelle génération de systèmes microfluidiques sur surface ouverte qui peuvent être parallélisés et reconfigurés. Ces nouveaux dispositifs, les multipôles microfluidiques, fonctionnent en utilisant les mêmes principes que les sondes microfluidiques. Cependant, leur parallélisation permet d'augmenter le nombre de tests pouvant être effectués, et leur reconfiguration permet de les utiliser afin d'automatiser des expériences multi-étapes.

Dans cette thèse, une méthode de fabrication de multipôles microfluidiques compatible avec des systèmes de toute taille est présentée. Cette méthode couvre la totalité du procédé de fabrication, de la conception des dessins vectoriels à l'aide de scripts jusqu'à l'assemblage des systèmes. Les résultats démontrent qu'il est possible de produire des multipôles microfluidiques formés de plus de 300 ouvertures, avec une taille d'ouverture de 160 μm . Les résultats d'expérience démontrent que les multipôles fabriqués ne comportent pas de défauts et de déformations affectant significativement les motifs d'écoulement des fluides.

Dans une deuxième section de cette thèse, la manière la plus efficace afin de multiplexer et de reconfigurer des multipôles microfluidiques formés d'un petit nombre d'ouvertures est investiguée. Plusieurs architectures et concepts de multipôles sont étudiés et testés. Le grand potentiel de reconfigurabilité des multipôles est démontré, et un stroboscope chimique permettant le contrôle d'impulsion d'un réactif sur une surface est testé. Cette section de mon projet de recherche culmine avec l'automatisation d'un test immunologique à l'aide d'un multipôle microfluidique.

La dernière section de cette thèse porte sur l'élaboration d'un multipôle microfluidique hautement parallèle. La pièce centrale afin d'atteindre cet objectif consiste en l'élaboration d'une unité multipolaire modulaire, les pixels microfluidiques, pouvant paver une surface avec des zones de confinement indépendantes. Le résultat est l'afficheur chimique pixélisé, un sous-type de multipôle microfluidique. Ce type de système peut théoriquement être étendu à n'importe quel nombre de pixels, et des systèmes formés de 144 pixels ont été testés expérimentalement. Les afficheurs chimiques pixélisés, comme les autres multipôles, peuvent être reconfigurés afin de générer des séquences « d'images chimiques », ce qui permet l'automatisation d'expériences multi-étapes. Les

afficheurs chimiques ont la particularité de pouvoir être utilisés sur des surfaces immergées ou sèches, ce qui est habituellement impossible pour un multipôle microfluidique. Afin de démontrer cette possibilité, le traitement de surface de film plastique est effectué avec un afficheur chimique intégré dans un système « roll-to-roll ». Cette section de ma thèse se termine par une démonstration d'un afficheur chimique étant opéré uniquement par deux pompes à pression.

De manière générale, cette thèse a pour objectif de présenter une nouvelle approche de la microfluidique sur surface ouverte. Les multipôles microfluidiques présentés dans cette thèse sont les premiers dispositifs du genre étant reconfigurables, ainsi que les premiers permettant l'automatisation d'expériences multi-étapes. Les afficheurs chimiques pixélisés permettent une parallélisation qui est sans précédent en microfluidique sur surface ouverte.

ABSTRACT

Liquid handling is at the forefront of life science research. Despite its importance, it has been based on the same principle, the pipetting of fluids in wells, for over a century. The massive automation boom starting from the 70' has greatly increased the throughput that can be achieved. However, as the required throughput increased and the wells and reagent volumes are decreased further and further, pipetting fluids become more and more problematic. It is due to fluid viscosity and surface tension becoming more important as the scale of the problem decrease, leading to increased imprecision.

A way out of the “tyranny of pipetting” is to use microfluidic devices that are designed to operate with fluid at the microscale. Microfluidic systems break free from the well plate paradigm and are based on fluidic circuits in which the whole experiment usually takes place. However, processing samples in microfluidic systems come with its own challenges and limitation. A lot of standards samples in life science are surfaces, such as cultures in Petri, tissue slices or protein arrays. Moreover, injecting samples in a microfluidic system often require important modification to the experimental protocol. Some biological samples are also incompatible with microsystems, such as certain types of cells that are extremely vulnerable to shear stress.

The subfield of open-space microfluidic tries to address those limitations. Open-space microfluidics encompasses many systems that aim at processing and interacting with open surfaces. The general idea behind those systems is to allow the localized deposition of fluids directly on surfaces, and thus not require the insertion of the samples into the systems. Open-space microfluidic systems such as the microfluidics probe, which is the main inspiration being this project, have already demonstrated their potential in surface patterning. They have been successfully used for applications such as immunohistochemical staining and selective cell lysis. However, while the open-space microfluidic systems can precisely confine a fluid in an area, a viable method to parallelize those devices remains virtually inexistent. This greatly limit their adoption since they cannot be used for experiment requiring high throughput.

This research project revolves around the design, fabrication, and evaluation of a new generation of open-space microfluidic devices that are parallelizable and reconfigurable. These new devices, the microfluidic multipoles (MFMs), operate on the same principles as the previous microfluidic

probe. However, their parallelization allows for an increase in throughput, and flow pattern reconfiguration open the possibility to perform multistep experiments.

In this thesis, a fabrication method for MFMs of any size, from a few apertures to several hundreds of apertures is presented. This method covers the whole process, from the script-assisted CAD design to the assembly of multipoles. The results demonstrate the possibility to fabricate MFMs with as many as 313 apertures with a size as small as 160 μm . Experiment have demonstrated that MFMs could be reliably printed without defects and warping that would deform the flow. This fabrication method is, furthermore, simple, inexpensive and versatile.

A second section of this thesis investigate the best way to parallelize and reconfigure MFMs that are comprised of a limited number of apertures. Different multipole architectures are proposed and tested. The high reconfiguration potential of MFMs is demonstrated, and a chemical stroboscope allowing the spatiotemporal pulse of chemicals on a surface is presented. This part of my work culminates with the automation of an immunofluorescence assay, which demonstrates the potential use of MFMs to automatize long-term multistep experiments.

The last section of my work is an all-out attempt at highly parallel open-space systems. This section revolves around the use of modular MFM units, the microfluidic pixels, to tessellate whole surfaces in independent confinement areas. This results a Pixelated Chemical Display (PCD), a subtype of MFM. This device architecture can theoretically be expanded to any size and was experimentally tested for systems formed of up to 144 pixels. PCDs, just like other MFMs, can be reconfigured to create sequences of “chemical images”. That allows them to be used to automatize multistep experiments. Moreover, they can be made compatible with dry surfaces, which is not expected from an open-space microfluidic system. We demonstrated that capability by patterning dry plastic films in a custom roll-to-roll setup. This section of my thesis end with a demonstration of how to operate large PCDs using only two pressure pumps.

Overall, this thesis aims at offering a new way of approaching open-space microfluidics. MFMs presented in this thesis are the first reconfigurable microfluidic multipole, and the first open-space system to be used to automate multistep experiments. Moreover, PCDs presented in this work offer a parallelization potential which is unprecedented in open-space microfluidics.

TABLE OF CONTENTS

ACKNOWLEDGEMENTS	III
RÉSUMÉ.....	V
ABSTRACT	VIII
TABLE OF CONTENTS	X
LIST OF TABLES	XIV
LIST OF FIGURES.....	XV
LIST OF SYMBOLS AND ABBREVIATIONS.....	XXII
LIST OF APPENDICES	XXIV
CHAPTER 1 INTRODUCTION.....	1
1.1 Motivation.....	1
1.2 Research objectives.....	2
1.3 Dissertation organisation.....	4
CHAPTER 2 LITTERATURE REVIEW	5
2.1 Liquid handling automation	5
2.1.1 System densification	5
2.1.2 Liquid handling method	6
2.1.3 Liquid handling limitations	6
2.1.4 Microfluidics	7
2.2 Open-space microfluidics.....	9
2.2.1 Chemistode	10
2.2.2 Atomic force microscopy-based methods.....	11
2.2.3 Multiphase systems	11
2.2.4 Micro and nanopipette.....	12

2.2.5	Microfluidic patterning	13
2.2.6	Inkjet printer	14
2.2.7	Microcontact printing	14
2.2.8	Microfluidic probe & multipole	15
2.3	Direct 3D printing of microfluidic system	21
2.3.1	3D printing methods	22
2.3.2	Direct printing using SLA	23
2.4	Microfluidic multiplexor	24
CHAPTER 3	PROJECT OVERVIEW	26
3.1	The microfluidic multipole	26
3.1.1	The microfluidic probe vs. the microfluidic multipole	26
3.1.2	Microfluidic multipole basis	26
3.1.3	MFM in this thesis	27
3.2	Multipolar microfluidic theory	29
3.2.1	Potential flows	29
3.2.2	Convection-diffusion and conformal mapping	31
CHAPTER 4	MICROFLUIDIC MULTIPOLES AND PIXELATED CHEMICAL DISPLAY FABRICATION	35
4.1	CAD design	35
4.2	3D printing and post-processing	38
4.3	3D Printed microfluidic multipoles results & discussion	39
CHAPTER 5	MULTIPLEXABLE AND RECONFIGURABLE MICROFLUIDIC MULTIPOLES	44
5.1	Scanning device limitations	44

5.2	First explorations of the MFM configurations	45
5.3	Microfluidic multipole reconfiguration.....	49
5.4	Reconfigurable MFM immunofluorescent assay	53
5.5	Discussion	56
CHAPTER 6 ARTICLE 1 : PIXEL-BASED OPEN-SPACE MICROFLUIDICS FOR VERSATILE SURFACE PROCESSING.....		58
6.1	Background information	58
6.2	Abstract	59
6.3	Significance Statement.....	59
6.4	Introduction	60
6.5	Results and discussion.....	61
6.5.1	Pixelized chemical display concept.....	61
6.5.2	Display operation	63
6.5.3	Display stability.....	65
6.5.4	Display reconfigurability.....	67
6.5.5	Roll-to-Roll applications	69
6.6	Conclusion.....	70
6.7	Materials and Methods	71
6.7.1	PCDs fabrication and operation	71
6.7.2	Experimental measurements	72
6.7.3	Simulations.....	72
6.7.4	Stability Analysis	73
6.7.5	Roll-to-roll experiment.....	73
6.8	Data Availability	74

6.9	Acknowledgments.....	74
CHAPTER 7	PRESSURE-BASED PCD.....	75
7.1	Comparison between syringe pumps and pressure pumps.....	75
7.2	Pressure-based PCD design.....	77
7.3	Results & discussion	79
CHAPTER 8	GENERAL DISCUSSION.....	81
8.1	Discussion on project objectives and results.....	81
8.1.1	Multipolar microfluidic system fabrication.....	81
8.1.2	Small Size reconfigurable multipoles	83
8.1.3	Scalable multipole and large scale pixelated chemical display.....	85
8.2	Limitations and recommendations	88
8.2.1	Inherent limitation of hydrodynamic flow confinement	88
8.2.2	PCDs and MFMs are not compatible with thick tissues.	89
8.2.3	Fabrication method.....	89
8.2.4	Bubble nucleation.....	90
8.2.5	Fluid compatibility and clogging	91
8.2.6	Total reconfiguration vs minimum useful reconfiguration.	92
8.2.7	Checklist to access future experiment viability.....	92
CHAPTER 9	CONCLUSION.....	94
9.1	Multiplex open-space microfluidics and the tyranny of numbers.....	94
9.2	Outlook.....	95
REFERENCES.....		97
APPENDICES.....		108

LIST OF TABLES

Table 3-1: Example of conformal transformation that can be applied to the microfluidic dipole solution.....	34
Table 7-1 Comparison between system operated with syringe pumps and pressure pumps	77
Table 8-1 Comparison between MFM fabrication methods. The most limiting characteristics of each method are highlighted in red.	82
Table A-1. Microfluidic multipole transformation list.....	108
Table C-1 α correction for a constant pattern width using the rMFM	109

LIST OF FIGURES

- Figure 2.1 Micrograph of an integrated fluidic circuit (IFC) comprised of 256 individually addressable microchambers. This system can be operated using only 18 connections to the outside world. Reproduce with permission from Thorsen & al., *Science* (2002)¹⁰.8
- Figure 2.2 A droplet microfluidic on-chip viability assay. Schematic and micrograph of the system. A) Droplets with cells and dye are generated. B) Droplets are merged. C) The content of the droplets is mixed. D) Delay line. E) Signal measurement. Reproduce with permission from Brouzes & al. *PNAS* (2009)³³. Copyright 2009, National Academy of Sciences.....9
- Figure 2.3. The Chemistrode. A) Schematic of the chemistrode operation. B) Close-up schematic of the tip of the chemistrode. C) Experimental bright-field micrograph of a stimulus droplet wetting a surface and being aspirated. Reproduced from Chen & al. *PNAS*, (2008)³⁵. Copyright 2008, National Academy of Sciences.11
- Figure 2.4: Aqueous two-phase system. A) Schematic of a two-phase system. B) Brightfield and fluorescent micrographs of a two-phase system used to write UMICH on a surface using FITC-labeled Dextran on a PEG immersed surface. Reprinted with permission from Tavana & al., *Nature Materials*, (2009)¹²..... 12
- Figure 2.5. Voltage driven nanopipette for reagent delivery. Nanopipette operation for A) no delivery, B) reagent delivery. Reproduced with permission from Bruckbauer & al., *Biophysical Journal* (2007)⁴⁴..... 13
- Figure 2.6 : Folch’s research group parallel chemosensitivity assay chip. Reprinted with permission from Chang & al. *Lab Chip* (2014)⁵⁵. 14
- Figure 2.7 : Microfluidic probe working principle. The MFP is held over the surface to pattern. By having an injection flow rate lower than the aspiration flow rate, a confinement area is created. a) side view. b) bottom view. Reprinted with permission from Juncker & al. *Nature Materials*. (2005)¹³..... 16
- Figure 2.8 : The hierarchical MFP and its mode of operation. Grey represents immersion medium. Green and blue respectively represent the fluid of interest and a shaping fluid. A microfluidic dipole (a). A hierarchical MFP working in nested mode (b) and pinched mode (c). Reprinted

- with permission from Delamarche & al. *Open-Space Microfluidics: Concepts, Implementations, and Applications*, Chapter 2, Wiley VHC, (2018)⁶³.....18
- Figure 2.9 Flow lines and experimental micrograph of a dipole array, a) without stabilization apertures, b) with stabilization aperture. Reproduced with permission from Taylor & al. *Langmuir* (2016)¹⁸.....19
- Figure 2.10 : A microfluidic quadrupole seen as a 2D electrostatic problem. A) Electrical field lines around four punctual charges positioned as a quadrupole. b) Fluorescent micrograph of fluorescent tracers under a microfluidic quadrupole showing the experimental flow lines. Modified and reproduced with permission from Quasaimeh & al. *Nat. Commun.* (2011)⁶².20
- Figure 2.11 Multilayered MFP fabrication protocol used by IBM research group. (a) Schematic of a multilayered MFP head. (b) Illustration and schematic of the fabrication process. A DRIE etched silicon wafer is bonded to glass a wafer using anodic bonding. Reproduced with permission from Kaigala & al. *Langmuir* (2011)⁵⁶.....21
- Figure 2.12 A DLP-SLA 3D printer. The image is formed by reflecting the UV light from a light source (generally UV led) on a digital micromirror device (DMD). The image is then magnified by a lens. For each layer, the image is projected, then the stage is moved up by the layer thickness before the subsequent layer is projected. Reproduced from 3D printing industry [<https://3dprintingindustry.com/>].23
- Figure 3.1 MFM Schematic. A) A 3D schematic of a MFM held over a surface. B) Side cut of an MFM. Aspirations and injections are streaming continuously, which result on stationary patterns on the surface.....27
- Figure 3.2 Small reconfigurable MFM and PCD. The top row is a axisymmetric MFM and the bottom row is a square-pixel PCD. a), d) Micrograph of the system. b), e) Theoretical flow lines. c), f) Fluorescent micrograph of the surface patterning. Scale bars represent 500 μm28
- Figure 3.3 MFM streamline. (a-d) Example of MFM streamline generated using the superposition of the velocity field from every aperture. (e-h) Comparison with fluorescent micrographs. (a,e) Dipole. (b,f) Quadrupole. (c,g) Rotationally symmetric MFM. (d,h) 12-aperture MFM. Figure

from Goyette & al. Nat. Commun. (2019) ⁹² . License CC BY 4.0 http://creativecommons.org/licenses/by/4.0/	30
Figure 3.4 Concentration profile from the theoretical convection-diffusion model. Concentration profile for a) a semi-infinite obstacle, b) a microfluidic dipole, c) a 4 petal rotationally symmetric MFM, d) a microfluidic quadrupole. Figure modified from Goyette & al. Nat. Commun. (2019) ⁹² . License CC BY 4.0 http://creativecommons.org/licenses/by/4.0/	33
Figure 3.5 Solution of the conformal transformations from table 3-1 applied to a dipole. Concentration mapping for (a) the quadrupole transformation, (b) the flower multipole transformation, (c) the polygonal multipole transformation, (d) the impinging flows transformation. Modified and reproduced with permission from Boulais & al. Physics of Fluids (2020) ⁹³	34
Figure 4.1 Differences in CAD complexity. a) User designed 9-aperture “Flower” microfluidic multipole. b) Script assisted model of an 81-aperture PCD.....	35
Figure 4.2 Script-assisted CAD design visual protocol.	36
Figure 4.3 a) Model of a PCD with integrated manifold made with OpenSCAD, a script-only CAD software. Notice that the 9:1 manifold (in red) are repeated and used at two different scale. b) The PCD design from a) 3D printed by Nordin's group in BYU.....	37
Figure 4.4 Asiga Pico 2 HD 3D printer.....	38
Figure 4.5 3D printed MFM. a) an 8-petal "flower" MFM. b) An 81-aperture PCD. c) A 313-aperture PCD. Scale bar represents 1 mm.....	39
Figure 4.6 MFMs using a positioning system and autoalignment spacers. a) A 3D printed microfluidic quadrupole compatible with a positioning system. b) Positioning system slider and probe holder. c) Microfluidic Probe positioning systems. d)-f) 12-aperture MFM with autoalignment spacers.	40
Figure 4.7 PIV measurements of the flow under a 3D printed microfluidic dipole. a) Potential flow streamlines under a microfluidic dipole. b) Average of 200 PIV measurements presenting the orientation and magnitude of the flow under the dipole. c) Fluorescent beads streamlines. Scale bar represents 500 μm	41

- Figure 4.8 a) Comparison between the envelope of a microfluidic quadrupole for experimental data, a 3D finite element simulation and the analytical solution based on potential flows. Aspiration to injection ratio (α) equal to 3. b) 3D printed microfluidic quadrupole with different aspirations to injection ratio. Scale bar represents 500 μm42
- Figure 5.1 a) Schematics of a fixed MFM setup. The MFM is precisely positioned over the surface with a gap controlled by the auto alignment spacers. b) Picture of the experimental setup with a holder and a MFM clamped on an inverted microscope. Figure modified from Goyette & al. Nat. Commun. (2019)⁹². License CC BY 4.0 <http://creativecommons.org/licenses/by/4.0/>.46
- Figure 5.2 Comparisons between the theoretical model and experimental results for different cross-sections of a microfluidic dipole. How each cross-section maps to the experimental image is illustrated in a), while b)-f) show the comparison of experimental and theoretical concentration. The diffusive species used is fluorescein. (Figure from supplementary information, of Goyette & al. Nat. Commun. (2019)⁹². License CC BY 4.0 <http://creativecommons.org/licenses/by/4.0/>).47
- Figure 5.3 Experimental setup and side-by-side comparison between theory and experiments. For each subfigure, the top half represents the theoretical concentration profile, and the bottom half is a fluorescent micrograph of an MFM injecting a fluorescent dye. a) Microfluidic dipole. b) Microfluidic quadrupole. c) Polygonal multipole d) 4-petal axisymmetric “flower” multipole e) 8-petal axisymmetric “flower” multipole f) Asymmetric impinging flows. $Pe \sim 100$. Scale bars represent 500 μm . Figure modified from Goyette & al. Nat. Commun. (2019)⁹². License CC BY 4.0 <http://creativecommons.org/licenses/by/4.0/>.48
- Figure 5.4 Microfluidic multipole generation from the conformal transform $\omega = z^{1/n}$. a) A microfluidic multipole. b) Using the aspiration as origin, a 2-petal axisymmetric “flower” multipole can be generated from the dipole. c) A 4-petal axisymmetric “flower” multipole. d) Using the injection as origin, microfluidic polygons can be generated. e) Polygonal MFM.49
- Figure 5.5 Reconfigurable multipole. Theoretical streamlines (a–b) and fluorescence micrograph (c–d). Positive and negative signs represent injection and aspiration apertures. a), c) MFM with rotational symmetry. b), d) 12-aperture MFM with translational symmetry. Scale bars

represent 500 μm . Figure modified from Goyette & al. Nat. Commun. (2019)⁹². License CC BY 4.0 <http://creativecommons.org/licenses/by/4.0/>.50

Figure 5.6 Microfluidic multipole devices. a) Fluorescence micrograph showing the confinement pattern of a rMFM device. b) Graph representing the periodic exposure to reagents for each confinement area of a rMFM used as a chemical stroboscope. c) Fluorescence micrographs showing 28 different confinement patterns made with a 12-aperture tMFM during a single experiment lasting less than 2 min. Scale bar represents 500 μm . Figure from Goyette & al. Nat. Commun. (2019)⁹². License CC BY 4.0 <http://creativecommons.org/licenses/by/4.0/>.52

Figure 5.7 Fluorescence micrographs showing 6 different confinement patterns made with a 12-aperture tMFM during an experiment lasting 30 seconds. Scale bar represents 500 μm53

Figure 5.8 Immunoassay experiments using a staggered tMFM microfluidic multipole. a)–c) Workflow of an immunofluorescence assay using a MFM. a) Antigen incubation. The device is used as a 6-petal rMFM to incubate 6 different concentrations of antigen on the capture antibodies. b) Detection antibodies incubation. The corner apertures are then used to expose the previous areas with detection antibodies. c) Wash. A washing buffer is injected by the last aperture. d) Resulting micrograph of the detection antibody on the glass slide. e) Experimental binding curve of the immunoassay. Error bars represent the standard deviation over 6 spots. Figure from Goyette & al. Nat. Commun. (2019)⁹². License CC BY 4.0 <http://creativecommons.org/licenses/by/4.0/>.....55

Figure 6.1 Pixelated Chemical Display concepts and schematic. a) Schematic presenting an 81-aperture square-pixel PCD. The PCD is held over a sample. Lines on the surface represent the flow lines. b) Theoretical flow lines in an array of microfluidic pixels under a PCD. Positive and negative signs represent injection and aspiration apertures, respectively. c) Side view cut schematic of a PCD. The PCD is maintained at a fixed height over a surface with the help of spacer pillars. Fluids are injected and reaspirated within the shallow gap formed between the surface and the device.63

Figure 6.2 Experimental PCDs. Fluorescent micrograph at the tip of a) a square-pixel PCD, b) a triangle-pixel PCD, and c) a hexagonal-pixel PCD. Fluorescent micrographs of a locally-confined, globally unconfined d) square-pixel PCD, e) triangle-pixel PCD, and f) hexagonal-

pixel PCD. g) Micrograph of a 3D-printed 144-pixel PCD device. h) Fluorescent micrograph of a 144-pixel PCD. All the scale bars represent 1 mm.65

Figure 6.3 Effect off clogged apertures. (a) Simulation of a 19x19 square-pixel PCD with a clogged aperture. The clogged aperture is pointed by the red arrow. (b) Absolute error resulting from the clogged injection. (c) Graph of the error generated at each pixel border by a clogged injection in function of the position. Error were measured on the red line from (b). The error ε follows a decreasing power function of equation $\varepsilon = (1.3 \times 10^7)d^{-1.64}$, where “d” is the distance in pixel. The error (ε) is the integral of errors peak intensity over position. (d) Fluorescent micrograph of a hexagon-pixel PCD. (e) The hexagon-pixel PCD from (d) with an injection turned off. (f) Absolute errors resulting from the injection turned off. Scale bars from (d-f) equal 1 mm.66

Figure 6.4 PCD reconfiguration. a) Fluorescence micrographs of PCD reconfigured to sequentially write “P”, “O”, “L”, and “Y”. Scale bar represents 1 mm. b) Schematic of the pumps, valves and manifolds used to perform the PCD reconfiguration from a).....68

Figure 6.5 Roll-to-roll processes using a PCD. a) Schematic of the roll-to-roll setup used for the biopatterning of proteins and silver thin film deposition. For the bio-patterning, the sensitization bath was removed, and the film went directly from the feed roll to the alignment rolls b) Fluorescent micrograph of three consecutive patterns of BSA-Alexa 555 and BSA-Alexa 488 proteins on a polystyrene film in a roll-to-roll process. c) Fluids schematic of the deposition process of a E-shape silver pattern on a PET film. d) Micrograph of an E-shape silver pattern on a PET film roll. All scale bars represent 500 μm70

Figure 7.1 Pressure-based PCD. Fluidic circuit schematic of a 12-pixel (4 groups) pressure-based PCD operating with two pressure regulators. The pump system is based on a pressure generator that feeds the inlet pressure of the two-pressure regulator. The aspirations are all connected together through a manifold. Four reagent vessels are connected to a single pressure regulator. Both for the aspirations and the injections, the tubes in between the pressurized flask and the PCD serve as precision hydraulic resistors to match the flow rate.....78

Figure 7.2 Fluorescent micrograph of pressure-based PCD. A) A 9-pixel PCD (3 groups of 3 pixels). B) A 12-pixel PCD. This PCD is organized as 4 groups of 3 pixels and uses the manifolds presented in Figure 7.1.....80

LIST OF SYMBOLS AND ABBREVIATIONS

2PP	Two photon polymerisation
AFM	Atomic force microscopy
ALH	Automated liquid handling
BSA	Bovin serum albumin
CAD	Computer assisted design
COVID-19	Coronavirus disease 2019
DLP	Digital light processing
DMD	Digital micromirror device
DNA	Deoxyribonucleic acid
DPN	Dip pen lithography
DRIE	Deep reactive ion etching
ER	Estrogen receptors
FDM	Fused filament deposition
FITC	Fluorescein isothiocyanate
HCl	Hydrochloric acid
HD	High definition
HER2	Receptor tyrosine-protein kinase erbB-2
HFC	Hydraudynamic flow confinement
IFC	Integrated fluidic circuit
IHC	Immunohistochemical
KOH	Potassium hydroxide
LCD	Liquid cristal display

LOD	Limit of detection
MFM	Microfluidic multipole
MFP	Microfluidic probe
PBS	Phosphate-buffered saline
PCD	Pixelated chemical display
PCR	Polymerase chain reaction
PDMS	Polydimethylsiloxane
PEG	Polyethylene glycol
PET	Polyethylene terephthalate
PIV	Particle image velocimetry
PJ	Polyjet
PR	Progesterone receptor
PS	Polystyrene
RGB	Red green blue
rMFM	Rotationally symmetric multipole
SLA	stereolithography
tMFM	Translationally symmetric MFM
UV	Ultraviolet

LIST OF APPENDICES

Appendix A	List of conformal transforms and the link between different geometries of microfluidic multipoles	108
Appendix B	Chemical stroboscope flow rate correction	109
Appendix C	Reconfigurable MFMs extended dataset	110
Appendix D	immunofluorescent background comparison with a null concentration confinement area	112
Appendix E	Supplementary Information, Pixel-based open-space microfluidics for versatile surface processing	113
Appendix F	List of contribution.....	130

CHAPTER 1 INTRODUCTION

1.1 Motivation

Liquid handling is at the heart of any life science research. From cell biology to pharmacology, hundreds of types of assays exist, and most depend on fluid manipulations. However, despite its importance, most of the liquid handling is still performed using pipettes, the same basic tool used since Louis Pasteur era¹. The automation boom we have seen in the last 40 years has greatly increased the liquid handling throughput^{2,3}. However, as these systems originally built to operate at the macroscale are modified to work with increasingly small volume, challenges arise^{4,5}.

Many researchers have postulated that the future of multiplex liquid handling will come from microfluidics^{6,7}. Microfluidics theoretically allows for faster and more efficient reaction due to the small diffusion length used in microsystems⁸. Some research in high-throughput microfluidics, notably high-throughput droplet microfluidics⁹ and integrated fluidic circuits (IFC)¹⁰ are showing the potential of microfluidics for next generation large-scale liquid handling automation.

However, current microfluidic systems lack compatibility with some assays. Classic microfluidic systems based on circuits of channels and chambers generally require the sample to be inserted in the systems. It is problematic as a lot of samples used in life science are planar samples, like Petri dishes, tissue slices or protein and DNA arrays. In some case, the sample can't be injected in the system (such a shear stress sensitive cells). In other cases, it would require the microdissection of the sample, which would lead to the loss of spatial information. Finally, it sometimes greatly impacts the standard assay protocols and add a barrier to the adoption of microsystems.

A subfield of microfluidics, open-space microfluidics, has been working on devices that can operate on open surfaces. Different ideas emerged, like the use of modified channeled atomic force microscopy (AFM) tips to interact with cells¹¹, or the use of multiple aqueous phases¹². One of the most versatile and prolific method presented is the microfluidic probe¹³ (MFP). Since their introduction in 2005 by David Juncker and IBM research, over 60 papers have been published on this device. MFPs have been used to process planar samples in experiments such as protein biopatterning¹³, immunohistochemical staining^{14,15}, organotypic slice perfusion¹⁶ and single cell lysis and analysis¹⁷, amongst many more. These devices use hydrodynamic flow confinement (HFC) to precisely control fluid under their tip. To address large surface areas, the MFPs are

scanned over the surfaces¹³. Despite the amount of work on MFP in the last decade and a half, MFPs remain extremely limited in terms of their multiplexing potential¹⁸. Moreover, scanning MFPs can be used to perform experiments with time scale in the seconds, but they are incompatible with long lasting or parallelized experiments.

The objective of this thesis is to bridge the gap between the parallelization potential of classic microfluidic system and open-space microfluidic systems. Using the microfluidic probe as a starting point, new system architectures are designed and tested with the goal in mind to create parallelizable open-space devices that can perform both short- and long-term assays on open surfaces. The devices presented in this thesis are microfluidic multipoles (MFMs), a generalization of the microfluidic probe that operate on the same flow principles. However, MFM can be extended to any number of flow apertures. Two mains approach to achieve MFM parallelization and reconfiguration are investigated. The first one focuses on architecture adapted to small MFMs and their use in multistep experiments based on confinement area overlap. This approach yields MFMs that are well adapted for experiments requiring a limited multiplexing and a fast dynamic. In a second phase, a scalable MFM architecture, the Pixelated Chemical Display (PCD) is presented. PCDs are highly multiplexable open-space systems, which allows the tessellation of surfaces in hundreds of independent fluid confinement areas. They are extremely stable and can be reconfigured. PCDs offer a new liquid handling alternative to both robotic pipetting stations and closed microfluidic systems.

1.2 Research objectives

This dissertation main objective is **to develop new surface compatible microfluidic devices that are reconfigurable, parallelizable, and automatable**. These new systems should be contactless, compatible with immersed surface and compatible with solutions and reagents usually used in life science. Moreover, the shear stress to which they exposed the sample should be low enough to be compatible with cell tissues. This thesis aims at covering both the fabrication, the design, and the characterization of those devices. This project can be divided in three main research objectives.

1. Develop a robust and versatile method to fabricate microfluidic multipoles.

The first objective is to develop a reliable fabrication method with a fast turnaround rate. This method should also be versatile and allows the testing of various MFM designs. While not having the scientific interest of the second and third objective, it is the workhorse of this project as it is essential to any experimentation on microfluidic multipoles. This objective can be divided in three steps. To begin, an efficient method to generate the computer assisted drawing of MFMS is developed. This is followed by the development of a fabrication method based on stereolithography printing. Finally, 3D printed MFMs are evaluated.

2. Design, test and characterize multiplexed open-space systems of limited size (<12 apertures).

The second and third objectives are both at the core of this research. These objectives focus on the conception and evaluation of parallelizable open-space microfluidic devices. However, the second objective is limited to the design and evaluation of MFM architectures that are adapted to small reconfigurable MFM with a limited number of aperture (<12). Creating systems that allow a certain degree of multiplexing and reconfiguration while remaining the simplest possible is the goal. This objective aims at more than simply designing small-scale MFMs. MFM architectures are optimized to maximize the multiplexing and reconfiguration. Moreover, reconfigurable MFM dynamics are evaluated. The last major sub-objective is the showcase of a long-term multistep experiment using a small reconfigurable MFM.

3. Design, test and characterize a scalable and highly parallelizable open-space microfluidic system.

The third objective is the design, operation, and characterization of highly multiplexable open-space microfluidic devices. For this objective, finding a scalable architecture that can be used independently of the microfluidic multipole size is the key. This part of my research focus on scalable devices that allows the tessellation of a surface into a hundred of independent fluid confinement areas. After a large-scale architecture is developed, its use to produce large-scale reconfigurable MFM systems is demonstrated.

1.3 Dissertation organisation

This thesis starts with a literature review on liquid handling automation, open-space microfluidics and the direct 3D printing of microfluidic systems (Chapter 2). It is followed by a brief project overview that explains the MFM basics as well as cover multipolar flow theory (Chapter 3). Chapters 4 to 7 are the heart of this research project. Chapter 4 covers the fabrication of MFMs. Chapter 5 presents the small reconfigurable MFMs. Chapter 6 describes the content of my third published article. It covers the design, fabrication and test of pixelated chemical displays, large scalable open-space microfluidic devices. Chapter 7 presents how to design pixelated chemical displays that rely on pressure pumps, and the implications that result from it. Chapter 8 serves as a general discussion and chapter 9 presents the conclusion. Six appendices follow this thesis. Appendix A cover the conformal maps that can be used to generate different geometries of MFMs. Appendix B, C and D present some detailed information related to small reconfigurable MFM experiments. Appendix E is the supplementary information of my PNAS article presented in chapter 6. Appendix F is a list of the publications that resulted from this thesis.

CHAPTER 2 LITTERATURE REVIEW

2.1 Liquid handling automation

Liquid handling automation have become ubiquitous in life sciences, and an essential component in drug screening and development. Drug screening can require the testing of thousand to hundreds of compounds to find one considered to be sufficiently active^{3,19}. While drug screening is at one end of the spectrum, it is far from the only domain which benefit for liquid handling automation. A lot of life science process and assay are extremely time intensive, from PCR to immunoassay. The Covid-19 is a beautiful example of how liquid handling automation have become essential. In March 2021, over 800 000 COVID-19 test were performed each day in the USA, thanks to automated liquid handling²⁰.

2.1.1 System densification

The need for high throughput system has led to an intense densification of the well plates. Decreasing the volume of the assay importantly decreased the cost of assays. In less than 50 years, assay volume have gone from 250 μL in a 96-well plate to 2.2 μL in a 3456-well plate¹⁹. It would however be a mistake to consider the transition from 96-well plate to 3456-well plate as a simple miniaturisation. Multiple factors are changing, such as the surface to volume ratio. Smaller well are a lot more vulnerable to surface effects (adhesion, surface reactions, fouling) and evaporation, which sometimes lead to edge effect (side well plate are more affected by evaporation than well in the center of the plate)⁵. Washing steps (especially with non-homogenous solution) are increasingly difficult to achieve as the well volume diminishes⁵. Risk of damaging sample or cell cultured in a well during washing steps also increases as the well size is decreased²¹. Furthermore, pipetting become more and more inefficient, inaccurate, and inappropriate as volumes become smaller. The impact of decreasing well sizes brings us two to simple conclusions. First, it is not possible to decrease well volume indefinitely, as major physical constraints will arise. Secondly, the early idea that liquid handling is a mere robotization of human movement is unsuitable and limitative. In an excellent letter to the editor, McClymont and Freemont claims that “[...] lab automation isn’t anthropomorphic²²”. The methods used by person to work with 96-well plate might not adapted at all to robotised high throughput solutions.

2.1.2 Liquid handling method

While liquid handling might look simple (after all its all about taking fluid from a reservoir and put it in an other reservoir) and is often overlooked, a study found that different liquid handling method (in this case between pipette vs acoustic methods) used during drug screening could lead to significantly different results^{1,23}. Considering that liquid handling is the backbone of most biomedical research, understanding the implication of each liquid handling method is of utmost importance.

Pipette-based methods are the most known and used, but they can be problematic for fluids with low surface tension. Moreover, imprecision from the pipette action increases as the volume of the assays decreases. Pipette-based methods are also prone to foaming²¹. These limitation lead to research on other delivery method, such as acoustic droplet ejection. Systems using this method (such as Labcyte echo) use a transducer to project nanodroplet of liquid from a supply well plate to a test well plate (which is positioned upside down during this operation) using focused soundwaves^{24,25}. Some systems can project droplets as small as 2.5 nL. No contamination is possible in between well since no tip or nozzle is shared. Inkjet based methods form another liquid handling option²⁶. Inkjet systems with different actuation mechanism exist, be they thermal, piezoelectric, acoustic or electrostatic in nature²⁷. Each of these methods have different characteristics and compatibility with different solvents, but they all allow the deposition of droplet in the hundreds of picoliter range. Both acoustic droplet injection and inkjet systems allow an unprecedented precision in reliability in high throughput liquid handling, however, neither can remove fluid from a well, and both these still depend on tip-based solution for washing steps.

2.1.3 Liquid handling limitations

Despite advances in automated liquid handling, available solutions remain limited. Commercially available solutions are mostly compatible with well plates, which can be limitative. There is no possibility to create chemical gradient. Rapid change of reagent, or pulse of reagent are also impossible due to slow washing steps. Moreover, robotic liquid handling system are full of moving parts, and become increasingly complicated as the well plate becomes denser. Another problem is that while high throughput and parallelisation is the goal, using a tip or nozzle approach to move

fluid remains an inherently serial process. More and more nozzles and heads can be added, but it is impossible to get a purely parallel and scalable approach.

While traditional liquid handling automation systems are impressive, it seems clear that a change of paradigm is needed to allow further miniaturisation, increase in throughput and increased flexibility. Microfluidic offer a way out of this “tyranny of pipetting”, as described by Stephen Quake in his address at the 2017 Nobel Symposium⁷.

2.1.4 Microfluidics

Microfluidics is the science and technology of fluid manipulation at submillimeter scale. Fluids at the micrometer scale behave differently than at the macroscopic scale. The scaling laws are such that some forces like viscosity and surface tension, which are normally negligible at macroscale, become dominant at the microscale²⁸. Whereas the pipette and well-based automated systems were designed at the macroscale and are affected by this change of dominant forces, microfluidic system are built to operate at this scale. Microfluidic system usually requires minute amount of reagent and sample and offer faster reaction dynamic due to the shorter transport times⁸. Multiple researchers are seeing microfluidic systems as the solution toward a new generation of liquid handling system^{6,7}.

Microfluidic have evolved into plenty of subfields with various goals, from point of care diagnostics to high-throughput analysis. This literature review will only focus on systems designed for high throughput applications. Arguably, the most notorious work in multiplex microfluidic is the design and fabrication of PDMS pressure valves²⁹ (or Quake valves) and their integration into integrated fluidic circuits (IFCs)¹⁰. Todd Thorsen’s original circuit contained over three thousand valves that could address over a thousand subnanoliter-volume chambers. This work is a cornerstone for microfluidic multiplexing, as it introduced both a simple valve that has since been ubiquitous in microfluidics, and a microfluidic multiplexor that allows a circuit to address a large number of lines and chambers from a small number of control lines. It is also the backbone of Fluidigm Inc., a major public microfluidic player, that commercializes different versions of integrated fluidic systems⁷. IFCs have since then been used for applications such as multiplexed PCR³⁰ and drug screening³¹.

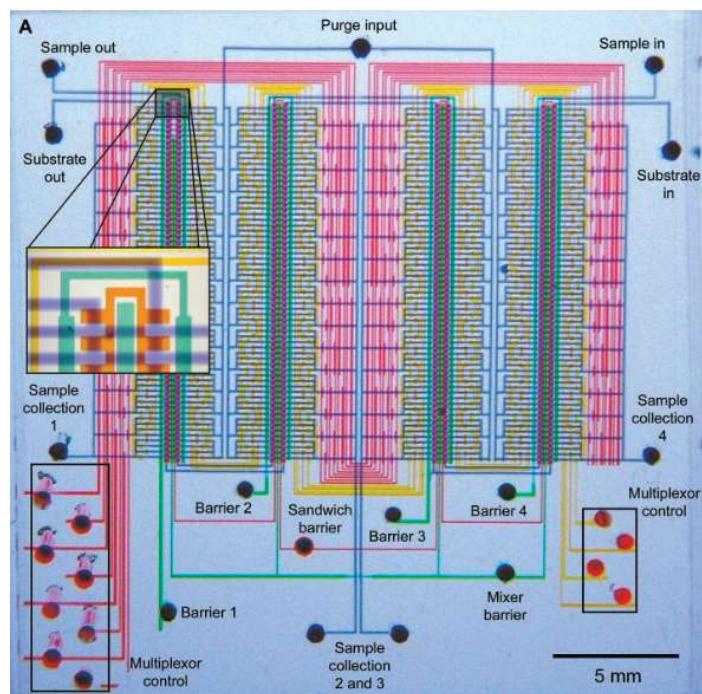


Figure 2.1 Micrograph of an integrated fluidic circuit (IFC) comprised of 256 individually addressable microchambers. This system can be operated using only 18 connections to the outside world. Reproduce with permission from Thorsen & al., Science (2002)¹⁰.

A different approach to high throughput microfluidic is the domain of droplet microfluidics⁹. In these types of devices, the samples, the reagents and the dyes are encapsulated in aqueous droplets that travel in a carrier oil fluid. These systems can operate at high throughput (droplets can be generated at up to 10kHz³²). Droplets can be merged to control chemical reaction. Using droplets minimizes the shear stress on the sample and insures mixing due to the internal advection. Droplet microfluidic systems are mainly known to be used for high-throughput PCR³³ and single cell screening³³.

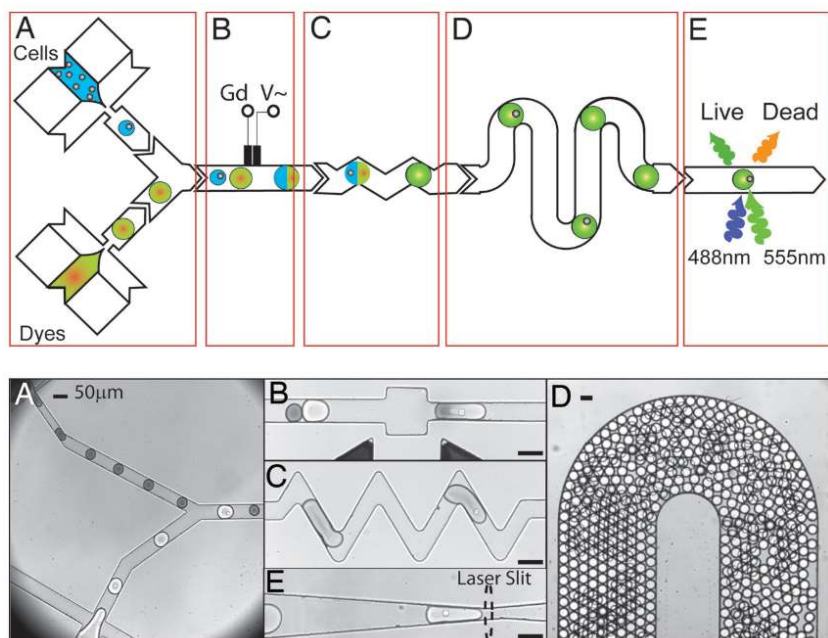


Figure 2.2 A droplet microfluidic on-chip viability assay. Schematic and micrograph of the system. A) Droplets with cells and dye are generated. B) Droplets are merged. C) The content of the droplets is mixed. D) Delay line. E) Signal measurement. Reproduce with permission from Brouzes & al. PNAS (2009)³³. Copyright 2009, National Academy of Sciences.

Most microfluidic systems, like those presented in this section, use channels and chambers to confine reagents and samples. They are not a viable solution to this project scope, which is to design a multiplexed system that can operate directly on surfaces. Channel-free and chamber-free systems that can operate on surfaces are the aim of a microfluidic subfield called open-space microfluidics, that will be thoroughly covered in the next section. It will be possible to see that for now, contrary to classic microfluidic systems, no high throughput open-space microfluidic solution exists.

2.2 Open-space microfluidics

Open-space microfluidics research comes from the desire to create devices that can interact, functionalize, pattern, or take measurements on immersed planar sample. Classical microfluidic systems are based on intricate circuits of chambers and channels, and generally require the sample to be inserted in the device. This comes with a variety of challenges, such as the limitation of the size of the sample and the presence of high shear stress that can damage some samples. Moreover,

these systems usually disrupt the standard protocol, which may be a hindrance to their use and adoption.

Open-space microfluidic systems are designed to work on surfaces. Rather than injecting the sample in the system, they interact with its surface. While various open-space system exists, they all forsake the use of channels and chambers. Their compatibility with open surface allows them to work with sample common in life sciences, such as cell cultures in Petri dishes, tissue slices, DNA microarrays and protein microarrays. Kaigala & al. give a good description of the perfect open-space system requirements³⁴;

- Non-invasive (preferably without contact).
- Work in immersed environment.
- Biocompatible (compatible with pH, temperature and shear stress used in biology).
- Flexible (work at various flow rate and surface dimension).
- Interactive (give feedback or allow live measurement).

While not all open-space microfluidic devices possess all these characteristics, they give a general idea of system specifications in this research field.

2.2.1 Chemistode

The chemistode is an open-space microfluidic device presented by Chen & al. in 2008. It aimed at creating the chemical equivalent of a microelectrode. The idea was to design a device that could chemically stimulate a sample, allow a small reaction time and analyze the molecular signal of the response³⁵ (Figure 2.3). The chemistode is a droplet microfluidic system comprised of a probe head with two integrated channels. One of them injects droplets of reagent that wet the surface and create a chemical stimulus. The other aperture aspirates the droplet. Reaspirated droplet can be mixed with fluorescent markers and analyzed. The chemistode allows the analysis of chemical pulses as short as 50 ms, and as a spatial resolution of 15 μm . However, both the surface of interest and the chemical signal of interest must be hydrophilic³⁶, which decrease the flexibility of this device.

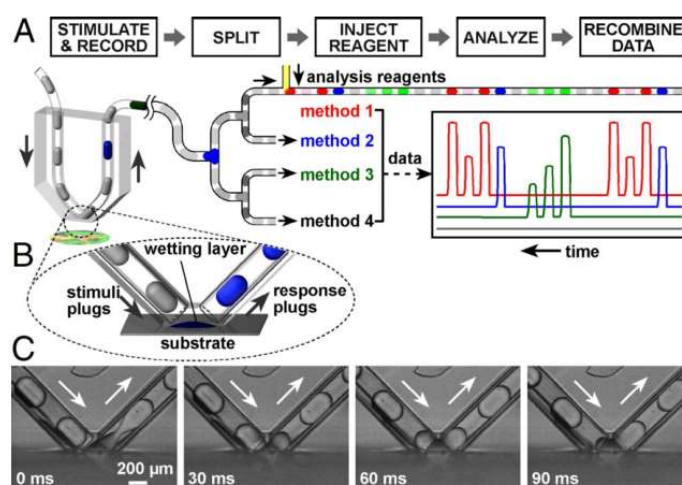


Figure 2.3. The Chemisthode. A) Schematic of the chemisthode operation. B) Close-up schematic of the tip of the chemisthode. C) Experimental bright-field micrograph of a stimulus droplet wetting a surface and being aspirated. Reproduced from Chen & al. PNAS, (2008)³⁵. Copyright 2008, National Academy of Sciences.

2.2.2 Atomic force microscopy-based methods

Atomic force microscopy (AFM) has been used for surface functionalization. One method, the dip pen lithography (DPN), consists in using the AFM tip as a nib to write on a surface^{37,38}. The resolution of such system is excellent (a few nanometers), however, it is incompatible with immersed surface. To circumvent this problem, Zambelli research group introduced the FluidFM in 2009. The FluidFM is a modified AFM tip with a microchannel integrated in its tip¹¹. This microchannel allows the FluidFM to work on immersed surface, and thus, with biological samples. Topographic data from the AFM allows a precise and delicate interaction with cells and tissues. FluidFM has been used to move single cells^{39,40}, and to perform intracellular and extracellular chemical reagent delivery^{11,41}. FluidFM is a promising open-space microfluidic system for single cell analysis. However, it is not useful for large surface processing, and it has low throughput.

2.2.3 Multiphase systems

The use of a multiphase system is a relatively simple method for the micropatterning of immersed surface presented by Taviana & al¹². The main idea is to immerse the surface to pattern in polyethylene glycol (PEG) and to inject a dextran mixed with the reagent of interest in the area

where patterning is required. Dextran and PEG are both biocompatible and immiscible. Dextran has a higher density, and always occupy the lower phase in contact with the sample (Figure 2.4). This method was successfully used to perform localized cell transfection¹².

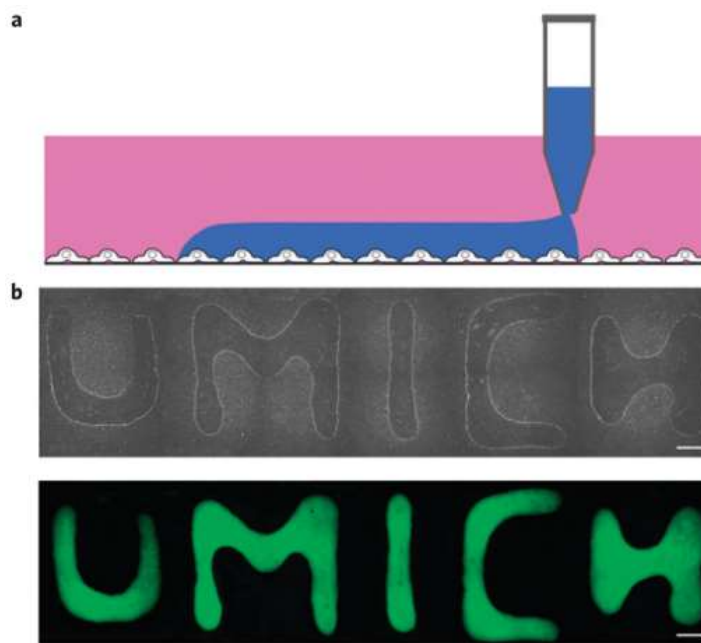


Figure 2.4: Aqueous two-phase system. A) Schematic of a two-phase system. B) Brightfield and fluorescent micrographs of a two-phase system used to write UMICH on a surface using FITC-labeled Dextran on a PEG immersed surface. Reprinted with permission from Tavana & al., Nature Materials, (2009)¹².

2.2.4 Micro and nanopipette

Multiple variants of micro and nanopipette have been presented in the last 20 years. Part of these research project concern pipettes in which the injection and the aspiration of reagent is controlled by an electrical potential. By changing the potential between an electrode positioned in the pipette and the fluid immersing the surface, fluid can be injected or aspirated (Figure 2.5)⁴². These systems can also be used to do scanning ion microscopy, which allows the measurement of surface topography. To do this, the voltage is held constant and the current between the electrode and the fluid is measured. Voltage triggered nanopipettes have been used for multiple applications, such as the deformation measurements of cardiac myocytes⁴², DNA and protein surface patterning^{42,43}, single molecule fluorescence tracking⁴⁴ and intracellular reagent injection⁴⁵.

Other research projects have focussed on pressure driven micropipette. They have mostly been used to sample intracellular content for mass spectrometry analysis⁴⁶⁻⁴⁸. Shiku & al. present a different approach with a dual channel micropipette⁴⁹. This pipette was used to perform the selective lysis of cells. One channel injected lysis buffer while the other aspirated the cell lysate.

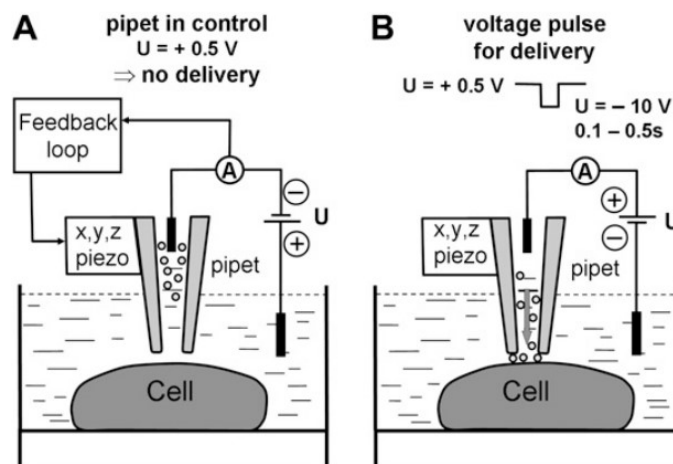


Figure 2.5. Voltage driven nanopipette for reagent delivery. Nanopipette operation for A) no delivery, B) reagent delivery. Reproduced with permission from Bruckbauer & al., *Biophysical Journal* (2007)⁴⁴.

2.2.5 Microfluidic patterning

A surface patterning method used by many research groups is microfluidic channel patterning. This method uses arrays of open microfluidic channels that are temporarily affixed on the surface to treat. The sample is used as a fourth wall to close the system. Reagents are then flowed in the channels to pattern the surface⁵⁰⁻⁵⁴. While microfluidic patterning is not per se an open-space microfluidic method, it achieves similar surface patterning, which explains why it is included here. Microfluidic channel patterning has mainly been used for surface functionalization with antibodies^{50,51}. It has also been used for immunohistochemical staining on histological slices⁵⁴, and in situ hybridisation⁵³. In 2014, a variant of this system was presented by Folch's lab. This system differs from previous by using a porous membrane to close the fourth wall of the system. In this configuration, the sample is positioned on the top of the porous membrane. It was successfully used for the parallel perfusion of tumor xenografts with dozens of chemotherapeutic drugs and cell viability markers¹³ (Figure 2.6). The parallel perfusion of tumor slices being one of the potential

applications for multiplexed open-space systems, a comparison between Folch lab system and an MFM could be interesting.

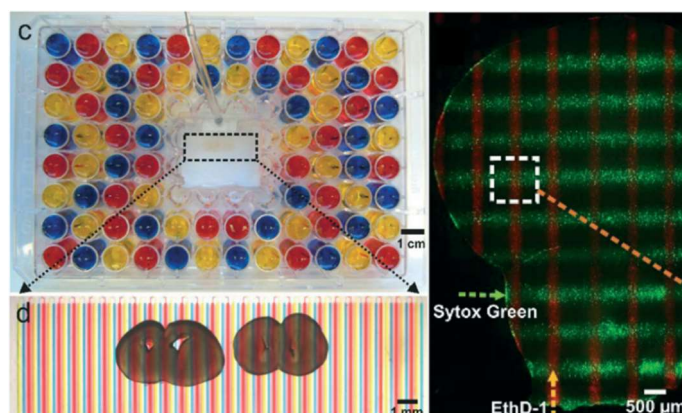


Figure 2.6 : Folch's research group parallel chemosensitivity assay chip. Reprinted with permission from Chang & al. *Lab Chip* (2014)⁵⁵.

2.2.6 Inkjet printer

Inkjet printers are generally not considered open-space microfluidic systems. However, they are one of the most prominently used devices for surface patterning which explains their inclusion to this literature review (the distinction with open-space microfluidics is that they are not compatible with immersed surface). Inkjet printers are systems that allow the precise deposition of droplets on surfaces. They can be operated in drop-on-demand or continuous mode. Inkjet with different actuation mechanisms exist, such as piezoelectric, thermal and electrostatic¹⁰. The compatibility of reagent varies greatly depending on the mechanism used by the inkjet. For example, thermal-based inkjets require thermally stable ink and can't be used to pattern proteins. Moreover, micro and nanodroplet deposited on surfaces are vulnerable to evaporation. Nonetheless, inkjets have been extensively used for various biopatterning applications, such as the fabrication of protein arrays and enzyme-based sensor⁴.

2.2.7 Microcontact printing

Microcontact printing is another method that is not being based on open-space microfluidics, but that allow similar precision surface patterning. While different variations of the method exist, the main idea is to use a molded polymeric bloc as a stamp to pattern a surface. In most common form,

a PDMS stamp is molded on a micromachined silicon wafer. The PDMS stamp is then covered with the patterning solution, either by pouring the solution on the stamp or by dipping the stamp in the solution. The stamp is then brought into contact with the surface to pattern, before being removed. Some iterations of microcontact printing were demonstrated to allow the deposition of sub-100 nm pattern¹¹. Microcontact printing has been extensively used with self-assembled monolayer. It was also used for protein patterning, cell patterning and DNA patterning¹².

2.2.8 Microfluidic probe & multipole

2.2.8.1 Microfluidic probe concept

Microfluidic probes (MFP) are considered as one of the most versatile open-space microfluidic system. They were first introduced in 2005 by Juncker & al¹³. Microfluidic probes, in their simplest form, are comprised of a flat surface and two apertures. The microfluidic probe is held in proximity with the immersed surface to pattern. The two injections are used to continuously inject and aspirate fluids. By maintaining an aspiration rate higher than the injection rate, the injected fluid is confined to a specific area on the surface, since all the flow lines are reaspirated (Figure 2.7). This effect is termed hydrodynamic flow confinement (HFC). Maintaining a small gap between the probe and the surface ensure that the flow is laminar viscous (Stoke flow). Microfluidic probes, being designed to operate in an immerse environment, are well adapted to life science experiments. They are a contactless technology, highly flexible in terms of size, flow rate, and compatibility with reagent, and they allow live measurement if operated over an inverted microscope.

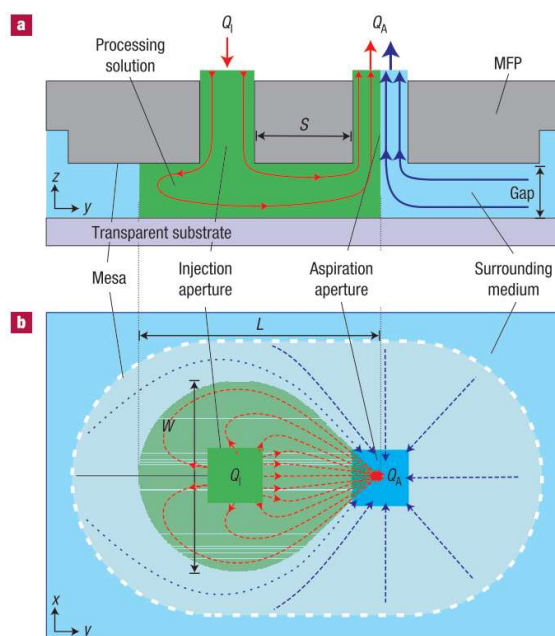


Figure 2.7 : Microfluidic probe working principle. The MFP is held over the surface to pattern. By having an injection flow rate lower than the aspiration flow rate, a confinement area is created. a) side view. b) bottom view. Reprinted with permission from Juncker & al. *Nature Materials*. (2005)¹³.

2.2.8.2 Microfluidic probe applications

The first article on MFP, published by IBM research, already presented multiple applications such as surface functionalization with proteins, cell staining and the selective detachment and collection of single cells¹³. Since then, over 60 papers were published on microfluidic probes, and proposed various other applications. The most recurrent application is cell and tissue staining, both on live⁵⁶ and fixed tissues⁵⁷. It was further used for immunohistochemical staining^{14,18}. The most promising work in this regard is the recent paper from Kashyap & al., that used MFP to perform quantitative micro-immunohistochemistry of patient-derived breast-cancer tissue. In this paper, they stained the tissues with the antibody for three biomarkers (PR, HER2, ER). Staining different areas of the tissue for different amounts of time allowed them to assess the binding dynamics and give a quantitative score for each biomarker. Another application related to immunohistochemical staining is the localized dewaxing of fixed tissues slides⁵⁸. It was used to perform localized staining of paraffin embedded tissues that are stored in a biobank, at a low cost and with little sample usage.

MFPs were also used for the selective lysis and sampling of live cells^{59,60}. Han's research group pushed the concept further in 2014 by using a microfluidic probe for the selective lysis and analysis of single cells, and integrating the reaction chamber for cell analysis directly in the microfluidic probe⁶⁰.

Microfluidic probes were shown to have potential for cellular microenvironment control. Microfluidic probes were used to perfused organotypic brain slices¹⁶, that are difficult to cultivate in classic microfluidic system due to their high sensitivity to shear stress. Other research groups used them to generate gradients and study cellular migration⁶¹. Recent work from Kaigala & al. showed that MFP could be used to create not only chemical confinement, but also thermal confinement⁶¹.

2.2.8.3 Microfluidic probe architecture

Several multiple architecture and geometry of MFPs have been presented since the first publication. One of them, the microfluidic quadrupole, allows the generation of precise and variable gradient⁶². One of the most used MFP architecture is the hierarchical probe. It is comprised of four apertures positioned on a line and allow to generate a dipole embedded in another dipole. This MFP can be used in two manners. The first mode, nested HFC, use the interior dipole to inject the fluid of interest, and the outermost dipole to shape the fluid of interest patterns. Using the appropriate parameters, the totality of the injected fluid can be reaspirated with low dilution, which allows the recirculation of the injected reagent (Figure 2.8b). In the second mode, pinched HFC, the outside dipole injects the reagent of interest, while the central dipole is used to pinch the fluid of interest on the sample (Figure 2.8c). The pinched HFC mode lowers the amount of wasted reagent by reducing the distance at which a molecule must diffuse to react with the sample.

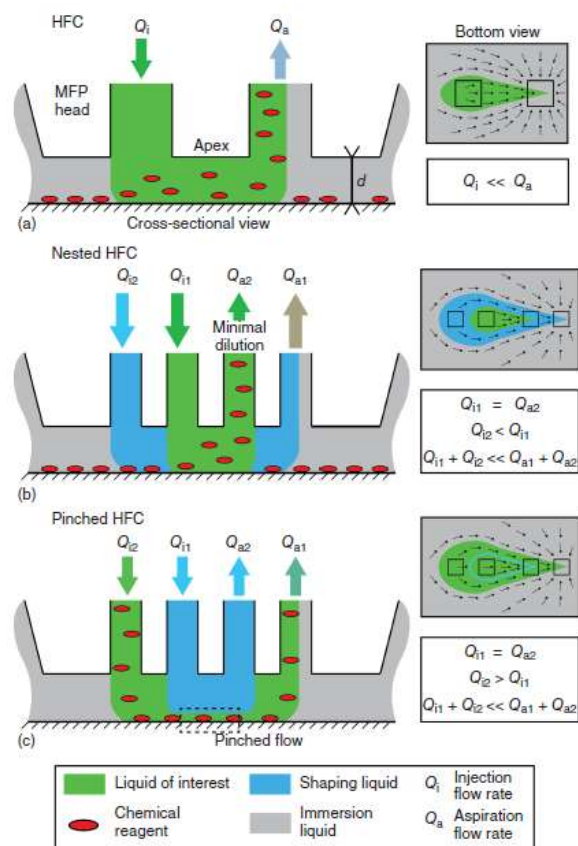


Figure 2.8 : The hierarchical MFP and its mode of operation. Grey represents immersion medium. Green and blue respectively represent the fluid of interest and a shaping fluid. A microfluidic dipole (a). A hierarchical MFP working in nested mode (b) and pinched mode (c). Reprinted with permission from Delamarche & al. *Open-Space Microfluidics: Concepts, Implementations, and Applications*, Chapter 2, Wiley VHC, (2018)⁶³.

The only MFP architecture allowing a somewhat level of multiplexing is a linear array probe¹⁸. Taylor & al. manage successfully achieved probe formed of 8 dipoles. It is important to note that dipole flow line affect each other (the dipoles collapse toward the center of the device). This effect was corrected by adding stabilization aperture to the design (Figure 2.9). While this correction is adequate for a relatively small multipole, this architecture would be unstable if massively scaled up.

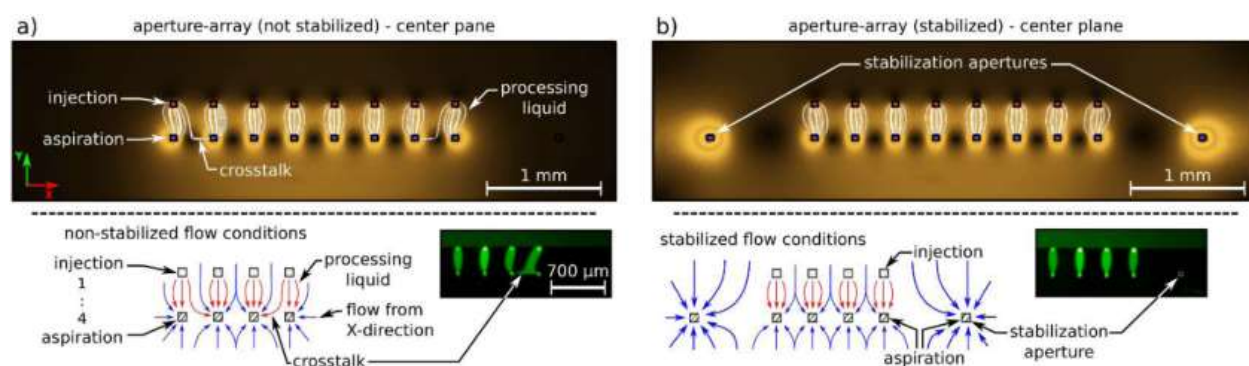


Figure 2.9 Flow lines and experimental micrograph of a dipole array, a) without stabilization apertures, b) with stabilization aperture. Reproduced with permission from Taylor & al. *Langmuir* (2016)¹⁸.

2.2.8.4 Microfluidic probe convection-diffusion model

The first convection model for the flow under an MFP was presented in 2011 for the microfluidic quadrupole⁶². Quasaimeh & al. propose that the flow under an MFP is a quasi-2D problem, and use Hele-Shaw flow approximation. They further show that the flow under an MFP can be analyzed as a potential flow problem. When using this model, the flow under an MFP become analog to a 2D electrostatic problem (Figure 2.10). Apertures can be seen as punctual charges, and the electric field lines correspond to the flow lines. This model is extremely accurate in predicting the flow line, fluid velocity, and the confinement area. However, the major shortcoming is that this model doesn't consider the diffusion in the flow, which is essential to modelize the full concentration profile under an MFP. In the same paper, Quasaimeh & al. also present a diffusion model, but it is valid only for the centerline of the MFP. After the quadrupolar MFP article, a second one presenting a similar model for the dipolar MFP was published⁶⁴.

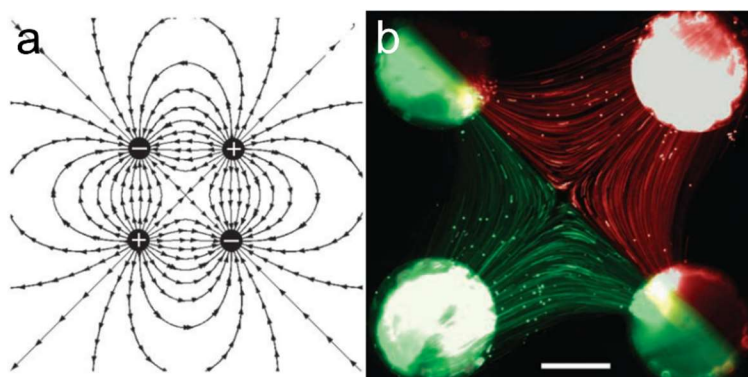


Figure 2.10 : A microfluidic quadrupole seen as a 2D electrostatic problem. A) Electrical field lines around four punctual charges positioned as a quadrupole. b) Fluorescent micrograph of fluorescent tracers under a microfluidic quadrupole showing the experimental flow lines. Modified and reproduced with permission from Quasimeh & al. *Nat. Commun.* (2011)⁶².

2.2.8.5 Microfluidic probe fabrication

The first MFPs were made from a silicon tip with DRIE etched microaperture¹³. This tip was plasma bonded to a PDMS block that served as a probe body and that allowed the interfacing between the micro-apertures and the capillaries. This method allowed the fabrication of MFP with apertures as small as 20 μm . However, the plasma bonding between the PDMS and the silicon tip make this type of probe fragile and prone to leaks. Other fabrication methods have been presented since then. One method consists in laminating pre-molded PDMS¹⁶. It is a simple method, but it yields deformable MFPs with an uneven tip. The most used method, and the standard method of IBM research group, is to DRIE etch channels in a silicon wafer and use anodic bonding to seal the MFP with a glass or silicon wafer⁵⁶. After the two wafers are bonded, the MFPs are cut and polished (Figure 2.11). This method yields precise, rigid, and robust MFP. Moreover, it is a batch process that can produce over 30 MFP on a 4-inch wafer. This method has the advantage that it could be used for the mass production of system. However, it requires access to a clean room and the equipment to perform DRIE etching, anodic bonding and precision silicon cutting. These processes also necessitate a certain level of optimization. The cost, equipment availability and time expenditure of this method can be a deterrent for university research groups, especially those focused in life sciences with little or no experience with clean room processes. Moreover, this method is limiting in terms of MFP geometries, as it can only be used to fabricate MFPs in which

all the apertures are positioned on one or two lines. In the framework of this research project, we aim at fabricating reliable MFM with a high number of apertures that can be positioned in any configuration. None of the previously presented methods fit the requirement of this project. The search for a cost-effective and user-friendly fabrication method adapted to academic research led us to direct 3D printing of microfluidic systems, which is the topic of the next section.

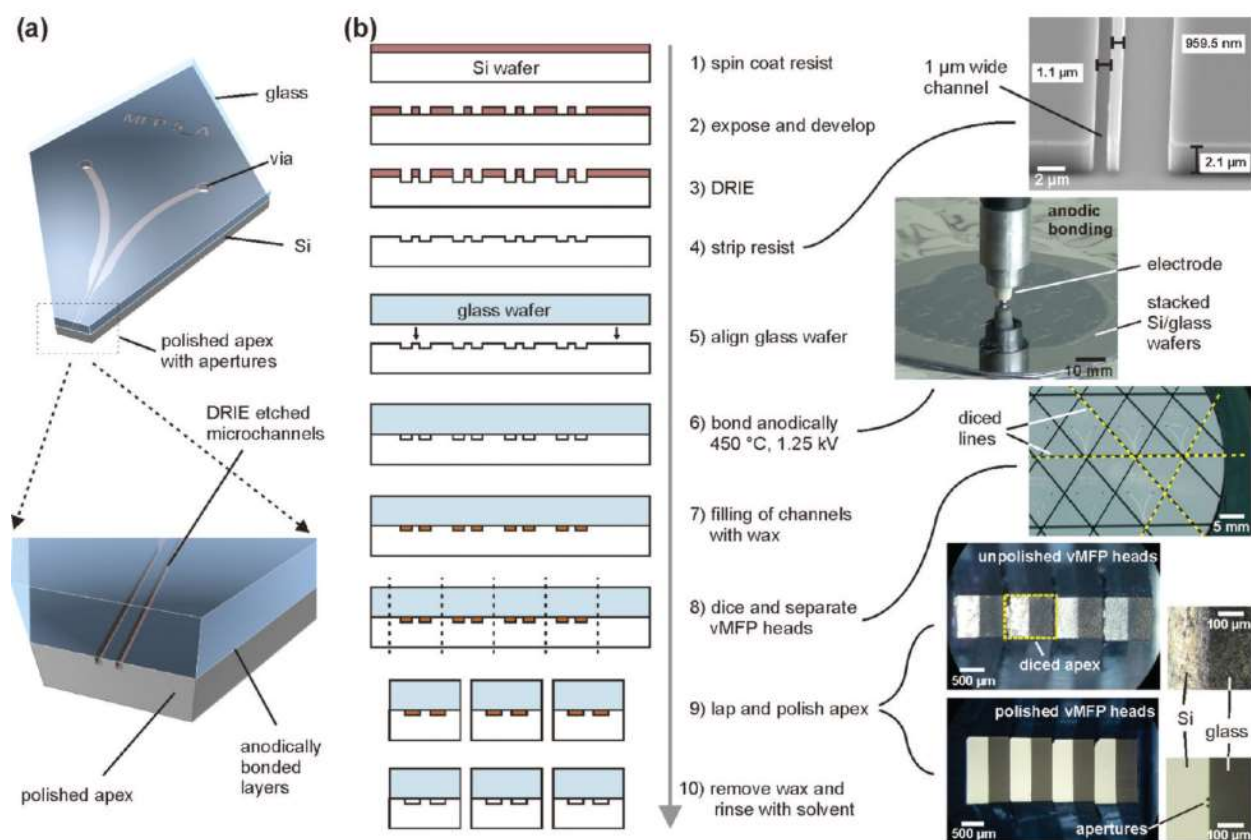


Figure 2.11 Multilayered MFP fabrication protocol used by IBM research group. (a) Schematic of a multilayered MFP head. (b) Illustration and schematic of the fabrication process. A DRIE etched silicon wafer is bonded to glass a wafer using anodic bonding. Reproduced with permission from Kaigala & al. *Langmuir* (2011)⁵⁶.

2.3 Direct 3D printing of microfluidic system

In the last decade, 3D printing and additive technologies have become mainstream. Costs have plummeted and the capabilities of those technologies have greatly increased. Many microfluidic research groups saw the opportunity and started to move away from traditional microfabrication

method and started using additive technologies⁶⁵. Some research groups are using 3D printing to fabricate soft lithography mold for PDMS⁶⁶⁻⁶⁸. The resolution of 3D printing is few orders of magnitude inferior to microfabrication. However, the complete fabrication cycle of a system (design, fabrication, test) is only a fraction of what it would be with microfabrication. The complete fabrication cycle can now be in the order of a day or two, where it would have been in weeks prior to the use of 3D printing.

Various research groups are suggesting that to use 3D printing at its full potential, microfluidic systems must be directly 3D printed⁶⁹⁻⁷¹. A major argument for that is that 3D printed systems are not limited to quasi-2D geometry like their molded counterparts. Moreover, 3D printed systems don't require molding and plasma bonding steps, which are the two time-consuming steps in a soft lithography process⁷². These steps are also difficult to scale up and can be a limitation to mass production. Direct 3D printed systems are generally monobloc, which makes them robust and not prone to leaks.

2.3.1 3D printing methods

Different 3D printing methods exist and have been used for microsystem printing. Fused filament deposition (FDM) works by melting and extruding a thermoplastic filament⁷³. While it is the most common 3D printing technology, it is generally considered that it doesn't offer the precision required for microsystem fabrication⁷⁴.

Polyjet (PJ), also named photopolymer inkjet printing is based on the jetting of droplets of UV sensitive resins that are subsequently photopolymerized⁷⁵. To print internal features, a sacrificial polymer must be printed and later dissolved. Dissolving this sacrificial layer can, however, be challenging for intricate channels arrays since this process is diffusion limited⁷³. That is why, while both stereolithography (SLA) and polyjet (PJ) have a similar resolution (~100 um), comparative studies point out that stereolithography is the most promising method for microfluidic systems⁷⁴.

Stereolithography (SLA) 3D printing is based on the polymerization of layers of resin in a bath. Early SLA system scanned a focalised laser to polymerise the resin. However, present SLA systems usually use UV led projected on a digital micromirror device (DMD) to control the polymerized patterns. These systems are termed digital light processing SLA (DLP-SLA). Other than their

significantly lower cost, DLP-SLA systems have two main advantages over their laser scanning predecessor predecessors. The array of micromirror allows the polymerisation of the whole layer concurrently, which increase the printing speed. Moreover, the printing resolution is determined by the micromirror size and the optical magnification of the lens systems, and result in a better resolution than laser focalised systems⁷³.

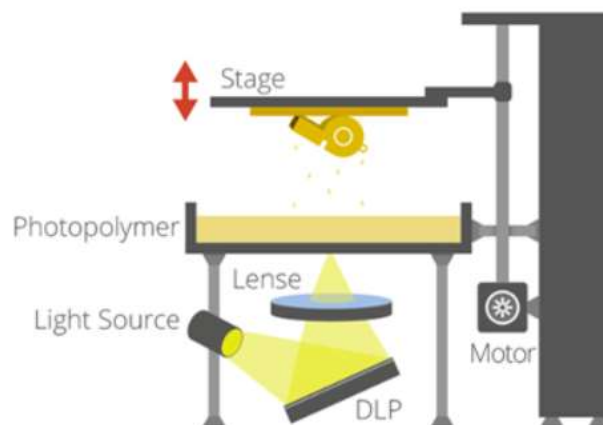


Figure 2.12 A DLP-SLA 3D printer. The image is formed by reflecting the UV light from a light source (generally UV led) on a digital micromirror device (DMD). The image is then magnified by a lens. For each layer, the image is projected, then the stage is moved up by the layer thickness before the subsequent layer is projected. Reproduced from 3D printing industry [<https://3dprintingindustry.com/>].

An alternative method that could have been used in this research project is a two-photon polymerisation system (2PP) such as the nanoscribe⁷⁶. 2PP systems operate in a similar fashion than the laser scanning SLA systems. However, they use two-photon absorption to polymerise the resin. Two-photon absorption is a non-linear effect that happens only close to the focal point of the laser. 2PP systems offer incomparable performance with a submicron resolution⁷⁶. However, both the cost (>250k USD), and the lengthy fabrication for large chip are prohibitive⁷⁷.

2.3.2 Direct printing using SLA

The direct 3D printing of microfluidic system is still limited. Commercial SLA 3D printers and resins are not adapted to microfluidic design. Current stereolithography printers are mainly aimed

at audiology, denturology and jewelry, where most feature are external details rather than voids in blocks like required by microfluidics. Nordin research group published multiple articles on the fabrication of stereolithography 3D printers⁴ and UV sensitive resins^{69,78} adapted to microfluidic requirements. This allows them to fabricate systems with microchannels with a diameter of 20 μm in a biocompatible resin⁶⁹. It is around a tenfold smaller than what is currently possible to print using a commercial printer⁷⁴.

Other research groups are working on the printing of more traditionally used material such as Glass⁷⁹ and PDMS⁷⁷, which should improve both the chemical compatibility and the optical properties of printed systems. Using both custom and commercial printer, different research laboratories have worked on a large range of SLA 3D printed devices and components, such as gradient generators⁸⁰, valves, pumps^{74,81,82}, high density interconnections⁸³ and culture chamber⁸⁴.

2.4 Microfluidic multiplexor

Microfluidic multiplexors are an essential component to achieve a large-scale multiplexable lab on a chip. They serve the purpose of selectively addressing one of many channels while keeping a low number of control lines. In a system, they can be used to fill fluid lines selectively and sequentially (select one of many output), or inversely, to select one reagent to inject from many (select one of many inputs). By using multiplexor on the input and the output, different reagents can be injected into different lines.

The first microfluidic multiplexor was presented by Quake's research group. It was based on a binary architecture (like electronic multiplexor), and allowed the control of $2^{N/2}$ fluid lines from N pneumatic lines¹⁰. They later presented modification to this design to diminish the dead volume in the multiplexor, thus diminishing the contamination⁸⁵. Hua & al. later presented a combinatorial multiplexor that allows the control of $N!/((N/2)!)^2$ fluid lines from N pressure lines⁸⁶. This multiplexor is more efficient than the binary multiplexor from Quake research group. For example, for 12 control line, this multiplexor can control 924 fluid lines, compared to the 64 that could be controlled from the binary multiplexor.

Another method to improve multiplexor efficiency is to use pressure valves with multiple pressure level thresholds⁸⁷. Lee & al. demonstrated that, using valves with three pressure levels, it was

possible to control four fluid lines with only two control lines. However, these control lines would require pressure line with variable pressure control, which adds a lot of complexity.

Microfluidic multiplexors have also been used to control pneumatic circuit rather than fluid lines. One main advantage of pneumatic circuit is that they allow the fabrication of latching valves (these valves use the air compressibility and thus can't be used in fluidic circuits). Grover & al. used a multiplexor to address pneumatic latching valves. They could sequentially change the state of 16 latching valves using 5 control lines⁸⁸. To further increase the control of the system while limiting the number of control lines, Rhee & al. further used pneumatic circuit with multiplexor and latching valves to create pneumatic logic circuits. They used those logic gates to control multiplexor of a microfluidic circuit⁸⁹. Controlling microfluidic circuit using integrated pneumatic logic circuit is an interesting avenue for highly multiplexable system, but this technology is still far from being mature.

CHAPTER 3 PROJECT OVERVIEW

This chapter gives a brief project overview of this research project. It first covers the principles behind the microfluidic multipoles, presents the different type of multipoles and explain how they are linked to this research project. This chapter ends with a short section on MFM convection-diffusion models.

3.1 The microfluidic multipole

3.1.1 The microfluidic probe vs. the microfluidic multipole

The main goal of this project is to take the principle behind the microfluidic probe and use it to create multiplex open-space devices. The original microfluidic probe was comprised of two apertures and made to be operated as a scanning device. In this thesis work, we hypothesize that any number of apertures could be put at the tip to create intricate fluid patterns. As our system became more complex and made to be operated without scanning, it became evident that the term microfluidic probe did not describe our work properly. Therefore, we defined the microfluidic multipole (MFM) as an open-space system comprised of any number of apertures that uses hydrodynamic flow confinement to create fluid patterns on surfaces. MFMs include microfluidic probe, but also all the systems presented in this work, such as the pixelated chemical display that allows the creation of fluids pattern made of hundreds of independent fluid confinement areas. The name multipole was chosen because there is a strong mathematical analogy between electrostatic and magnetostatic multipole field line patterns and those of streaming patterns under arrays of apertures in a Hele-Shaw cell, as we will see at the end of this section. Under this new framework, the microfluidic probe as described early on represents the dipole subclass of microfluidic multipoles.

3.1.2 Microfluidic multipole basis

MFMs are formed of a body with a flat tip on which apertures are positioned (Figure 3.1). To operate, MFM must be held in close contact with the surface, which creates a small gap that acts as a Hele-Shaw cell⁹⁰. This small gap confines the fluid and ensure the flow is laminar and viscous.

It is important that the MFM tip is parallel to the surface because a misalignment would create variation in the hydraulic resistivity and deform the fluid patterns.

Apertures are injecting and aspirating fluid continuously. Stationary flow patterns can be generated on the surface when the net flow rate is negative due to hydrodynamic flow confinement. Since a net aspiration is present, the sample surface must be immersed in a fluid (although a method to get around this constraint is discussed in Chapter 6). Apertures are linked to pumps through tubes that are connected to the sides of the MFMs (Figure 3.1b).

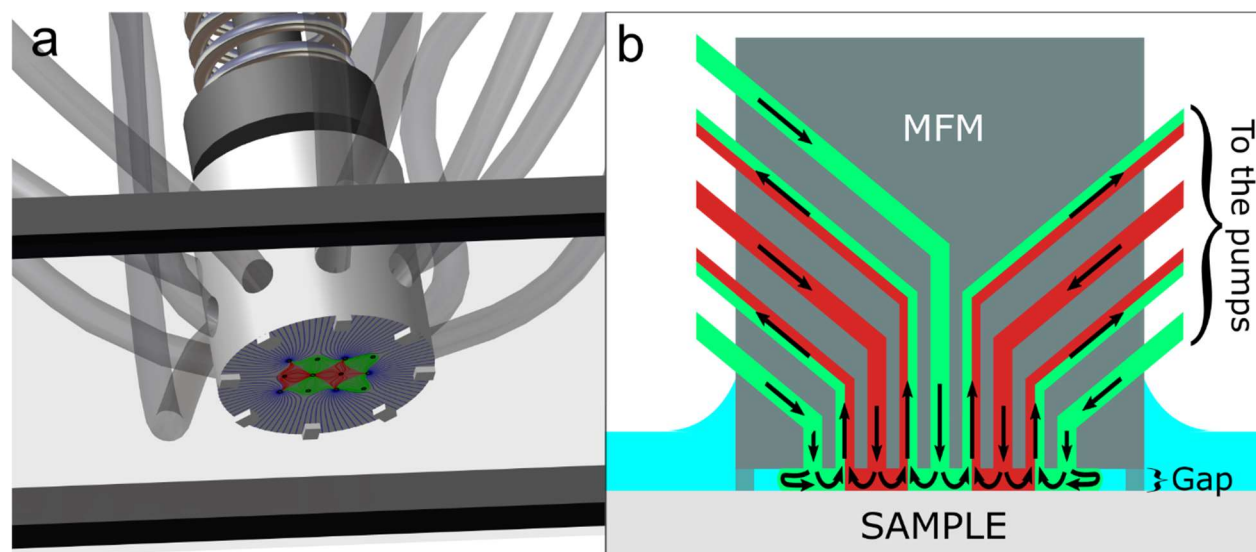


Figure 3.1 MFM Schematic. A) A 3D schematic of a MFM held over a surface. B) Side cut of an MFM. Aspirations and injections are streaming continuously, which result on stationary patterns on the surface.

3.1.3 MFM in this thesis

During my research project, multiple concepts and designs were tested. They can be separated in two main groups. The first one is the small reconfigurable MFM group. They are comprised of a small number of apertures (<12), and every aperture is connected to a single pump (Figure 3.2a-c). These systems can be reconfigured rapidly by turning on and off each pump. While these small MFMs cannot compete with the multiplexing of later systems, they offer an unmatched reconfigurability dynamic. Due to their simplicity, a lot of variants of small MFMs could be tested, which turned out extremely useful in the exploratory phase of my project. A cornerstone of my

work with small MFMs is the first demonstration a long-term and multistep assay using an open-space microfluidics. It was done by automating an immunofluorescent assay on a protein chip. These systems will be discussed in chapter 4.

The second group are the pixelated chemical displays (PCDs). These systems are based on large array of apertures (Figure 3.2d-f). A distinction with small MFMs is that the apertures are connected to the pumps through systems of manifolds. Moreover, PCDs are reconfigured by changing the fluid injected in fluid lines using a system of valves. A second major distinction is that PCDs use a scalable architecture and can theoretically be scaled to control fluid in any number of independent confinement areas. These systems also have the particularity that they can be used on a dry as well as an immersed surface. Chapter 6 and 7 will cover those systems.

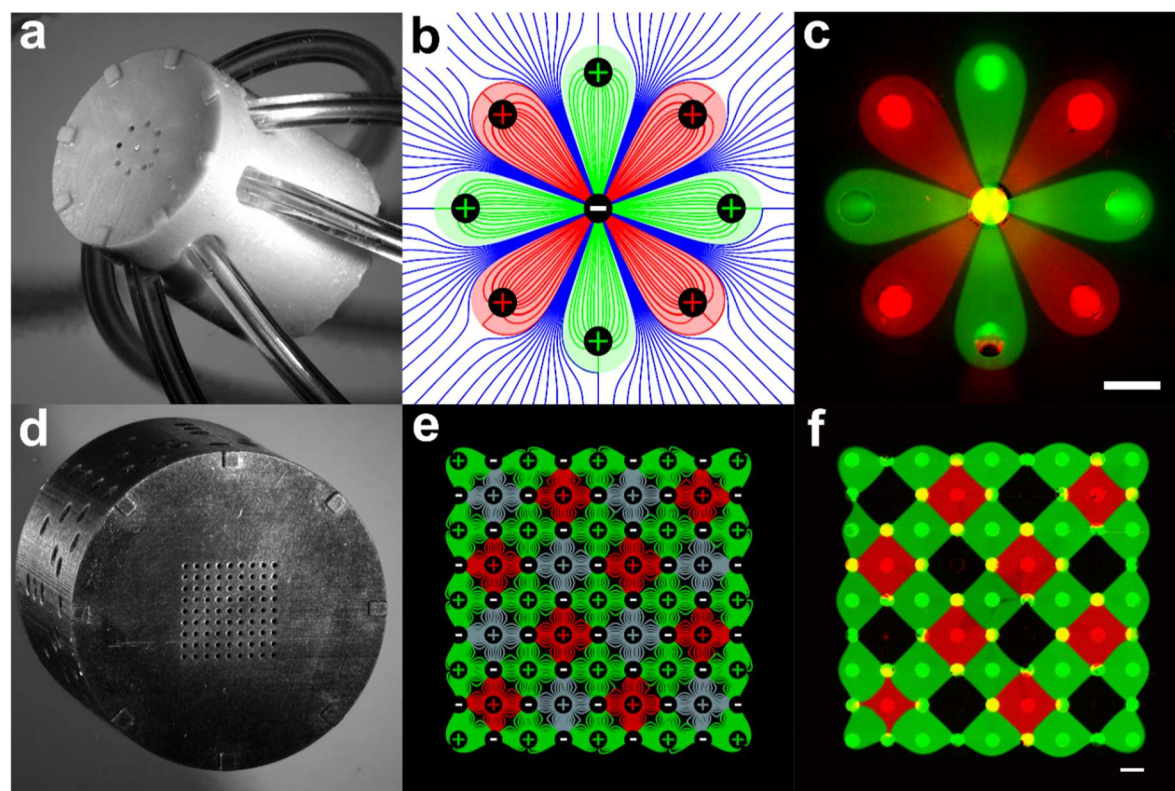


Figure 3.2 Small reconfigurable MFM and PCD. The top row is a axisymmetric MFM and the bottom row is a square-pixel PCD. a), d) Micrograph of the system. b), e) Theoretical flow lines. c), f) Fluorescent micrograph of the surface patterning. Scale bars represent 500 μm .

Both types of system and the manifold required in this project were designed and fabricated using script-assisted CAD and stereolithography 3D printing. This fabrication method was chosen in part because of the multiple geometry of systems that had to be fabricated. Stereolithography is versatile and the process as the advantage of being mostly geometry independent. The fabrication process I developed is the workhorse of this thesis and will be discussed in chapter 4. However, before diving in the heart of the project, I will address MFM flow theory.

3.2 Multipolar microfluidic theory

3.2.1 Potential flows

MFM's form a Hele-Shaw cell⁹⁰, where the fluids are confined in between the sample and the tip of the system. That results in transport theory problems for MFM being quasi-2D. Flow under MFM tip can be seen as 2D potential flow⁶² (hence the name microfluidic multipole and multipolar microfluidics). Potential flow describes the flow velocity field as a gradient of a velocity potential. Flow lines and fluid velocity can thus be calculated by solving Laplace's equation rather than the much more complicated Navier-Stokes's equation⁹¹. Potential flow fails to satisfy the no-slip condition at lateral walls, but since there are no walls in MFM, it is well suited.

MFM complex velocity potential (Φ) can be expressed as a sum of each aperture velocity potential⁹².

$$\Phi = \sum_i q_i \log(z - z_i) \quad (1)$$

Where q_i is the flow rate of the apertures and z_i the complex position of the apertures. By differentiating the complex velocity potential Φ , the velocity field \bar{u} can be found.

$$\bar{u} = \frac{d\Phi}{dz} = u_x(x, y) - iu_y(x, y) \quad (2)$$

Thus, velocity field can also be found as the superposition of the velocity field of each aperture.

$$u_x = \sum_i q \frac{(x - x_i)}{(x - x_i)^2 + (y - y_i)^2} \quad (3)$$

$$u_y = \sum_i q \frac{(y - y_i)}{(x - x_i)^2 + (y - y_i)^2} \quad (4)$$

The velocity field superposition was used throughout my project to predict MFM flow patterns, as presented in Figure 3.3. A simple Matlab code was made to generate the streamline and velocity field of MFMs from a list of aperture position and flow rate.

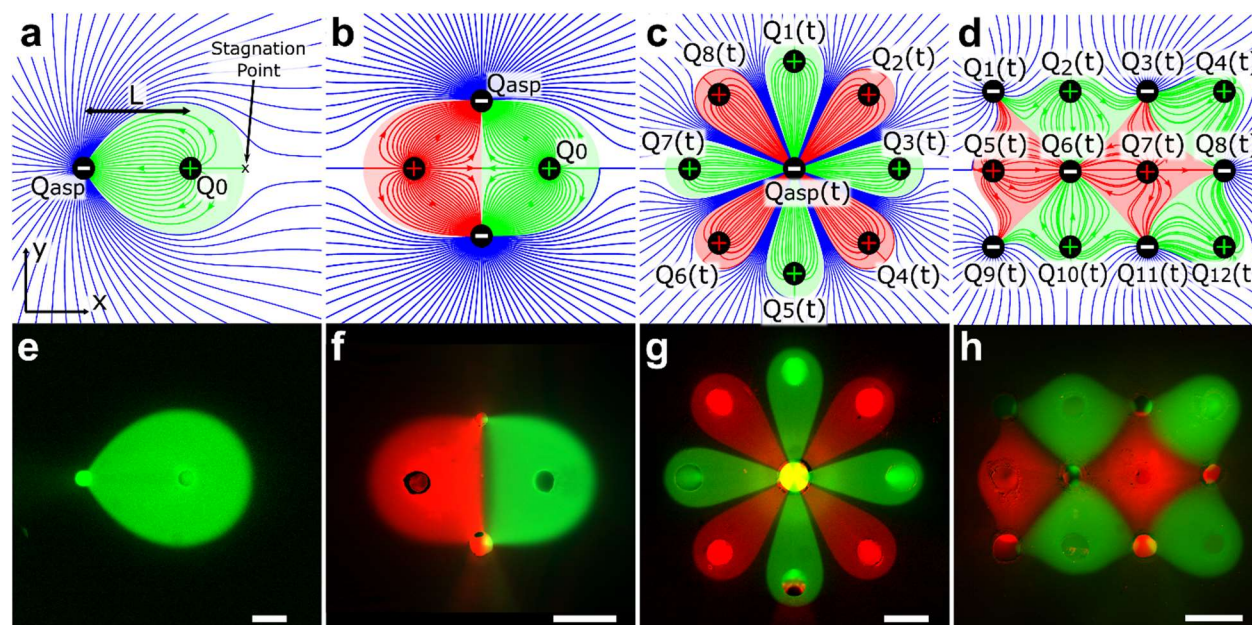


Figure 3.3 MFM streamline. (a-d) Example of MFM streamline generated using the superposition of the velocity field from every aperture. (e-h) Comparison with fluorescent micrographs. (a,e) Dipole. (b,f) Quadrupole. (c,g) Rotationally symmetric MFM. (d,h) 12-aperture MFM. Figure from Goyette & al. *Nat. Commun.* (2019)⁹². License CC BY 4.0 <http://creativecommons.org/licenses/by/4.0/>.

It is not a coincidence that previous equation and figure greatly resemble 2D electrostatic problems. There is a strong parallel between potential flow and electrostatic⁶². They are both potential problems with the same solutions. The electric potential field from punctual sources is an analog to the velocity potential from a MFM aperture. The electric field lines are the equivalent to the fluid streamlines. The flow lines under a microfluidic dipole are the same as the electrical field line from an electrostatic dipole. This analogy is helpful in predicting flow lines of MFMs when an electrostatic equivalent is already known.

Potential flows are an easy way to predict convection under an MFM. However, this model fails to predict diffusion under an MFM. This model can be used to determine the confinement area, pattern

shape and flow velocity, but give no information on gradient length at pattern limits. To get a concentration map for a MFM, a convection-diffusion model is required.

3.2.2 Convection-diffusion and conformal mapping

The analytical model presented in the next few paragraphs was developed by my colleague Étienne Boulais, and was published in an article we co-wrote⁹² and further described in a second article⁹³. While this model is not essential to understand most of my work, our projects are closely linked (my experiments on MFMs were used to validate his model, but it was later used to generate new MFM designs and predict convection diffusion in them). This section is intended to be a brief overview of the model without a strong mathematical formalism.

From the potential flow, we know that a MFM with a negative net flow rate has a steady state with steady confinement pattern. Transport in a MFM can be described by the convection-diffusion equation:

$$\nabla^2 c - Pe(\bar{u} \cdot \nabla c) = 0 \quad (5)$$

Where Pe is the Péclet number equal to $Pe = Q_0/2\pi GD$, G is the gap (distance between the multipole and the surface), D is the diffusion constant of the analyte, Q_0 is the injection flow rate and c is the concentration. The term $(\bar{u} \cdot \nabla c)$ is intractable even for simple MFMs. A work around this problem is to use conformal invariance property of the convection-diffusion equation in 2D potential flows. By transforming the concentration map of a problem with a known solution into the geometry that interests us, we can obtain the solution to our problem. Multiple conformal transformation can then be applied subsequently to determine concentration for increasingly complicated MFMs.

The first step is to determine concentration the simplest MFM, the dipole. Let's consider a simple microfluidic dipole with an injection at origin, an aspiration located a $z = -1$ and an aspiration to injection ratio equal to α . This ratio α is strictly superior to 0 for MFMs, since an injection rate higher than the aspiration rate would result in an unconfined MFM where the injected reagent leak toward infinity. The convection-diffusion problem for this dipole can be transformed to a streamline problem using the transform

$$\Phi(z) = \log(z) - \alpha \log(z + 1). \quad (6)$$

Which is the complex velocity potential of such dipole as presented in the last section. When applying this transformation, the problem becomes analog to flow in a channel in which flows of concentrations $c=1$ and $c=0$ are separated by a no flux boundary positioned at the origin (Figure 3.4a). Past a certain distance (which is related to the position of the stagnation point in the dipole) the no flux boundary is removed, and the fluids mix. This semi-infinite obstacle problem has been previously studied and has a known solution⁹⁴

$$c(\Phi) = \frac{1}{2} \left(1 \pm \operatorname{erf} \left(\operatorname{Im} \sqrt{Pe(\Phi - \Phi_{stag})} \right) \right), \quad (7)$$

Where erf is the error function. Φ_s is the image of the stagnation point and can be calculated by evaluating $\Phi(z)$ for z_{stag} equal to the stagnation point of the dipole. The stagnation point is a point where flow rate equals 0. For the dipole in our problem, it was previously demonstrated that z_{stag} is⁹⁵

$$z_{stag} = \frac{1}{\alpha-1}. \quad (8)$$

Thus, the concentration profile for a microfluidic dipole (Figure 3.4b) is

$$c(z) = \frac{1}{2} \left(1 \pm \operatorname{erf} \left(\operatorname{Im} \sqrt{Pe(\log(z) - \alpha \log(z+1) - \Phi_{stag})} \right) \right). \quad (9)$$

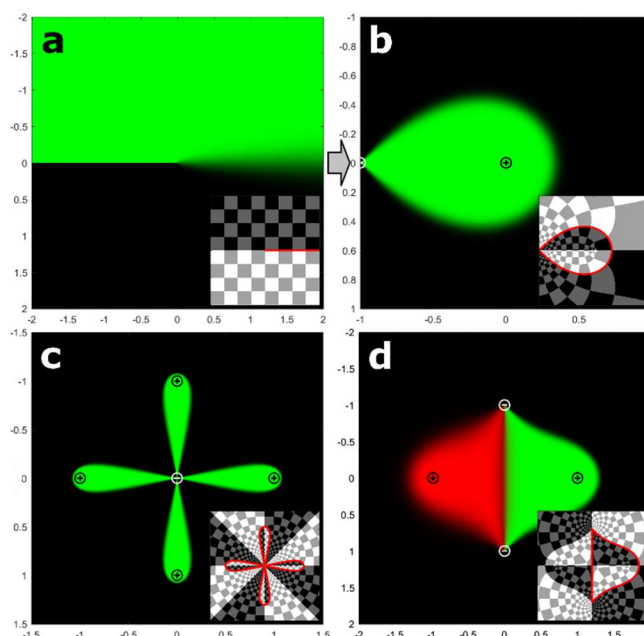


Figure 3.4 Concentration profile from the theoretical convection-diffusion model. Concentration profile for a) a semi-infinite obstacle, b) a microfluidic dipole, c) a 4 petal rotationally symmetric MFM, d) a microfluidic quadrupole. Figure modified from Goyette & al. Nat. Commun. (2019)⁹². License CC BY 4.0 <http://creativecommons.org/licenses/by/4.0/>.

The interesting part for this thesis is not how to obtain the concentration profile for the dipole, but what we can do with it. In the same manner that the semi-infinite obstacle can be transformed into the dipole, the dipole concentration map can be transformed into more complicated MFMs. Some examples are the $\omega = z^{1/n}$ transformations that generate rotational symmetries and that can be used to generate “flower” (Figure 3.4c) or polygonal MFMs that are used later in this thesis. Another transform is the $\omega = (2z + 1)^{1/2}$, which transform the dipole into a quadrupolar probe (Figure 3.4d). Table 3-1 presents a short list of conformal mapping that can be applied to the dipole solution. The results of those mapping are presented in Figure 3.5. An exhaustive list is available in Appendix A.

Note here that some details and subtleties were left out for the sake of simplicity. I would recommend to readers interested in more details to read Étienne Boulais’s detailed article⁹³.

Table 3-1: Example of conformal transformation that can be applied to the microfluidic dipole solution.

Straight Flow	$\omega = \log(z) - \alpha \log(z + 1)$
Microfluidic Quadrupole	$\omega = (2z + 1)^{1/2}$
Flower Multipole	$\omega = (z + 1)^{1/n}$
Polygonal Multipole	$\omega = z^{1/n}$
Impinging Flows	$\omega = 1/z - 1$

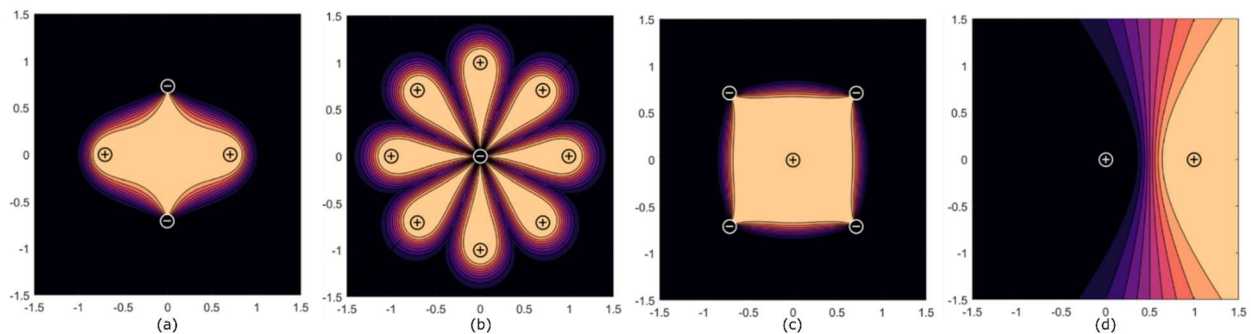


Figure 3.5 Solution of the conformal transformations from table 3-1 applied to a dipole. Concentration mapping for (a) the quadrupole transformation, (b) the flower multipole transformation, (c) the polygonal multipole transformation, (d) the impinging flows transformation. Modified and reproduced with permission from Boulais & al. *Physics of Fluids* (2020)⁹³.

CHAPTER 4 MICROFLUIDIC MULTIPOLES AND PIXELATED CHEMICAL DISPLAY FABRICATION

Objective #1: Develop a robust and versatile method to fabricate microfluidic multipoles.

This chapter covers the CAD design and the fabrication method used for the fabrication of microfluidic multipole and pixelated chemical displays. The method presented here has been used throughout my PhD, for the fabrication of simple MFMs as well as intricate design with hundreds of channels. The article “3D Printed Microfluidic Probes” from Brimmo, Goyette & al. (on which I am co-first author) would be a good introduction to this chapter. However, this chapter provides a more in-depth and up-to-date picture of the method used.

4.1 CAD design

Before any fabrication takes place, the systems must be modeled in a CAD software. This step is usually overlooked as it seems relatively simple. While it is true for basic systems, a thought about the best modelling method to use for complex systems comprised of hundreds of features is essential.

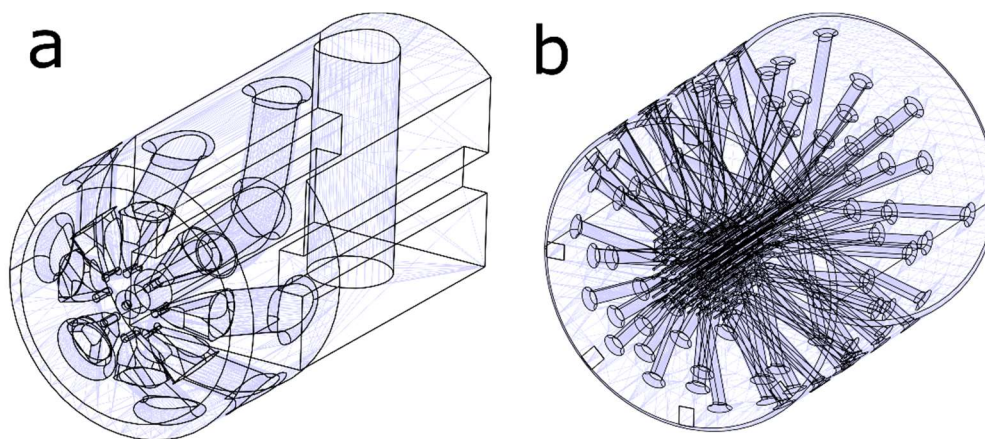


Figure 4.1 Differences in CAD complexity. a) User designed 9-aperture “Flower” microfluidic multipole. b) Script assisted model of an 81-aperture PCD.

Microfluidic multipoles with fewer than 25 channels have all been directly designed in Catia v5. However, when the project shifted toward pixelated chemical displays (PCD), systems changed from having a dozen apertures to up to three hundred. The designing time climbed from around a half-day to a few days. Moreover, modification to designs became complicated. To work around those problems, I decided to use script-assisted CAD with a library of components. The main idea was to create a library of simple features such as apertures, channels and body with different sizes. A script was then used to position, orient, and link these features together. Systems based on regular arrays of apertures (such as PCD) allowed for a relatively simple script.

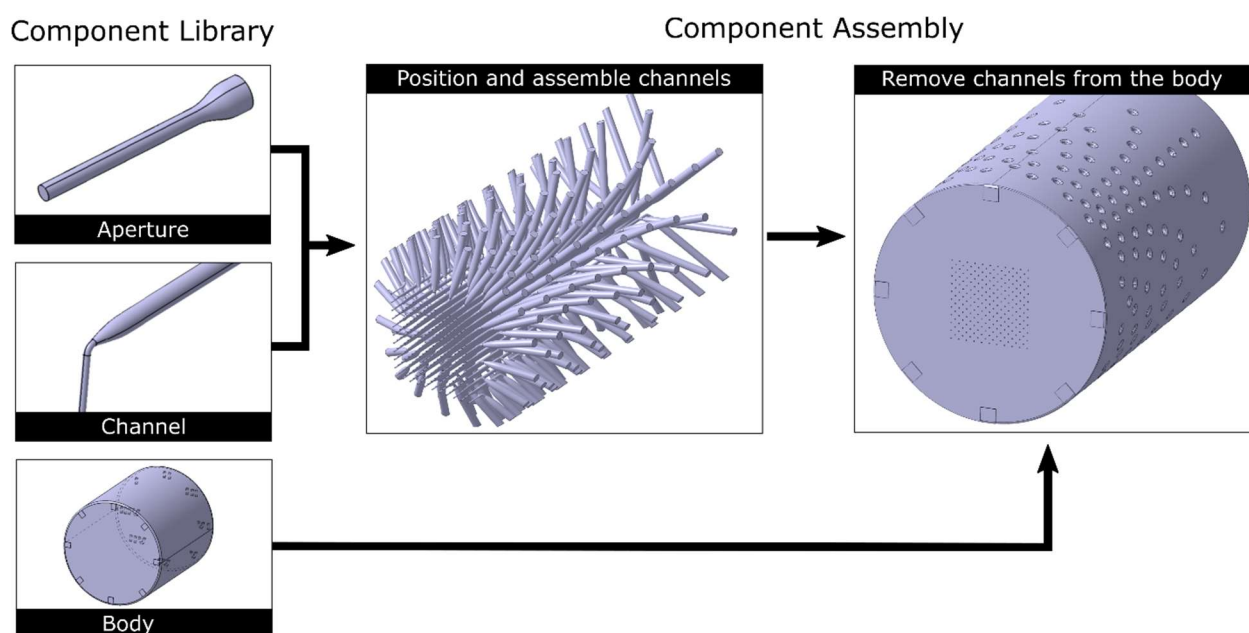


Figure 4.2 Script-assisted CAD design visual protocol.

Systems architecture was designed to allow an easy programming, and to maximize the distance between the channels. Maximizing distance between channels allows for more robust systems and a higher yield. The best solution found was to radially orient every channel. Moreover, channels were organized in different levels, the outmost aperture being the first level, the second outmost apertures being the second level, etc. For each level, the connection to tubes was positioned at a different height on the PCD side. While it was easy to program, it also allowed for an easy connection of the tubes since the architecture was well organized and standardized between systems.

While script assisted CAD is more complicated than direct design and took a significant time investment to learn, once the library and scripts were written, it allowed the design of extremely complex design (like a 313-aperture PCD) in less than a half-day. Such design would have been virtually impossible to directly design by hand. It also allows non-experts to do modifications (like change channels size or the number of apertures) on an existent PCD design.

Catia v5 scripts are limited and far from user-friendly. An alternative was to use a software dedicated to script CAD, such as OpenSCAD. I tested this option for my collaboration with Greg Nordin lab in BYU (the collaboration didn't go through as expected due to the COVID-19 pandemic). In this software, every component must be scripted. While it is time consuming, model with repetition of features can easily be made, as demonstrated in Figure 4.3 (manifolds are repeated and used at different scale). Moreover, it allows the design to be made on a grid corresponding to the 3D printer pixels, which becomes important for high-precision 3D printing⁶⁹. Figure 4.3 presents a PCD designed in OpenSCAD and that Nordin's lab printed.

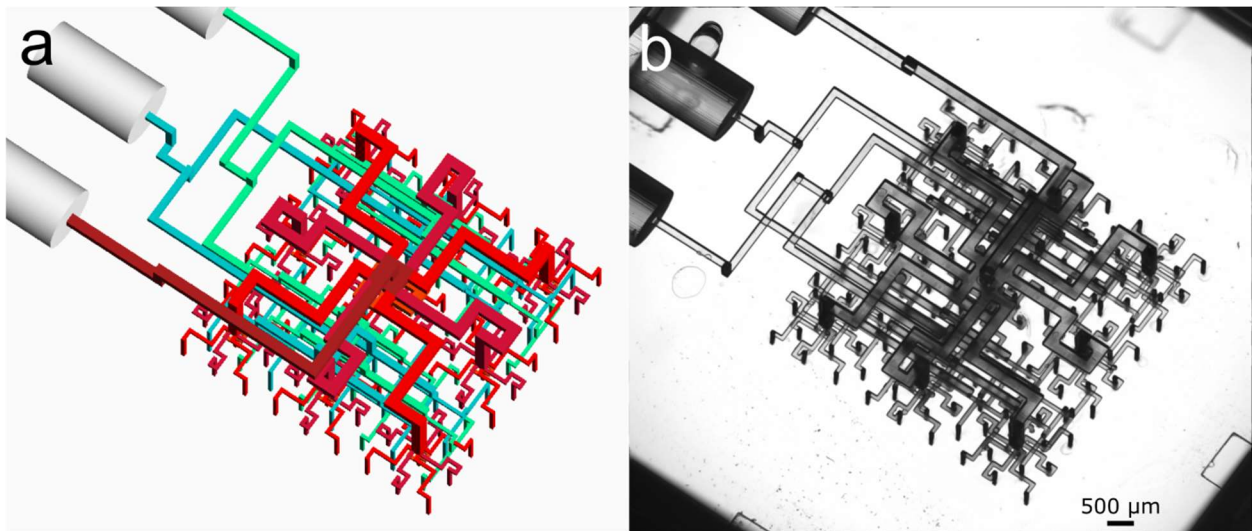


Figure 4.3 a) Model of a PCD with integrated manifold made with OpenSCAD, a script-only CAD software. Notice that the 9:1 manifold (in red) are repeated and used at two different scale. b) The PCD design from a) 3D printed by Nordin's group in BYU.

4.2 3D printing and post-processing

Before the start of this project, one major barrier to the use microfluidic probe and multipole was the fabrication method. The first MFPs used a micromachined silicon head bonded with a PDMS chip-to-world interface^{13,62}. IBM research group later standardized their MFP fabrication method. They abandoned the fragile PDMS-silicon bonding to use a two-layer architecture. A layer of glass and a DRIE etched layer of silicon are anodically bonded⁵⁶. This method yields reliable probes, however, it requires access and the appropriate training in a clean room facility. It might be a challenge for researcher from life-science oriented research groups. Other fabrication methods were presented^{16,96}, but they all required similar clean room facility processes. The first objective of this project was to find a cheap and accessible alternative to fabricate reliable and robust microfluidic multipole. I opted for the growing field of 3D printed microfluidic systems⁹⁷.

MFMs were 3D printed using digital light processing stereolithography (DPL-SLA). Since one objective of the project being to develop an accessible method to build microfluidic multipole, we used commercially available printer and resins. The Asiga Pico 2 HD was used. This printer has a wavelength of 385 nm, a resolution of 27 μm and a build size of 52 x 29 mm. Early in the project, different resins were used. However, the best results were yielded using Pro3dure GR-1 black with layer thickness of 50 μm . This resin is opaque, which is essential for good quality live imaging of the flow under microfluidic multipole. Moreover, the resolution achieved was good and this resin as a relatively low viscosity (for a UV sensitive resin) which allows for an easy flushing of the uncured resin out of the channels after the print.



Figure 4.4 Asiga Pico 2 HD 3D printer

3D printed component required post-processing prior to being used. 3D printed multipoles were sonicated for 3 min in an isopropanol bath. The residual resin in the channels was then flushed by plugging a tube in the channel opening and flowing isopropanol through it. The MFMs were then sonicated for 3 more minutes in an isopropanol bath. The devices were then cured in a UV oven to complete the cross-linking of the UV sensitive resin. Multipoles were connected to the pumps systems using Tygon tubes. Tubes were simply plugged into place and glued using UV sensitive resin.

4.3 3D Printed microfluidic multipoles results & discussion

This fabrication method has been used successfully for simple microfluidic probe, up to large PCD of up to 313 apertures (Figure 4.5). It allows to reliably fabricate microfluidic multipole with apertures of 160 μm . The printing time range from 25 minutes (for thin systems with a thickness of 1 cm) to 2h30 for PCDs comprised of hundreds of apertures (and a thickness of around 5 cm).

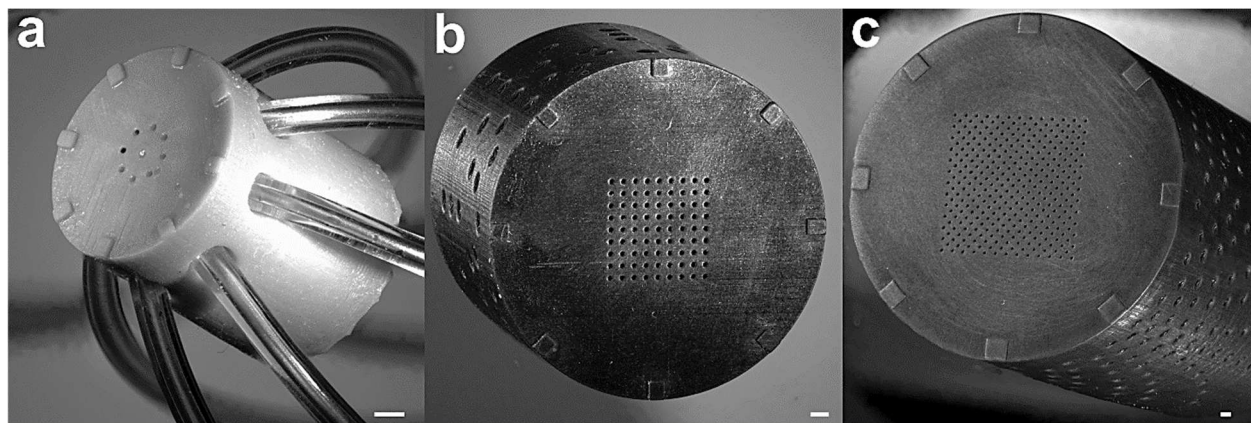


Figure 4.5 3D printed MFM. a) an 8-petal "flower" MFM. b) An 81-aperture PCD. c) A 313-aperture PCD. Scale bar represents 1 mm.

One advantage of 3D printing is the possibility to create real 3D features. Moreover, the fabrication method is not greatly influenced by the printed system geometry, as long as a few design rules are respected (mostly that channel with a length higher than a 3 mm should have a diameter of at least 300 μm , and that no aperture or small details should be positioned on the build tray). That has proved to be useful in the adaptation of multipoles to different experimental setup. The shape and size of probes can easily be changed. This versatility has allowed the fabrication of MFMs

compatible with positioning systems, as well as systems that used autoalignment spacers at their tip to control the gap between the multipole and the surface. Figure 4.6 presents two examples of experimental setup, one using a positioning system, and one where the MFM is using autoalignment spacers. Other setups were also used during this research project, such as the integration of a PCD with a roll-to-roll systems. These experimental setups will be presented in later chapters.

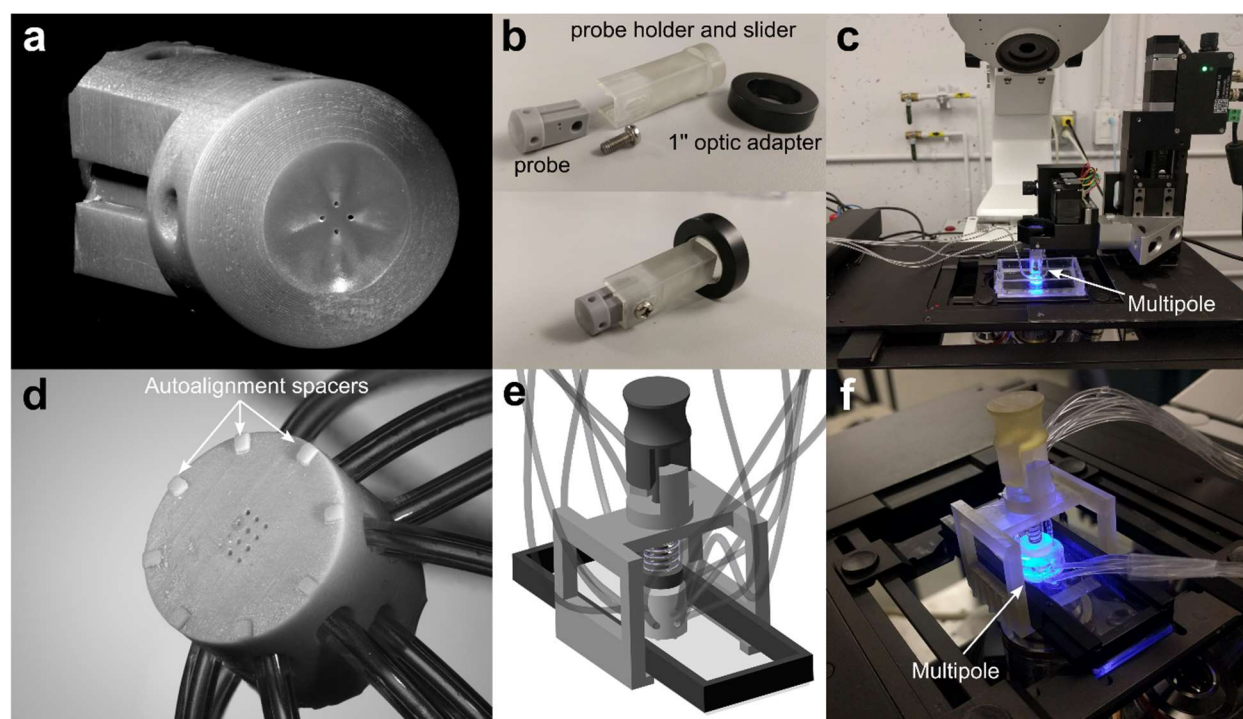


Figure 4.6 MFMs using a positioning system and autoalignment spacers. a) A 3D printed microfluidic quadrupole compatible with a positioning system. b) Positioning system slider and probe holder. c) Microfluidic Probe positioning systems. d)-f) 12-aperture MFM with autoalignment spacers.

Early in the research project, there was some doubt that the 3D printed systems would have reliability issues due to the relatively low printer resolution. It was feared that MFM would not reliably follow the models due to imprecisions in the fabrication. MFM models consider a perfectly flat surface, a perfectly parallel alignment between the multipole, the surface, and the point source apertures. Of course, it is impossible to build systems with point source apertures, but this discrepancy between models and experimental systems was previously demonstrated as not

significant⁹⁸. Nonetheless, a warped or unparallel surface would lead to a deviation between the observed flow patterns and the models. However, as the next figure presents, fabrication imperfection due to the 3D printing were found to have little effect on the observed flow patterns. Figure 4.7 and Figure 4.8 respectively present flow line and confinement area envelop comparison between models and experimental MFMs.

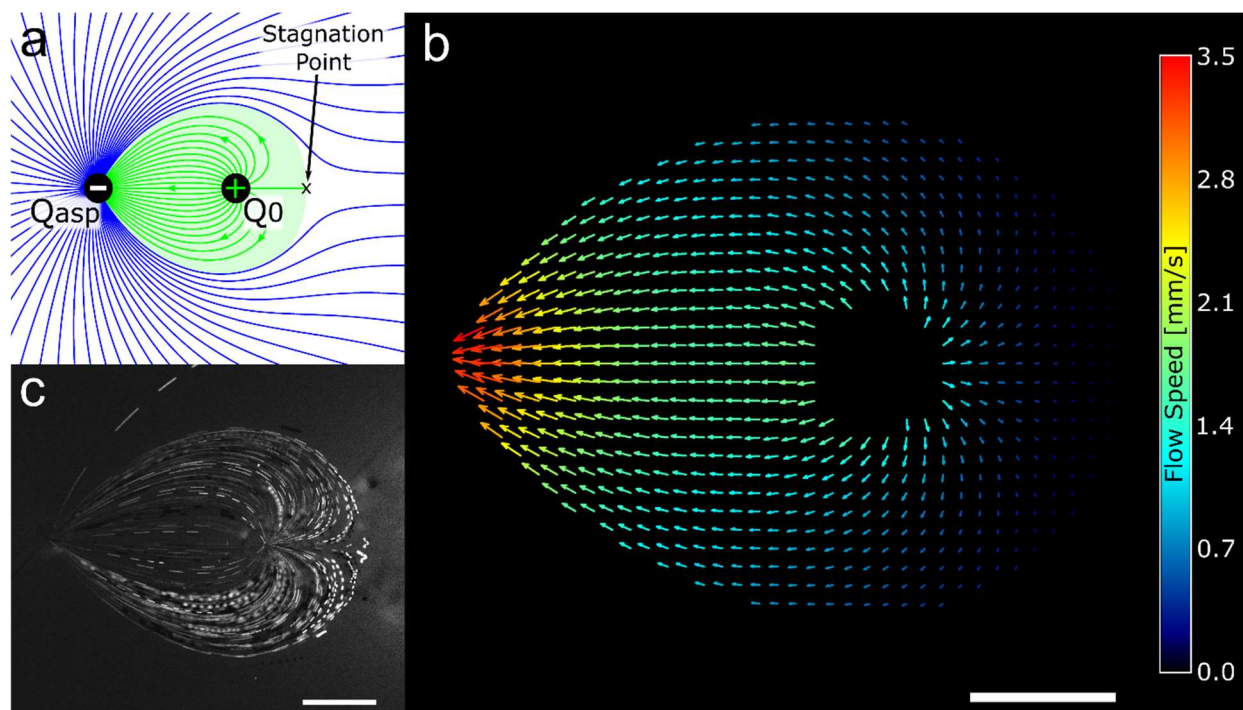


Figure 4.7 PIV measurements of the flow under a 3D printed microfluidic dipole. a) Potential flow streamlines under a microfluidic dipole. b) Average of 200 PIV measurements presenting the orientation and magnitude of the flow under the dipole. c) Fluorescent beads streamlines. Scale bar represents 500 μm .

Figure 4.7 presents the potential flow model streamlines and experimental streamlines of a microfluidic dipole. Experimental measurements were taken using particle image velocimetry (PIV) (Figure 4.7b). There was a concern that the 3D printed multipoles surface would be warped, which would have caused the flow line to be deformed. However, it is possible to see from this figure that the flow lines are symmetrical and show no sign of steep change of direction that would indicate the presence of important surface defects. Moreover, they follow the streamlines from the potential flow model (Figure 4.7a).

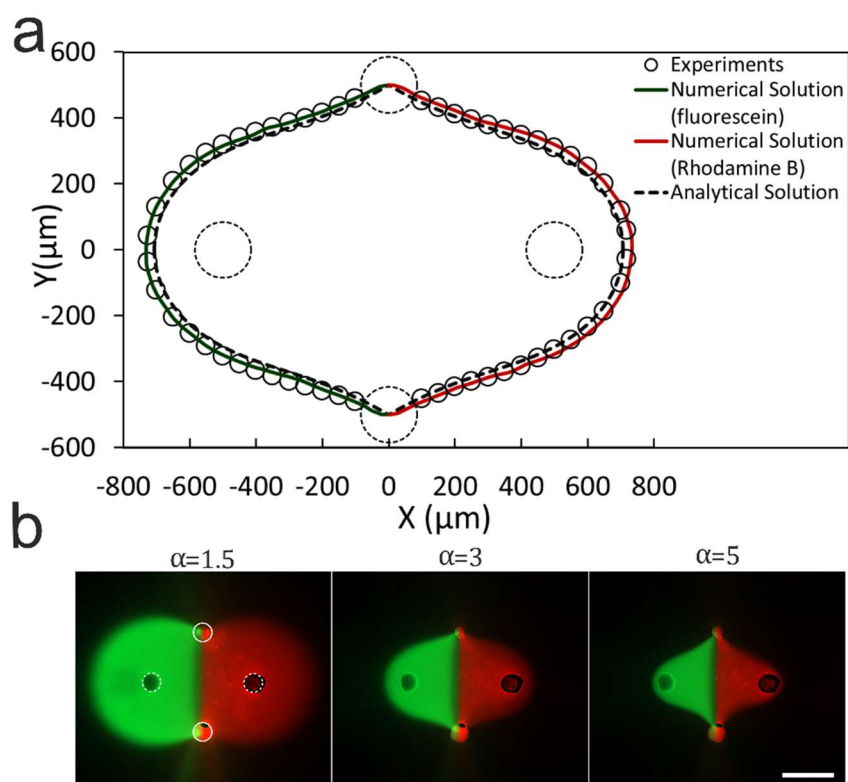


Figure 4.8 a) Comparison between the envelope of a microfluidic quadrupole for experimental data, a 3D finite element simulation and the analytical solution based on potential flows. Aspiration to injection ratio (α) equal to 3. b) 3D printed microfluidic quadrupole with different aspirations to injection ratio. Scale bar represents 500 μm .

Figure 4.8 compares the confinement area envelope for a 3D printed microfluidic multipole, a 3D finite-element simulation, and the potential flow analytical solution. A good fit was found for the three sets of data. The confinement area difference between experimental, simulation and analytical model is under 5%. The analytical model underestimates the confinement area size by approximately 25 μm on all borders, which can be explained by the fact that the analytical model considers point source apertures⁹⁹.

As the last figures presented, 3D printed microfluidic multipoles flow patterns are in agreement with the expected results. Both convection and diffusion are consistent with the potential flow model as well as the simulations. While 3D printing cannot compete with microfabrication in terms of fabrication tolerance, results show that it is possible to fabricate perfectly operable and predictable MFM using this method.

In conclusion, this chapter covered the whole fabrication process, from the CAD design to the 3D printing post processing. It was also demonstrated that the 3D printed MFM functioned as expected. While having its limitation, this fabrication method allowed the fabrication of countless devices with various parameters and applications. Moreover, all equipment and consumables required for this method are commercially available and are relatively cheap in comparison to the alternative. Using the process I developed, non-experts should be able to modify the CAD (by simple modification to the scripts parameters), print, assemble and operate open-space microfluidic devices.

CHAPTER 5 MULTIPLEXABLE AND RECONFIGURABLE MICROFLUIDIC MULTIPOLES

Objective #2: Develop, test and characterize multiplexed open-space systems of limited size.

This chapter covers the design, operation and application of small-scale reconfigurable microfluidic multipoles. It can be viewed as a revised and more detailed version of the second part of the article “Microfluidic multipoles theory and applications” that I co-wrote with my colleague Étienne Boulais⁹². This article originally started by presenting a convection-diffusion analytical model for MFMs. This model is omitted here since it was briefly presented in Chapter 3, and because it is my colleague’s research and not mine.

When I started my project, all open-space microfluidic devices were based on the concept of the scanning probe. This is extremely limiting for some applications. The time required to execute an experiment repeating “ n ” times a process lasting “ t ” second will scale with $n \cdot t$ when using a serial approach. Using a parallel device, the time to perform the same experiment would remain equal to t . This chapter covers the first step we took into multipole parallelization, in which the multipoles are multiplexable, reconfigurable, and fixed on the surface. This allows the MFMs to perform parallel, multistep and long-term experiments.

This part of my project is an exploratory phase with multiplexable and reconfigurable MFMs. MFMs were voluntarily kept somewhat simple and limited in their number of apertures. In this regard, this chapter revolves around the second objective of my thesis, which is to experiment with MFM limited in size. While this limited the parallelization potential of the systems presented here, it was sufficient to explore many MFM geometries, study reconfigurable MFM dynamics and do a proof of concept of an automatized immunoassay.

5.1 Scanning device limitations

At the start of my project, all published open-space microfluidic systems were operated on the scanning probe logic. Different microfluidic probe configuration existed, such as the hierarchical MFP¹⁰⁰ or the microfluidic quadrupole¹⁰¹, but they all greatly lacked parallelization. More recently, Taylor & al. presented a probe based on an array of dipoles that offered a somewhat parallelization

potential¹⁸. However, even this system was made to be used as a scanning device. Scanning is inherently a serial process, and a limitation the parallelization. Any experiment requiring the reagent residence time to be more than a few second become impractical with this kind of system. Experiment requiring various reagents are also impractical, and require a time increasing linearly with the number of conditions to be tested. A solution to the currently used systems limitations is to use a parallel approach, and design systems that allow multiplexing. Such systems would enable the patterning of different reagents simultaneously and the creation of multiple confinement areas. This idea can be pushed one step further by adding reconfiguration to the MFMs, which would allow those systems to carry out multistep experiments.

Scanning probes are mainly limited to cell staining and surface patterning application requiring residence time in the orders of seconds. The goal behind the design of multiplexable reconfigurable multiple is to create systems that can tackle long multistep experiments, such as immunoassays or dynamic cell perfusion.

5.2 First explorations of the MFM configurations

The first step toward multiplex reconfigurable MFMs was to explore the various configurations possible. We started by fabricating and testing simple MFMs, some of which based on configurations already demonstrated in the literature, such as the dipole and quadrupole (Figure 5.4a & b). It served two purposes. The first one was to develop a reliable experimental protocol on how to operate and evaluate the concentration profile of MFMs. Using already known designs simplified the debugging phase. The second one was to validate my colleague's convection-diffusion model based on conformal mapping. Having a matching model would mean that the concentration profile of our new devices could be predicted without the use of time-intensive finite element simulations.

The standard MFM imaging protocol developed for this research project revolves around the use of a fluorescent inverted microscope to measure MFM concentration profiles. Fluorescein is used as a concentration marker. Propidium Iodide mixed with DNA serves as a second marker when two colors are needed (DNA increases the propidium iodine fluorescent yield). Rhodamine B was previously tested but strong surface adsorption with the MFMs diminished the image quality. A background image of the system with all apertures turned off was frequently removed from the

fluorescent images to simplify the image analysis. MFMs were operated using Cetoni Syringe pumps. A Labview code was developed to control the pumps for both stationary and reconfigurable experiments. MFMs were fabricated with autoalignment spacers. It allowed the precise control of the gap in between the MFM and the surface. MFMs were simply clipped on the surface using a custom 3D printed holder and a spring latching mechanism (Figure 5.1). It is a major difference with previous work on microfluidic probes that used complicated positioning system based on costly scanning motorized system. We could rely on such a simplified system since the aim of this project is to design reconfigurable systems that address specific points of a surface through multiplexing and reconfiguration rather than scanning. For reliable use, the multipoles were printed with autoalignment spacers that are of a thickness that makes the surface unevenness negligible (MFM fabricated to operate on tissue slice had thicker spacers than MFM fabricated to operate on perfectly flat glass slide).

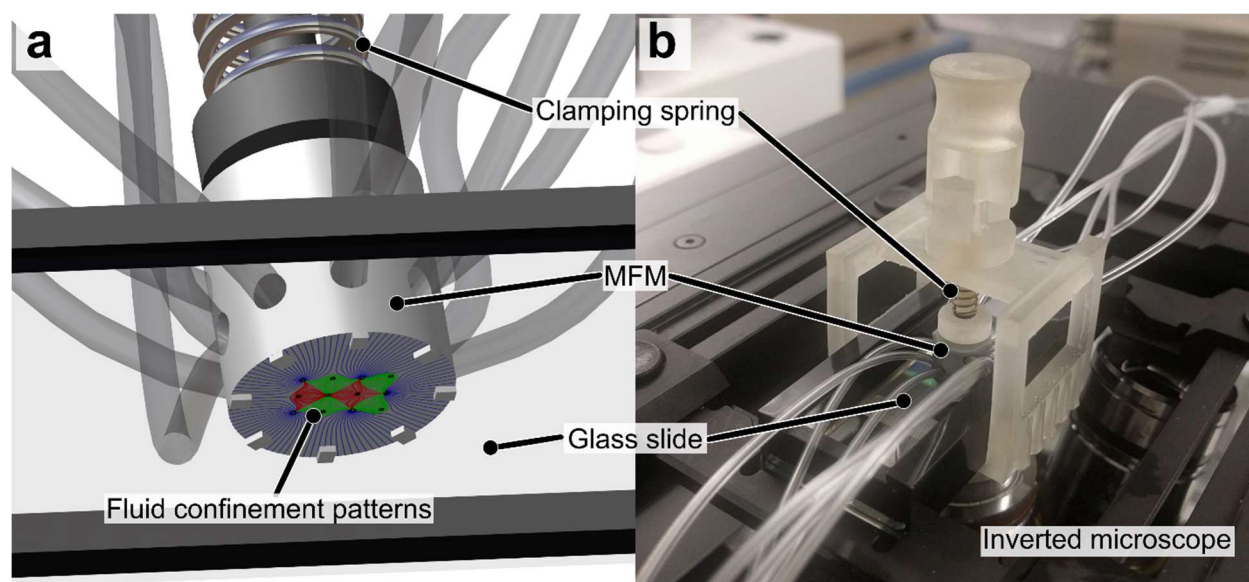


Figure 5.1 a) Schematics of a fixed MFM setup. The MFM is precisely positioned over the surface with a gap controlled by the auto alignment spacers. b) Picture of the experimental setup with a holder and a MFM clamped on an inverted microscope. Figure modified from Goyette & al. *Nat. Commun.* (2019)⁹². License CC BY 4.0 <http://creativecommons.org/licenses/by/4.0/>.

Experimental results from early MFMs were found to match convection-diffusion model of my colleague Étienne Boulais, as presented by Figure 5.2 and Figure 5.3. Figure 5.2 shows that the diffusion lengths and the concentration profile observed with a 3D printed dipole are consistent at

different angles on the profile (the diffusion length varies along the profile). Figure 5.3 demonstrates that the envelopes of the confinement areas match those predicted by the analytical model for various geometries. Those results validated our idea that the analytical model could help in the design of new MFM configurations. The idea was to use known MFM solutions such as the dipole and quadrupole and transform them into more complex geometries.

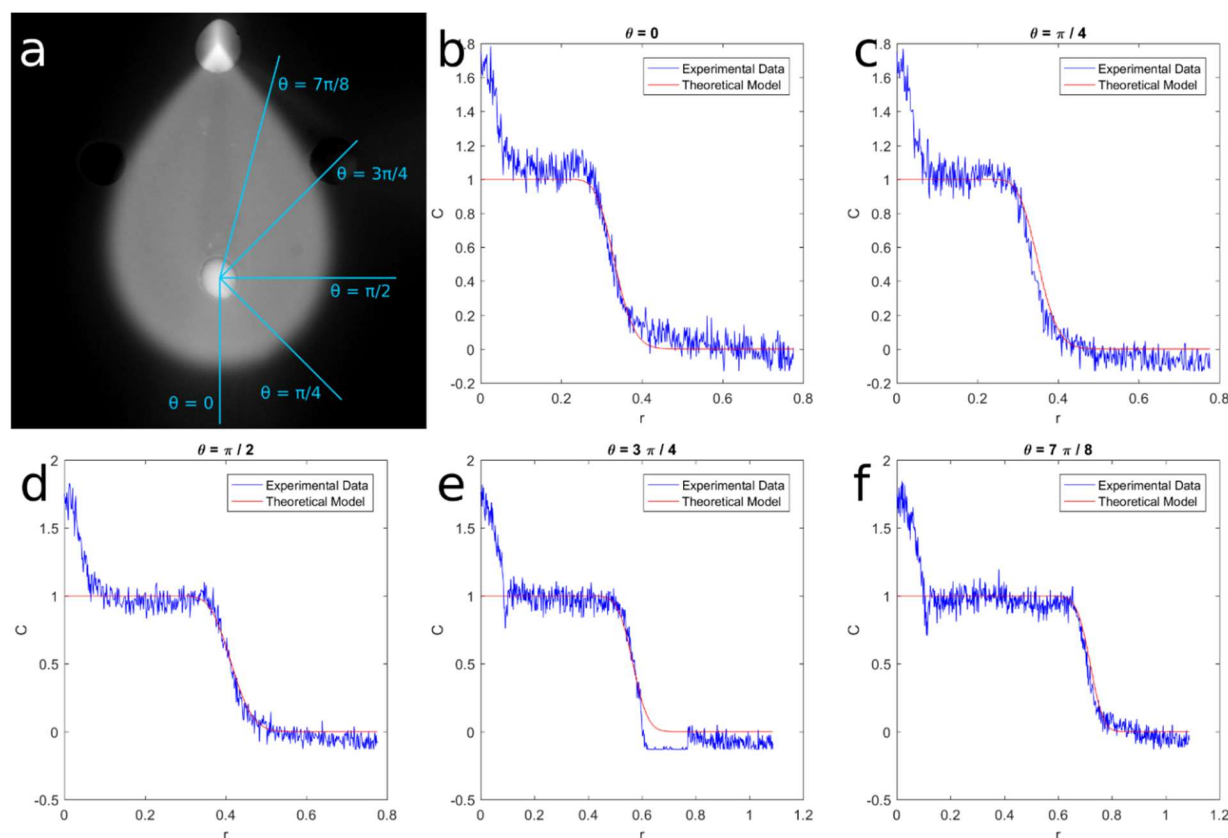


Figure 5.2 Comparisons between the theoretical model and experimental results for different cross-sections of a microfluidic dipole. How each cross-section maps to the experimental image is illustrated in a), while b)-f) show the comparison of experimental and theoretical concentration. The diffusive species used is fluorescein. (Figure from supplementary information, of Goyette & al. Nat. Commun. (2019)⁹². License CC BY 4.0 <http://creativecommons.org/licenses/by/4.0/>).

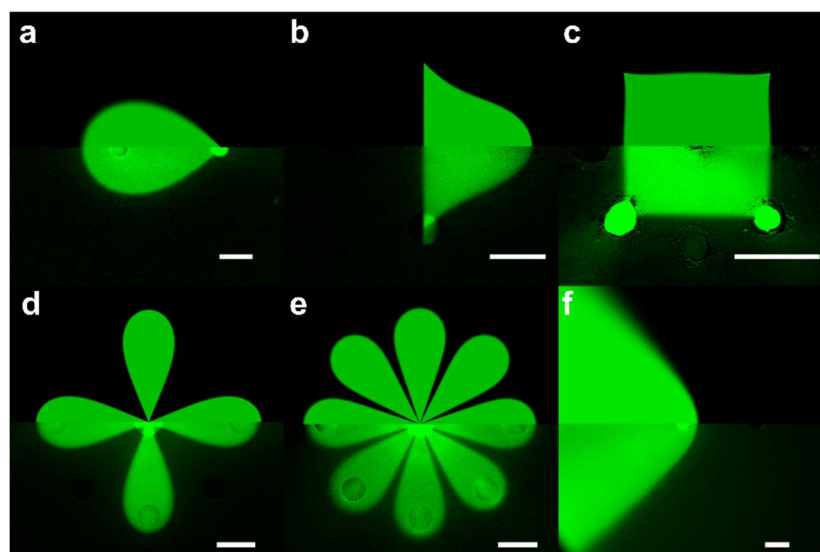


Figure 5.3 Experimental setup and side-by-side comparison between theory and experiments. For each subfigure, the top half represents the theoretical concentration profile, and the bottom half is a fluorescent micrograph of an MFM injecting a fluorescent dye. a) Microfluidic dipole. b) Microfluidic quadrupole. c) Polygonal multipole d) 4-petal axisymmetric “flower” multipole e) 8-petal axisymmetric “flower” multipole f) Asymmetric impinging flows. $Pe \sim 100$. Scale bars represent $500 \mu\text{m}$. Figure modified from Goyette & al. *Nat. Commun.* (2019)⁹². License CC BY 4.0 <http://creativecommons.org/licenses/by/4.0/>.

MFM design from conformal mapping led us to two configurations that would prove out to be useful for this project. They are the “flower” and polygonal MFM families (Figure 5.3c-e). Both these MFM configurations are based on the same $z^{1/n}$ conformal transform. This mapping compresses the complex plane in $1/n^{\text{th}}$ of the complex plane and replicate the new domain n time, resulting in a polygonal symmetry. Using a translation before this transformation, both types of MFMs were generated (Figure 5.3d-f & Figure 5.4). The “flower” or rotationally symmetric MFM is an effective MFM geometry that is easily reconfigurable, as it will be further described in the next section. The Polygonal MFMs generate a confinement area in the shape of a regular polygon. It was found to be extremely stable during experiments. While not being useful at this stage of my project, it is one of the inspirations behind the microfluidic pixel and highly scalable systems presented in chapter 6.

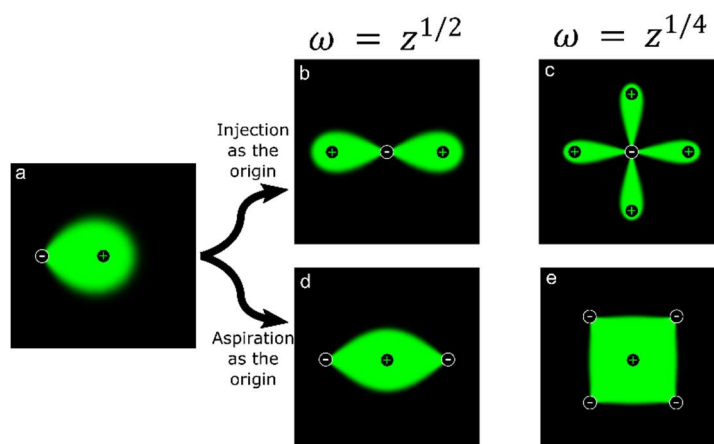


Figure 5.4 Microfluidic multipole generation from the conformal transform $\omega = z^{1/n}$. a) A microfluidic multipole. b) Using the aspiration as origin, a 2-petal axisymmetric “flower” multipole can be generated from the dipole. c) A 4-petal axisymmetric “flower” multipole. d) Using the injection as origin, microfluidic polygons can be generated. e) Polygonal MFM.

Other multipole configurations that were inspired by regular and staggered array of apertures rather than conformal transformations were also investigated. They were found promising for reconfiguration due to their versatility.

5.3 Microfluidic multipole reconfiguration

Different approaches can be used to create reconfigurable multipoles. The most evident one is to create systems where the reagent injected by apertures can be changed over time. However, it is technically difficult to achieve, and not essential for relatively small multipoles. It will be covered in the next chapter on display-like MFMs. As a first step toward reconfigurable MFMs, we used a simpler approach. MFMs were reconfigured by changing the flow rate and turning apertures on and off. This reconfiguration method is simple when using programmable pumps. Moreover, the number of patterns that can be generated (considering that apertures can only be turned on or off) scale with 2^a , where “a” is the number of apertures. For a 12-aperture MFM, it corresponds to 4096 fluid patterns.

From our exploration of microfluidic multipole geometry, two designs stood out as promising for multiplex and reconfigurable MFM applications. They are the rotationally symmetric multipole

(rMFM) (Figure 5.4a &c), also sometimes referred as the flower configuration, and the translationally symmetric MFM (tMFM) (Figure 5.5b &d), based on arrays of apertures.

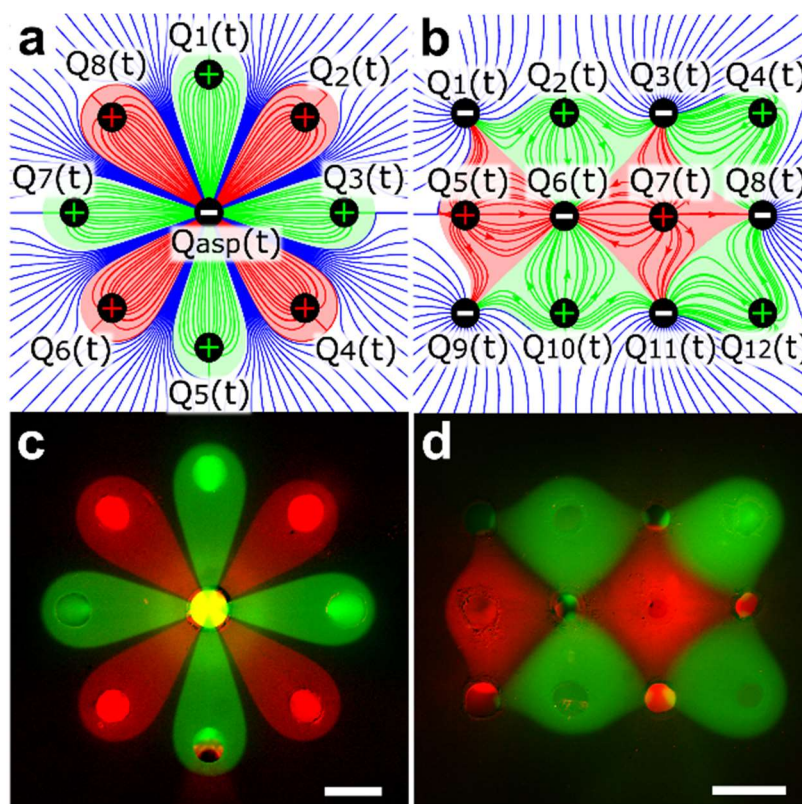


Figure 5.5 Reconfigurable multipole. Theoretical streamlines (a–b) and fluorescence micrograph (c–d). Positive and negative signs represent injection and aspiration apertures. a), c) MFM with rotational symmetry. b), d) 12-aperture MFM with translational symmetry. Scale bars represent 500 μm . Figure modified from Goyette & al. *Nat. Commun.* (2019)⁹². License CC BY 4.0 <http://creativecommons.org/licenses/by/4.0/>.

The rotationally symmetric microfluidic multipole (rMFM) is based on the idea of radially oriented dipoles with a superposed central aspiration. The injections are positioned at the corner of a regular polygon around the central aspirations. The rMFM is the configuration that allows the largest theoretical number of confined reagent conditions per apertures (since they are all injections except for the central aspiration).

A proposed use of the rMFM is to create a chemical stroboscope. Turning on and off the injections of the rMFM enable the fast spatiotemporal control of pulses of reagent above a surface. “Petals” can be pulsed at different rates and duty cycle. Figure 5.6a & b present a chemical

stroboscope we fabricated. It presents an experiment in which different “petals” are pulsed at different frequencies (period = 12s, 24s and 24s) and different duty cycle (25% and 50%). Two petals serve as controls (one always on and the other always off). The pulse transition time is in the order of seconds. In theory, the petals width and shape should be affected by the number of petals turned on at any moment. However, the petals could be kept at a fixed width throughout the experiment by modulating the aspiration to injection flow rate ratio in real time. The ratio of aspiration to injection to keep the petals stable was calculated from the potential flow model. More information on the injection to aspiration ratio correction is available in the appendix B. Supplementary micrographs showing the chemical strobe during use and other rMFM reconfiguration are available in the appendix C.

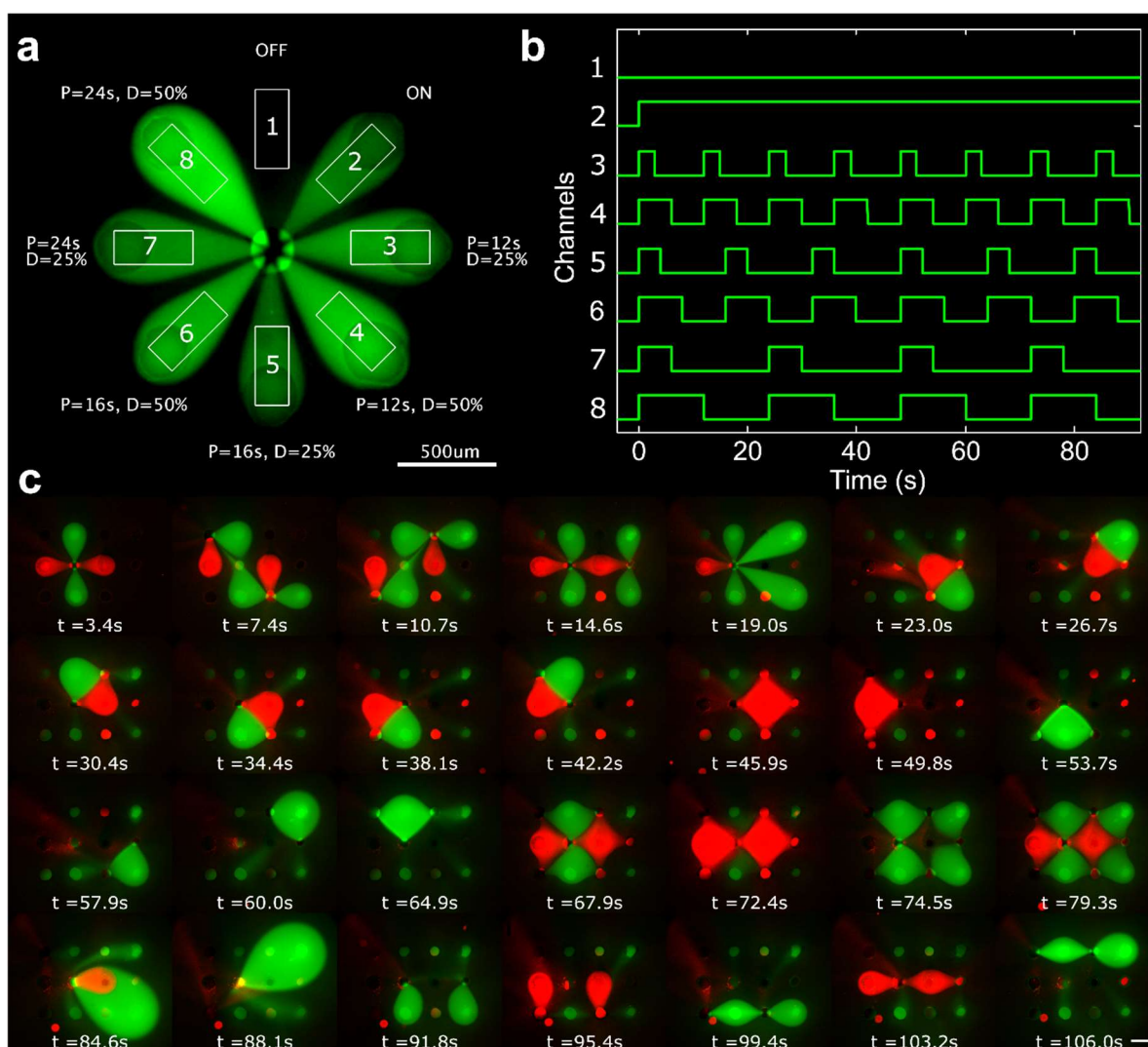


Figure 5.6 Microfluidic multipole devices. a) Fluorescence micrograph showing the confinement pattern of a rMFM device. b) Graph representing the periodic exposure to reagents for each confinement area of a rMFM used as a chemical stroboscope. c) Fluorescence micrographs showing 28 different confinement patterns made with a 12-aperture tMFM during a single experiment lasting less than 2 min. Scale bar represents 500 μm . Figure from Goyette & al. Nat. Commun. (2019)⁹². License CC BY 4.0 <http://creativecommons.org/licenses/by/4.0/>.

The translationally symmetric MFM (tMFM) is based on the idea of creating a regular array of apertures. When it was fabricated, every MFM presented until then (dipole, quadrupole, hierarchical) could be achieved using this multipole and the appropriate injection and aspiration placement. By alternating the placement of injection and aspiration (Figure 5.6b and Figure 5.7c), the tMFM yields a versatile device that can generate a different pattern, a lot of which including overlapping. In Figure 5.6, we present the reconfiguration of a tMFM to generate 28 different fluid patterns. It was performed in a single experiment that lasted less than 2 minutes. These figures are simply a subset of the 4096 fluids patterns that could be generated using this design. Moreover, a different placement of injection and aspiration yield totally different set of 4096 chemical patterns, as presented by Figure 5.7, that presents a second configuration and the fluids pattern that were generated. More figures of reconfigurable tMFM are available in the appendix C.

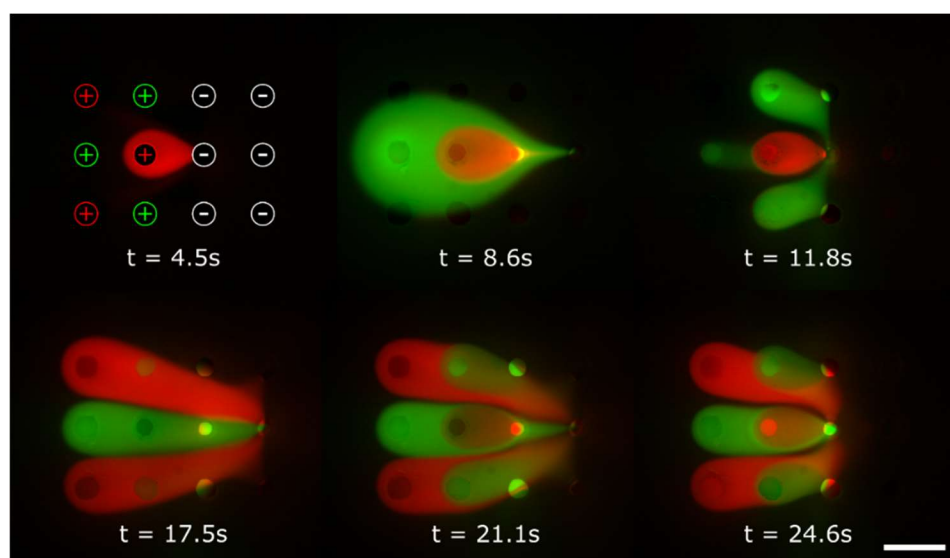


Figure 5.7 Fluorescence micrographs showing 6 different confinement patterns made with a 12-aperture tMFM during an experiment lasting 30 seconds. Scale bar represents 500 μm .

5.4 Reconfigurable MFM immunofluorescent assay

As a proof of concept of the potential of reconfigurable MFM to automatize long-lasting multistep experiments, we carried out an immunoassay experiment using a 12-aperture staggered tMFM. The goal was to fully automate an immunofluorescent assay that has 3-steps; antigen incubation, detection antibody incubation and washing. The experiment was performed on a slide

functionalized with spots of goat IgG anti-mouse capture antibodies. In a first step, the 7 centermost apertures were used as a rMFM, the central apertures serving as a drain, and the 6 others each injecting a different concentration of the antigen (mouse anti-human IgA heavy chain) (Figure 5.8a). The antigen was incubated for 50 minutes. The antigen injections were then turned off, and the 4 corner apertures were used to inject the detection antibody (fluorescent labeled Donkey anti-Mouse IgG) for one hour (Figure 5.8b). The pattern of injection of the detection antibodies overlapped the pattern of the antigens. After the detection antibodies incubation, the injections were turned off for 10 seconds to allow the central drains to aspirate the remaining detection antibodies. The central drain was then turned off, and the last aperture was then started to inject a wash buffer (PBS and tween) for 15 minutes (Figure 5.8c). The MFM was then removed, and the slide dried with nitrogen, before being imaged. Results present well define patterns without crosstalk (Figure 5.8d). The fluorescent level for the 6 antigen concentrations was used to generate the binding curve of the assay (Figure 5.8d). The area unexposed to antigen but exposed to the detection antibodies was used as background signal level. Previous experiments showed similar levels between this area and injecting confinement area to inject a solution with null concentration (more information in appendix D). The binding curve gives the assay a limit of detection (LOD) of 13 pM/ml (~ 2 pg/ml), which is in the range expected for any state-of-the-art sandwich immunoassay¹⁰². This immunoassay is the first proof of concept of a multistep experiment automated using an open-space microfluidic system. While it remains limited by allowing the test of only 6 experimental conditions, it is also the first demonstration of the use of open-space systems for experiment requiring long incubation time. It paves the way toward large-scale multistep automatization of life science experiments where microfluidic multipoles could be used instead of pipetting robots.

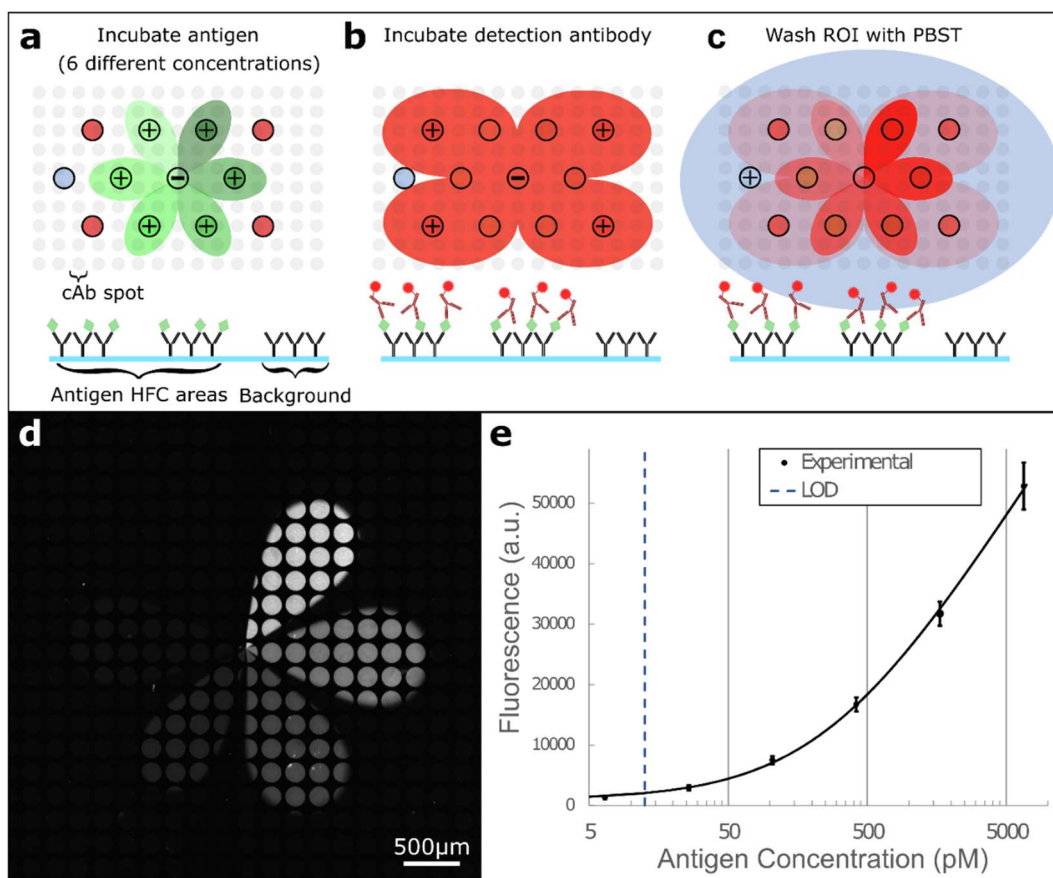


Figure 5.8 Immunoassay experiments using a staggered tMFM microfluidic multipole. a)–c) Workflow of an immunofluorescence assay using a MFM. a) Antigen incubation. The device is used as a 6-petal rMFM to incubate 6 different concentrations of antigen on the capture antibodies. b) Detection antibodies incubation. The corner apertures are then used to expose the previous areas with detection antibodies. c) Wash. A washing buffer is injected by the last aperture. d) Resulting micrograph of the detection antibody on the glass slide. e) Experimental binding curve of the immunoassay. Error bars represent the standard deviation over 6 spots. Figure from Goyette & al. *Nat. Commun.* (2019)⁹². License CC BY 4.0 <http://creativecommons.org/licenses/by/4.0/>.

5.5 Discussion

The MFMs presented in this chapter have two important improvements over previously presented microfluidic probes: multiplexing and reconfiguration. The major implication of these improvements is the compatibility with long-lasting experiments. By handling parallel experiments in the time range of minutes to days, they bring out new possibilities. Immunoassays are ubiquitous in life science, but MFMs would not be limited to those experiments. They could be used for immunohistochemical (IHC) staining, DNA hybridization¹⁰³, or cellular barcoding¹⁰⁴. Moreover, since MFM are based on constant streaming, they remove the need for tedious washing steps in between the injection of different reagents and they have no dead volumes (left over liquid volume from the previous step that could not be rinsed). While insignificant for experiments based on a few steps, it might be a huge advantage for experiments requiring the sequential incubation of tens of reagents such as in cellular barcoding.

MFMs presented in this chapter have fast dynamics, especially the chemical stroboscope that allows transition in the order of seconds. We envision the use of the rMFM chemical stroboscope to study cellular pathways that are frequency dependant^{105–108}. Some cell signaling pathways, such as the Notch pathway, results in distinct target gene programs depending on the frequency of exposure to a molecule or stimulus rather than the level of exposition¹⁰⁹. The study of such pathway is difficult using standard pipetting protocols, which are normally used to study dose response. The chemical stroboscope could offer a new tool to study such phenomena.

Compared to previous scanning microfluidic probes, reconfigurable MFMs require simpler positioning systems that can be based on simple latching mechanisms. Beside reducing the positioning system cost and complexity, it simplifies the MFM integration with incubators or imaging systems.

By design, MFM allows the test of different experimental conditions on a small footprint. Different conditions can be tested within a small area without physical barriers (such as walls or wells), while maintaining biochemical isolation. In this regard, the reconfigurable MFM allows the biochemical isolation offered by well plate or closed-channel microfluidics, while offering the compatibility with open surfaces like the microfluidic probe.

As showed in this chapter, MFM multiplexing potential increases with the number of apertures. I, however, have limited myself to systems comprised of up to 12 apertures for this part of my research project. Keeping the systems simple for an easy troubleshooting was not the only reason. Every aperture of MFM in this chapter are individually controlled by a syringe pump. Syringe pumps being expensive and thus limited in number, it became evident that the use of manifold would become essential to increase MFM multiplexing. It is an important lesson that was learned from the work of this chapter. The use of manifold, combined with concepts developed in this chapter, more particularly the MFMs based on an array of apertures and the polygonal MFMs, are the basis that led to the creation of the pixelated chemical display. These systems are presented in the next two chapters. Those newer versions of large-scale MFMs were designed to mitigate the limitations of small reconfigurable MFMs, namely the lack of massive parallelization potential.

CHAPTER 6 ARTICLE 1 : PIXEL-BASED OPEN-SPACE MICROFLUIDICS FOR VERSATILE SURFACE PROCESSING

Pierre-Alexandre Goyette¹, Étienne Boulais², Maude Tremblay², Thomas Gervais^{1,2,3}

¹ Institut de Génie Biomédical, Polytechnique Montréal, Montréal, QC, H3T 1J4, Canada

² Department of Engineering Physics, École Polytechnique de Montréal, Montréal, QC, H3T 1J4, Canada;

³ Institut du Cancer de Montréal, Centre de Recherche du Centre Hospitalier de l'Université de Montréal, Montréal, QC, H2X 0C1, Canada

Objective #3: Develop, test and characterize a scalable and highly parallelizable open-space microfluidic system.

6.1 Background information

This article was published on January 12th, 2021, in the Proceedings of the National Academy of Sciences of the United States of America (PNAS). It describes the design, fabrication, and operation of pixelated chemical displays (PCDs), which are highly parallelizable MFMs. One of the main contributions of this article is the architecture of the PCD. It is modular, which makes it possible to create simple systems or generate large arrays comprised of hundreds of fluid confinement areas using the same basic “pixelated” design (and thus using the same design rules). The article covers the use of manifolds to operate the PCDs, and how to achieve basic reconfiguration. Some surface processing applications are presented but remain somewhat limited in comparison with the potential of the PCDs. I consider the finding in this article, especially the PCD architecture, to be the centerpiece of my PhD, at least in terms of system design. While I view the MFM systems from previous chapters as proof of concept or unfinished design, I think that the pixelated architecture presented in this chapter is a mature design that has some potential for industrialization. It is highly multiplexable, stable and enables reconfiguration, which are the 3 characteristics I was looking for. The challenge that remains lies in the control systems that feed

the PCD, more than in the device architecture itself. The supplementary information of this article is presented in the Appendix E of this thesis.

My contribution to this article is around 75%. I designed, performed, and analyzed all the experiments present in the paper. I wrote the article, except a part of the introduction written by Thomas Gervais. While I designed the stability analysis, and analyzed the result, the simulations and the codes to generate them were made by Maude Tremblay, a summer intern that I supervised. The analytical model presented in the supplementary information (appendix E) is the work of Étienne Boulais.

6.2 Abstract

An increasing number of applications in biology, chemistry, and material sciences require fluid manipulation beyond what is possible with current automated pipette handlers, such as gradient generation, interface reactions, reagent streaming, and reconfigurability. In this article, we introduce the pixelated chemical display (PCD), a new scalable strategy to highly parallel, reconfigurable liquid handling on open surfaces. Microfluidic “pixels” are created when a fluid stream injected above a surface is confined by neighboring identical fluid streams, forming a repeatable flow unit that can be used to tessellate a surface. PCDs generating up to 144 pixels are fabricated and used to project “chemical moving pictures” made of several reagents over both immersed and dry surfaces, without any physical barrier or wall. This work distinguishes itself from previous work in open-space microfluidics by presenting the first device architecture where the number of confinement areas can be scaled to any size. Furthermore, it challenges the open-space tenet that the aspiration rate must be higher than the injection rate for reagents to be confined. Overall, this article sets the foundation for massively parallel surface processing using continuous flow streams and showcases new possibilities in both wet and dry surface patterning and roll-to-roll processes.

6.3 Significance Statement

Automated liquid handling is of utmost importance for life sciences, pharmaceutical research, and surface engineering. Despite its ubiquitous presence, last decades advances in this domain have mainly consisted in the robotization of the human pipetting movement, with its intrinsic limitations.

In this article, we lay the foundation for the Pixelated chemical display (PCD), a liquid handling system based on open-space microfluidics. This device uses the streaming of fluids through independent flow subunits to tessellated surface with hundreds of reagents simultaneously. PCD distinguish themselves from previous technology by offering a fast dilution-free reagent switching and a precise yet multiplexable spatiotemporal control of fluids on surfaces. PCDs will be of use in life sciences and for maskless surface processing.

6.4 Introduction

Since the turn of the century, automated liquid handling (ALH) technology has become ubiquitous in academic and industrial laboratories and at the core of a revolution in the life sciences, chemistry, and material sciences^{2,21}. Yet, from a technological point of view, in the vast majority of cases, ALH embodiments remain a mere robotization of the human pipetting movement. ALH systems can deposit small volumes of liquid extremely efficiently using multiple pipette heads simultaneously. However, they cannot expose surfaces to gradients of chemicals, nor can they replace medium without dilution or slow intermediate rinsing steps⁵. There is, meanwhile, an increasing demand for systems with a faster spatiotemporal control of chemical species, which can be explained by a growing interest in cellular pathway kinetics by both the synthetic biology and pharmaceutical domain^{6,106}.

In an attempt to free the life sciences from the “tyranny of pipetting”⁷, significant developments in the field of open-space microfluidics have brought new strategies for ALH compatible with well-based or petri-based assays. These include, among others, the microfluidic pipette¹¹⁰, the chemistode¹¹¹, the microchemical pen¹¹², and perhaps more importantly, the microfluidic probe¹³. All are contact-free methods which operate “from above” by continuously streaming reagents above an immersed surface. They can switch between two or more reagents quickly without dilution, enhance convective mass transport to surfaces, and generate sharp floating concentration gradients⁶². These technologies, however, are still inherently serial and slow. For example, the scanning speed of reagent-streaming devices is limited by the incubation time of the reagents involved in the surface reaction, often minutes to hours for protein-protein reactions (immunoassays) or cell stimulation (e.g. drug incubation). Finally, all open-space microfluidic systems developed so far can only operate on immersed surfaces since, for fluid confinement to

occur, more fluid must be aspirated from the probe than what is injected, with the excess taken from the immersion medium^{100,113,114}.

Circumventing limitations to both standard and microfluidic-based ALH requires a radical perspective change from inherently serial scanning methods to massively parallel, reconfigurable reagent dispensing, much in the way that the first real 2D displays, using liquid crystal displays (LCDs), replaced the first cathode ray tubes using a single scanning electron beam. In fluid processing, the concept of very large scale microfluidic integration eloquently demonstrated by Thorsen *et al.* almost two decades ago offers a path forward for static aliquots of fluids¹⁰. In this paper, we introduce the Pixelated Chemical Display (PCD), the ALH analog of a LCD, where a large number (100+) of independent reagent streams can be colocalized above a surface and reconfigured over time with discrete spatiotemporal control. We developed an exact first principles model to characterize mass transport under PCDs and provide experimental and theoretical evidence of their large-scale stability and robustness under flow perturbations or device imperfections. Devices are fabricated via a simple monolithic 3D printing process and used to demonstrate reagent confinement over both immersed and dry surfaces. In doing so, we challenge for the first time the received idea that open-space microfluidic devices must be operated immersed in fluids for reagents to be confined. Overall, the technology suggests a novel way to dynamically process surfaces by projecting “chemical moving pictures” onto them, which we exploit to propose broad applications in robotic liquid handling, roll-to-roll printing, and surface engineering.

6.5 Results and discussion

6.5.1 Pixelized chemical display concept

The key to develop a massively parallel open-space microfluidic system is to define a basic modular flow subunit, or microfluidic pixel, that can be indefinitely repeated over a surface completely. Microfluidic pixels are a special type of polygonal microfluidic multipoles⁹², where an injection is centered between three or more aspiration apertures that form the vertices of a polygon. Fluid is continually streamed through these apertures within the shallow gap formed between the device and the surface to be processed (Figure 6.1). Adjacent microfluidic pixels share aspiration apertures on their vertices to form a lattice of apertures which, for certain regular polygonal shapes,

can completely tessellate a surface with independent and isolated fluid confinement areas (Figure 6.1). The architecture of pixelated devices is highly modular as any number of columns or line of microfluidic pixels can be added on the periphery without affecting the inner units. Inside a single pixel, reagents are transported by convection but also diffuse, to a certain extent, in neighboring pixels in the lattice. The flow rate within a pixel and the diffusivity of the tracer (reagents, particles, heat) will determine the amount of interpixel transport taking place. Based on previous recent mathematical developments describing convection-diffusion transport problem in planar viscous flows (or Hele-Shaw flows¹¹⁵) and their early translation into microfluidics^{92,116}, we found an exact analytical solution for both streamlines and concentration profiles within pixels (Appendix E, section 2). We used this model throughout this paper as an experimental design tool to either minimize or exploit diffusional interfaces at the edge of the pixels in surface processing applications. Match between experiments and theory is outstanding for both diffusion and convection (Appendix E section 2, Fig. S8).

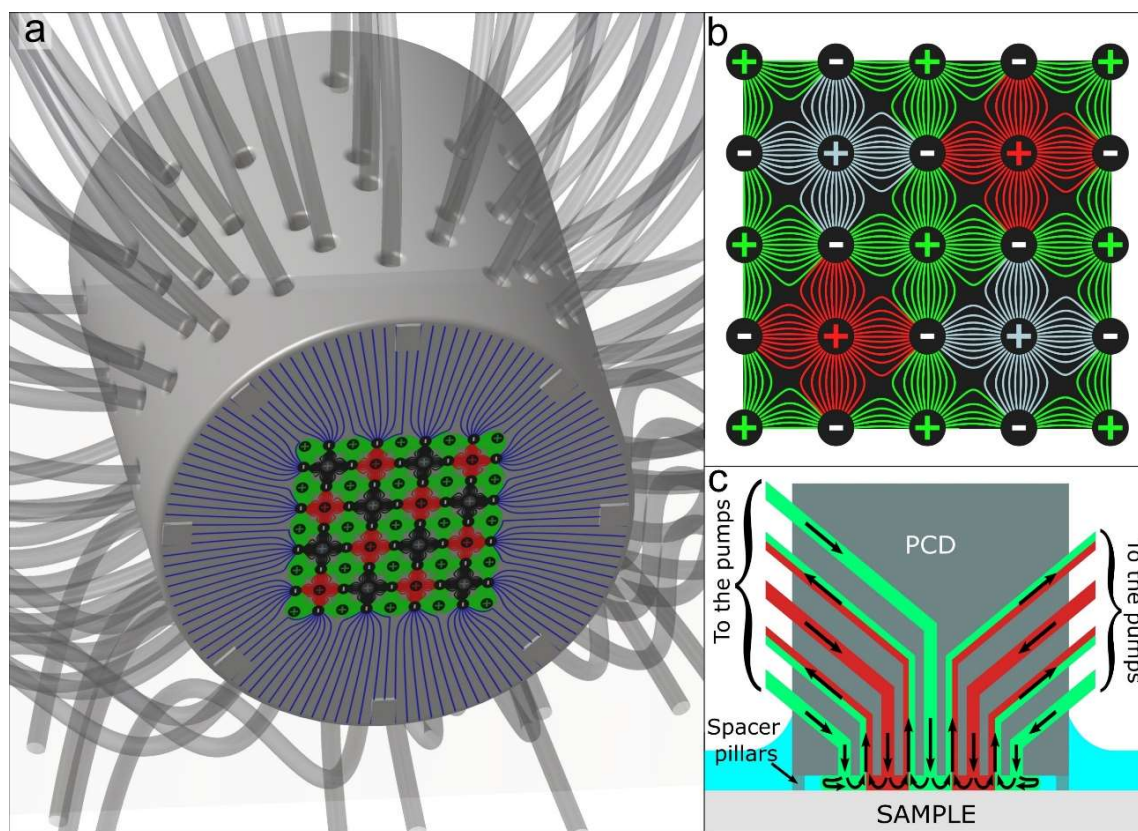


Figure 6.1 Pixelated Chemical Display concepts and schematic. a) Schematic presenting an 81-aperture square-pixel PCD. The PCD is held over a sample. Lines on the surface represent the flow lines. b) Theoretical flow lines in an array of microfluidic pixels under a PCD. Positive and negative signs represent injection and aspiration apertures, respectively. c) Side view cut schematic of a PCD. The PCD is maintained at a fixed height over a surface with the help of spacer pillars. Fluids are injected and reaspirated within the shallow gap formed between the surface and the device.

6.5.2 Display operation

We tested PCDs based on the only three possible regular tessellation patterns in planar 2D space (square, triangle, and hexagon). An 81-aperture rectangular array and a 92-aperture staggered array PCDs were 3D-printed using stereolithography and a method previously developed⁹⁹. To limit the number of pumps required, we designed custom-built manifolds to deliver fluids from one pump into all pixels sharing the same reagents. We also merged aspirations in two independently controlled groups (Appendix E, Fig. S1&S2), such that a PCD can be operated using a minimum number of pumps ($2 + X$, where X is the number of different reagents injected) no matter its size

or the chemical image generated. We used tubes connecting the manifolds to the PCDs as precision hydraulic resistors to match the flow rate from all apertures. Micrographs were taken using a fluorescence microscope through a glass slide that served as the sample surface (Appendix E, Fig. S3). The three-pixel shapes tested provided highly regular patterns (Figure 6.2).

In 2D periodic lattices, where every pixel shares a no flux boundary condition with its neighbors, having a zero net flow rate is the only method to preserve local mass balance. An exception is possible for the outermost pixels, where edge effects are present. A PCD with the edge pixels having a negative net flow rate, such as in Figure 6.2a-c, operates in the well-established hydrodynamic flow confinement regime^{34,113}. For any aperture configuration other than microfluidic pixels, including every previously published open-space microfluidic system, this regime is the only possible way to confine streaming reagents since, without a net aspiration from the device, they would diffuse to infinity and escape confinement. A restrictive condition on their operation ensues, which is that devices in hydrodynamic flow confinement must necessarily be immersed in a fluid to operate. In contrast, the unique 2D periodic symmetry of PCDs preserves confinement of the inner pixels even in the case of a net outward flow rate (Figure 6.2d-f). In other words, reagents streamed are locally confined in a globally unconfined flow. The main advantage of this operation mode is that PCDs no longer have to be used on an immersed surface. They can be used on dry surfaces, and also operated in an upside-down, fountain-like configuration. By injecting a neutral solution in the edge pixels, localized treatments of initially dry surfaces can thus be achieved (Appendix A, Fig. S4). Another advantage of PCDs is that they are modular and can be made of any size. The pressure drop inside pixels is decoupled from the size of the system. Furthermore, the larger the system is, the more ideal the periodicity conditions on the inner pixels become. We fabricated PCDs comprising up to 144-pixel (313 apertures) and found that they provide very stable and regular flow patterns (Figure 6.2g, h).

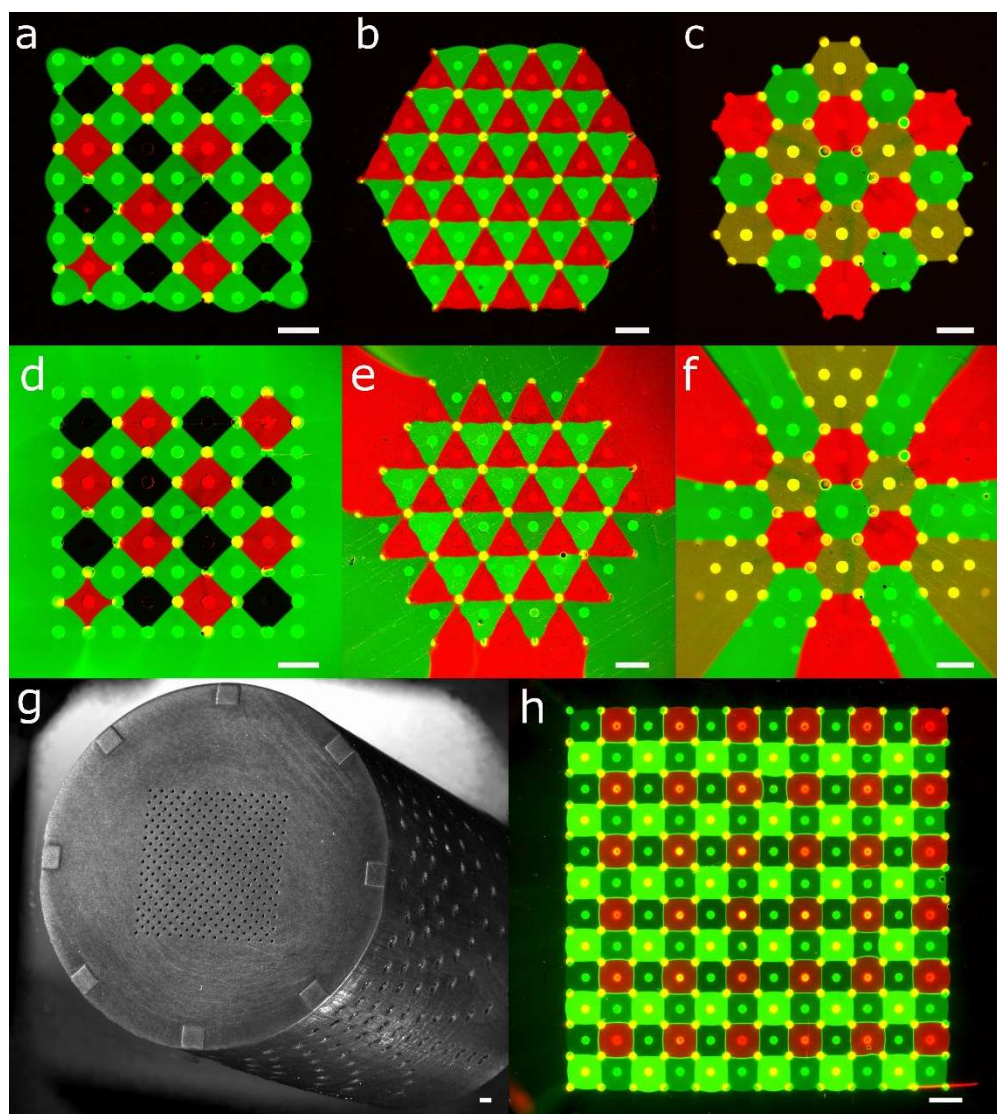


Figure 6.2 Experimental PCDs. Fluorescent micrograph at the tip of a) a square-pixel PCD, b) a triangle-pixel PCD, and c) a hexagonal-pixel PCD. Fluorescent micrographs of a locally-confined, globally unconfined d) square-pixel PCD, e) triangle-pixel PCD, and f) hexagonal-pixel PCD. g) Micrograph of a 3D-printed 144-pixel PCD device. h) Fluorescent micrograph of a 144-pixel PCD. All the scale bars represent 1 mm.

6.5.3 Display stability

PCD stability is crucial for device operation and was further investigated theoretically and experimentally. To ensure that PCD function is not compromised by a small number of clogged apertures, we compared transport inside a perfect PCD with that of a PCD with a single clogged

injection. Both experimental results and numerical simulations showed that a clogged injection has only a small local effect on PCD operation (Figure 6.3). Globally, microfluidic pixels are slightly shifted toward the errors with an amplitude decreasing quickly following a steep power law, such that even neighboring pixels are only mildly affected (Figure 6.3a-c). This error magnitude decreasing following a power law was found throughout this project (although the exact power law parameters varying depending on the PCD). These results are also in accordance with our experimental observations (Figure 6.3d-e). This situation is again analogous in LCDs, where a “dead” pixel does not affect significantly its neighbors. We obtained similar results for clogged aspiration (Appendix E, Fig. S5).

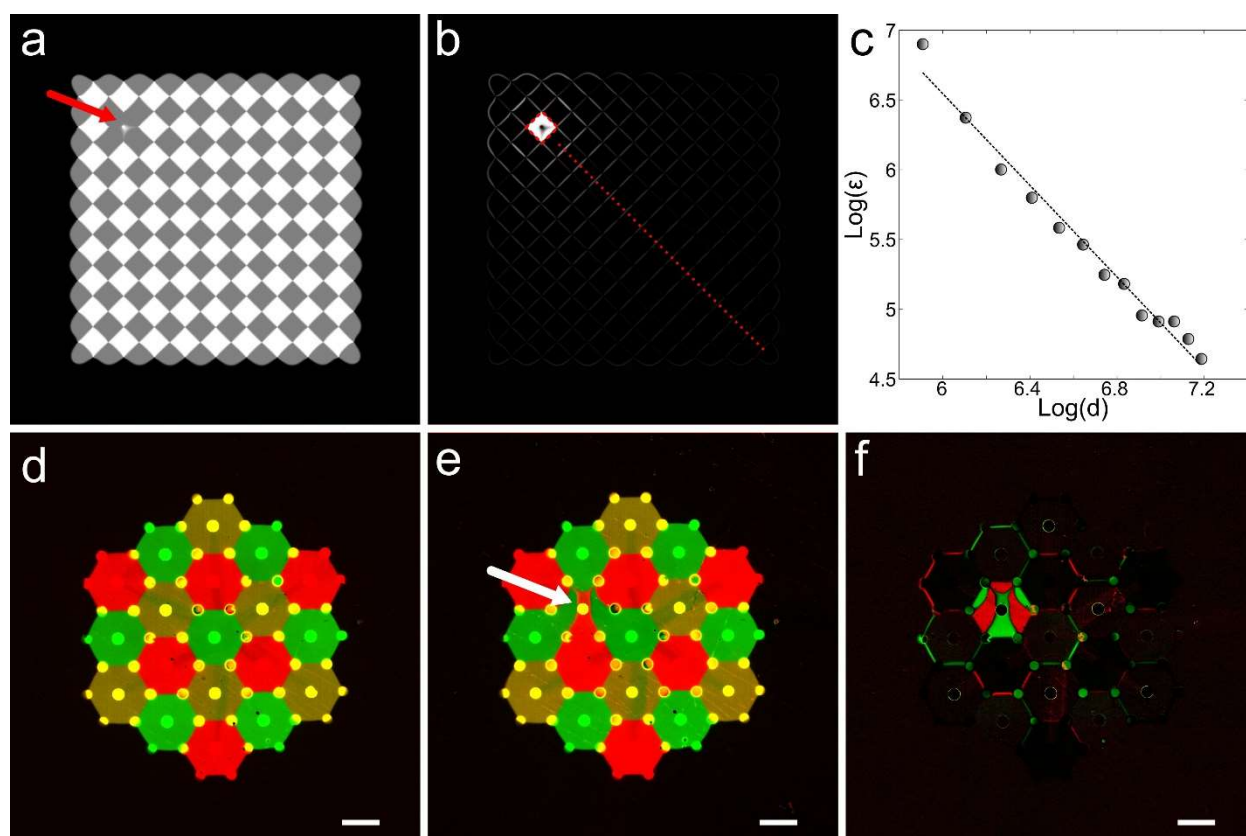


Figure 6.3 Effect of clogged apertures. (a) Simulation of a 19x19 square-pixel PCD with a clogged aperture. The clogged aperture is pointed by the red arrow. (b) Absolute error resulting from the clogged injection. (c) Graph of the error generated at each pixel border by a clogged injection in function of the position. Error was measured on the red line from (b). The error ϵ follows a

decreasing power function of equation $\varepsilon = (1.3 \times 10^7)d^{-1.64}$, where “d” is the distance in pixel. The error (ε) is the integral of errors peak intensity over position. (d) Fluorescent micrograph of a hexagon-pixel PCD. (e) The hexagon-pixel PCD from (d) with an injection turned off. (f) Absolute errors resulting from the injection turned off. Scale bars from (d-f) equal 1 mm.

Next, we investigated the stability of the resulting chemical images projected in the presence of pressure or flow rate mismatches in the display. A classical problem in microfluidics is that flow rate (Q) in a split junction is greatly affected by a slight error on the channel hydraulic radius r ($Q \propto r^4$)¹¹⁷. To examine this issue, we used a Monte-Carlo method¹¹⁸. Approximately 24 000 2D convection-diffusion finite-element transport simulations were performed, where stochastic errors were randomly added to the flow rate of each aperture. By varying the bound of the stochastic errors (from [-5%, 5%] to [-75%, 75%]), the effect on PCDs' stability was observed. The results show that flow rate or pressure errors of up to $\pm 20\%$ have virtually no effect on the PCDs (see Appendix E, section 3). Depending on the acceptable pixel deformation threshold for a given application, PCD with flow rate matching errors of up to 40% could be used. Moreover, the PCDs' size (in number of pixels) has no significant effects on its stability or error propagation, as expected from a device based on periodicity (Appendix E, Fig. S10). To conclude, while in most systems a higher number of subcomponents lead to more instability, we emphasize here that, in the case of the PCD, the use of periodic streaming flow patterns interacting with each other leads to a stable, self-correcting behavior.

6.5.4 Display reconfigurability

In turn, this pattern stability indicates that smooth transitions between multiple flow patterns exist and should be readily achievable, suggesting the possibility to stream sequences of chemicals within any given pixel. In the LCD analogy, this is equivalent to enabling a “RGB” like transition in pixels to stream chemical movies onto a processed surface. To demonstrate PCD reconfigurability with a minimum number of pumps and valves, we developed an approach strongly inspired by hardwired relay logic¹¹⁹. The apertures injecting the same chemical sequence were grouped into manifolds. We positioned programmable 3-way valves upstream of manifolds, so that every chemical image required during an experiment could be formed using a combination of logic operations on the valves (injecting either green fluorophore or red fluorophore) (Figure

6.4). An array of nine programmable syringe pumps, synchronized with nine valves, controlled the injected fluids, allowing the generation of sequences of chemical images. Each 3-way valve is adding 2 different states to the system, which when combined together result in a system allowing the generation of 512 chemical images, including the letters “P”, “O”, “L” and “Y” (Figure 6.4). Video S1 further presents the dynamic change from a chemical image to another. The transition time between different chemical images was in the order of a few tens of seconds (Appendix E, SI section 4). Moreover, the transition time being mainly due to Taylor-Aris dispersion in the tubing, it could be reduced by an order of magnitude or more using smaller tubing or capillaries (Appendix E, section 4).

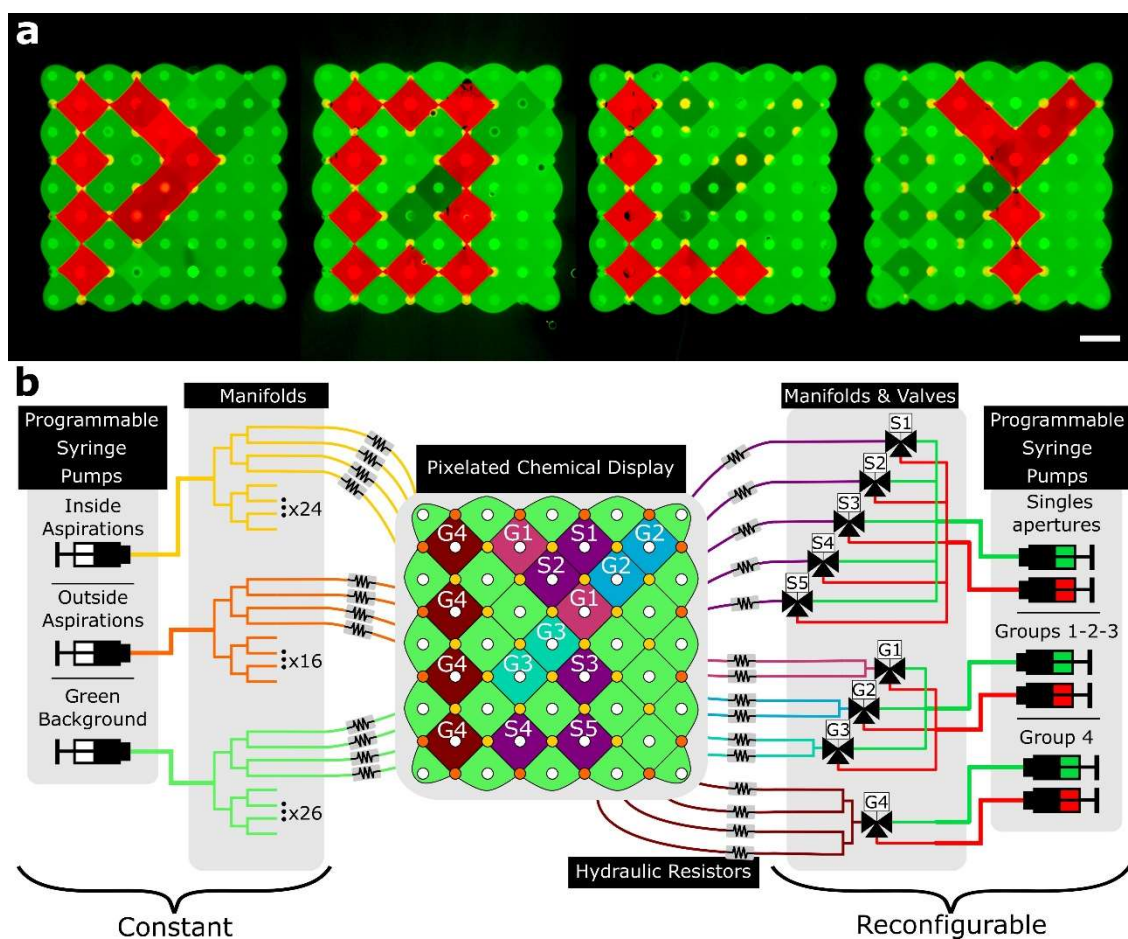


Figure 6.4 PCD reconfiguration. a) Fluorescence micrographs of PCD reconfigured to sequentially write “P”, “O”, “L”, and “Y”. Scale bar represents 1 mm. b) Schematic of the pumps, valves and manifolds used to perform the PCD reconfiguration from a).

6.5.5 Roll-to-Roll applications

Large reconfigurable, stable PCDs open up new possibilities for industrial and fabrication applications. Operating in local confinement in a globally unconfined flow removes the limitation of working in an immersed environment like with previous open-space microfluidics devices. To showcase applications on dry surfaces, we processed thin plastic films in a roll-to-roll setup using the PCD. Two distinct processes were implemented. First, as an example of surface biopatterning, we used the PCD to coat a polystyrene (PS) film simultaneously with two distinct fluorescently labeled forms of bovine serum albumin (BSA-Alexa Fluor 488 and BSA-Alexa Fluor 555). We used an 81-aperture square pixel PCD with fluid pattern similar to Figure 6.2d in a custom roll-to-roll setup to pattern the film in a stop and go manner with a cycle of 3 minutes (Figure 6.5a and Appendix E, Fig. S6). Results show well-defined, sharp patterns without overlap between the two proteins (Figure 6.5b). Consecutive patterns could be printed as close as 2.3 mm with the current 3D printed device. Remarkably, the roll-to-roll system integrated with a PCD was found to be insensitive on the gap and small angles between the PCD and the film. This resilience is due to the force equilibrium between the tension in the plastic film and the hydrodynamic pressure generated by the injections of fluids in the narrow gap¹²⁰. We implemented a second roll-to-roll process to print pure silver patterns on a different material: polyethylene terephthalate (PET). For the latter, the objective was to use the thin diffusion layer between reagents in neighboring pixels to generate a controlled interfacial reaction (Figure 6.5c). To achieve this result, we used Tollen's silver mirror reaction, a method that already demonstrated its potential for the deposition of silver thin films of controlled thickness for electric circuitry^{121,122}. Tollen's Reagent, when mixed with an aldehyde (in this case dextrose), yields solid silver. This reaction result in thin lines of silver being patterned on the PET sheet between pixels injecting Tollen's reagent and aldehyde. Water was injected around pixels where no silver line had to be patterned. To increase the silver deposition speed, a sensitization bath of tin chloride was added prior to the silver deposition¹²². As for protein biopatterning, the process was performed in a stop-and-go manner. The PET film was sensitized in a bath, rolled to the PCD, and then patterned for four minutes and rinsed for a minute while the next surface to be patterned was being sensitized. An example of complex thin film silver patterns (an E-shaped pattern) on PET is demonstrated as an example of controlled interfacial reaction in a PCD (Figure 6.5d).

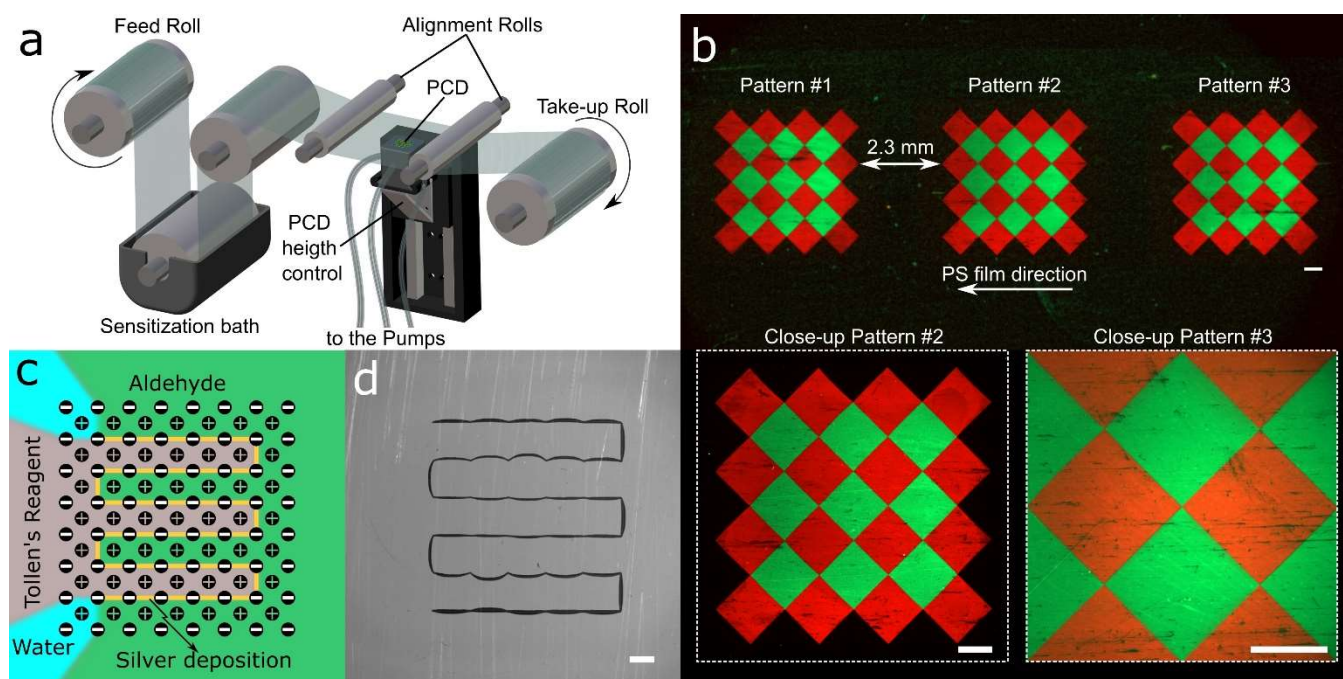


Figure 6.5 Roll-to-roll processes using a PCD. a) Schematic of the roll-to-roll setup used for the biopatterning of proteins and silver thin film deposition. For the bio-patterning, the sensitization bath was removed, and the film went directly from the feed roll to the alignment rolls b) Fluorescent micrograph of three consecutive patterns of BSA-Alexa 555 and BSA-Alexa 488 proteins on a polystyrene film in a roll-to-roll process. c) Fluids schematic of the deposition process of a E-shape silver pattern on a PET film. d) Micrograph of an E-shape silver pattern on a PET film roll. All scale bars represent 500 μm .

6.6 Conclusion

Pixelated chemical displays offer the first open-space microfluidic solution to process surfaces not immersed in fluids, opening up applications in roll-to-roll printing and thin film technologies. We demonstrated that the chemical patterns generated by the PCDs can be quickly reconfigured, impervious to evaporation, and are compatible with viscous samples. Moreover, they have no moving parts, which simplifies interfacing with any equipment or experiments requiring live imaging. Emerging 3D printing materials, such as chemically resistant polymers¹²³ or even glass⁷⁹ should allow their compatibility with a wide range of solvents or acids. As presented in this article, PCDs were used for the maskless biopatterning of surfaces and for the deposition of precise silver

pattern on thin plastic film. However, they might also find uses in bioassays by allowing the dynamic and multiplexed microperfusion of cell cultures or tissues.

In this article, we produced and operated a PCD of up to 144 pixels (12 x 12) and a reconfigurable system encompassing nine valves, thus allowing the generation of 512 different chemical images. From there, the scaling up of the device to an arbitrary number of pixels is straightforward, since all pixels operate independently from each other and displayed robustness to experimental imperfections. The number of inlets and outlets in a PCD scale linearly with the number of pixels. At least one valve per pixel would also be required to enable independent switching in every pixel as in LCD technology. This is out of consideration using macroscopic switch valves such as those used in this paper. However, recent advances in high resolution 3D printing seem to offer a way forward. Using custom resin and printers, Gong & al. recently showed the possibility to print compact arrays of up to 6 pressure valves per mm², high-density chip interconnects and channels with a diameter of 20 μm⁸³ (tenfold smaller than in this article). Using a 3D printer with such resolution could easily reduce the minimum size of microfluidic pixels to around 100 μm and increase pixel density by a factor of 100. Miniature PCDs with integrated valves and manifold systems would greatly cut channel dead volumes and simultaneously, the switching speeds of reagents within pixels. Fueled by the fast developments in 3D printing technologies, PCDs with pixel numbers in the thousands similar in size and resolution to early LCD screens¹²⁴ may not be too far away.

6.7 Materials and Methods

6.7.1 PCDs fabrication and operation

PCDs were designed using Catia V5 (Dassault Systèmes). They were printed using a stereolithography 3D printer with a x-y resolution of 27 μm and a wavelength of 385 nm (Pico 2 HD, Asiga). The resin used was Pro3dure GR-1 black (Pro3dure GmbH), printed in layers of 50 μm, with an exposure time of 0.468 s. After the printing, PCDs were cleaned in an isopropanol bath in a sonicator. They were then post-cured 10 min in UV light (Flash UV Curing Chamber, Asiga). 1/32" tubes (Masterflex Tygon, Cole-Parmer) were plugged and glued using a UV-sensitive resin (DecorRom). Manifolds were fabricated using the same method. Different

experimental setups were used for the figure of this article, in an upright and downright configuration. In some case, PCDs were simply set down on the glass slide, in others, spring or screws were used to hold the PCD in place. The sample distance to the PCD was controlled by the spacer pillars. Flow rates were controlled using nemesys syringe pumps (Cetoni GmbH). For the reconfigurable display, Cetoni 3-way valves were used. Pumps and valves were controlled using a custom LabView code (National Instrument).

6.7.2 Experimental measurements

Fluorescent micrographs were taken using an inverted fluorescence microscope (Axio Observer.Z1, Zeiss) with a Lavision sCMOS camera (Lavision), and an upright microscope (Axio Zoom.v16, Zeiss) with a sCMOS camera (Pco.Edge, PCO). Fluorescein salt dissolved in ultrapure water was used as the green fluorophore and propidium iodide (Sigma Aldrich) and DNA sodium salt (DNA sodium salt from salmon testes, Sigma Aldrich) dissolved in ultrapure water was used as the red fluorophore. A background image, which was taken by tuning off the PCD's injections, was subtracted from the measured images to remove the background noise. This process was made using MATLAB. The reconfiguration video was made using the same protocol frame-by-frame before being compressed using MATLAB.

6.7.3 Simulations

2D finite element simulation of the PCDs were made using the MATLAB-COMSOL livelink (COMSOL Multiphysics v.5.1, COMSOL AB). Simulations were made by coupling Laplace's equation (velocity potential) with diffusion. Dimensions and flow rates used were in the same order of magnitude as what was used for the experiments. Fluorescein was considered as the diffusive species and the diffusion coefficients used was $0.5 \times 10^{-9} \text{ m}^2/\text{s}$. Pixels with concentration of 1 and 0.5 were simulated to allow the easy segmentation of the pixels. To measure the effect of a clogged injection on a PCD, a 19×19 aperture square-pixel PCD with an injection turned off was simulated and compared with a perfectly working PCD. The error measured (ϵ) was the integral of errors peak intensity over position at each pixel transition.

6.7.4 Stability Analysis

A MATLAB code was used to automatize simulations with randomized errors on the flow rate on every aperture (each injection having flow rate randomized in the range $[Q - (\text{limit}(\%) \times Q), Q + (\text{limit}(\%) \times Q)]$). After the simulation, the pixels were segmented using a level threshold. Morphological mathematical image opening (erosion followed by dilatation) was used to improve the segmenting of the microfluidic pixels. For each microfluidic pixel, the area was measured, and the usability threshold criteria was tested. The standard deviation of the pixels' areas and usability threshold were calculated for every simulation and were then averaged over a thousand simulations for each condition. The standard error was calculated over the 1000 simulations. 95% bilateral confidence intervals on the standard deviation of the area and the ratio of pixels respecting the usability threshold were calculated using $\pm 1.96 \times (\text{Standard Error})$. The analysis didn't consider the border pixels of the PCD since they don't have the same geometry as the other pixels. Also, in a small number of cases, for simulation with high flow rate errors ($\geq 50\%$), our algorithm couldn't properly segment clusters of two to three microfluidic pixels. In this case, the area considered for each pixel was the combined area divided by the number of pixels. In the rare case where more pixels were wrongly segmented as one, their value was simply rejected. For each simulation, the segmented microfluidic pixel image was compared to a segmented image of PCD without error on the flow rate and an error map was made. By calculating the proportion of error maps containing an error for each point, the probability of error heatmaps were generated. More details in Supplementary Section 3.

6.7.5 Roll-to-roll experiment

A custom roll-to-roll setup was built for 8 cm width film. The setup comprised a motorized stage (X-LRM, Zaber) to control the gap in between PCD and the plastic film. The stage was controlled using a custom LabView code. A 190 μm thick polystyrene (PS) film (Goodfellow) was patterned using 10 $\mu\text{g}/\text{ml}$ BSA-Alexa Fluor 555 and BSA-Alexa Fluor 488 (Thermo Fisher Scientific) in a solution of 25 mM acetate buffer (Thermo Fischer) at pH 5, chosen to equal the proteins' isoelectric point to improve adsorption on the PS. The film surface was patterned for two minutes at a flow rate of 800 nL/s per aperture. The surface was then rinsed for one minute by stopping the BSA injection. Acetate buffer was injected by the outside injection while rolling the roll to ensure that a

film of liquid was always present between the PCD and the film, and thus that no air would be aspirated.

The silver circuit patterning was performed on a 250 μm polyethylene terephthalate (PET) film (McMaster-Carr). The film was sensitized in a bath of 50 mM tin chloride (Sigma Aldrich) for 5 minutes. The tin chloride solution was made by mixing the tin chloride to ultrapure water, and then drops of 1 M HCL (Sigma Aldrich) were added until the dissolution of the tin salt. The patterning was performed by injecting 50 mM Tollen's reagent by a set of apertures, and 50 mM dextrose (Sigma Aldrich) by another set of apertures. Tollen's reagent was made by mixing a 100 mM silver nitrate (Sigma Aldrich) solution in deionized water. 100 mM KOH solution (Sigma Aldrich) was added at a 1:1 ratio. 30% ammonia (Sigma Aldrich) was then added dropwise until the precipitate dissolve¹²². The PET film was patterned for 4 minutes with a flow rate of 800 nL/s per aperture. The film was then rinsed for a minute by stopping the dextrose and Tollen's reagent injection while keeping the deionized water injection and central aspirations running.

6.8 Data Availability

The data associated with the stability analysis are available at the following data repository: <https://doi.org/10.5683/SP2/TFJPJM>. All other data are contained in this article and its supplementary information files (see appendix E).

6.9 Acknowledgments

P.A.G. and E.B. acknowledge a graduate scholarship from the Fond de Recherche du Québec Nature et Technologies (FRQNT) and from the Natural Sciences and Engineering Research Council (NSERC). M.T. acknowledges an undergraduate internship scholarship from the NSERC. T.G. acknowledges support from NSERC (RGPIN-06409) and FRQNT (#205993, #197507) grants. We acknowledge CMC Microsystems for the shared access to design and simulation tools. We acknowledge David Juncker, Klavs F. Jensen, Molly M. Stevens, Stéphane Kena-Cohen and Daniel Therriault for useful discussions on the manuscript.

CHAPTER 7 PRESSURE-BASED PCD

This chapter covers my most recent contribution to the design and operation of PCD, that is, the creation of PCD operable using pressure pumps. The whole idea of this chapter is to demonstrate that it is possible to operate any PCD (of theoretically any size), with only two pressure pumps. While it was known from the start that it would be feasible, I believe it is an essential part to the design and fabrication of economically viable massively parallel systems. This chapter will describe the advantages and reason behind the creation of pressure-based PCD. PCD design modifications and results will then be presented. The work in this chapter has not yet been published, but it seems obvious to me that any future PCD papers from our research group will be based on pressure operated PCD.

7.1 Comparison between syringe pumps and pressure pumps

Both the design of reconfigurable MFMs and PCDs were made using syringe pumps. Other than being the equipment that was available, syringe pumps are extremely precise and helped to simplify small MFM circuitry. Since the flow rate is directly controlled, there is no need for hydraulic resistance calculation and matching. Moreover, as we designed the MFMs, we were interested in comparing experimental results with our analytical model. Syringe pumps excellent precision have been of great help for that. The Cetoni syringe pump we used also had integrated valves, which simplified the experimental setup during PCD reconfiguration experiments.

However, syringe pumps bring a lot of problems. They have a minimum flow rate (without pulsations) that is far higher than what can be achieved with pressure pumps, especially since it is possible to increase hydraulic resistance of the fluidic circuits when working with pressure pumps to achieve lower flow rate. Moreover, syringes are slow to fill and connecting them to the fluidic circuit is a step prone to bubble generation. Syringe pumps are also limited by maximum size of the syringe that can be used. Since the biggest compatible syringes have a volume of 20 ml, this limits the maximum time scale of an experiment. Pressurized vessels, on the other hand, can be as small as few microliters to liters in volume. As the system became more complicated and incorporated more apertures, fluid manifold design and resistance matching were required. It took

away the advantages of syringe pumps (since the design of fluid circuits including hydraulic resistors are essential in both cases).

The killing blow for the syringe pumps, however, comes from their inability to pump multiple fluids. A PCD or multipole requiring the use of 10 reagents during an experiment requires a system with at least 11 pumps (10 for the injection and 1 for the aspiration). At around five thousand dollars each, a system using syringe pumps cost tens of thousands of dollars only in pumps. This cost would be an important deterrent to reconfigurable MFMs and PCDs. On an experimental point of view, the use of tens of syringe pumps also leads to cluttering. Pumps have to be put farther and farther away from the system (which leads to its own kind of problems), and the PCD system becomes more and more difficult to integrate with other systems such as microscopes or incubators. It also becomes more and more difficult for the user to make sense of the experimental system.

Pressure pumps, on the other hand, can be used to pressurize multiple vessels, and thus to pump multiple fluids in parallel. Pressure pumps allow the fabrication of PCD using only two pumps, one used for the aspirations, and the other used to pressurize all the injected reagents. Using pressure pumps, it is possible to fabricate a highly multiplexed PCD system for less than ten thousand dollars. Using only two pressure pumps save a lot of space, and they can be positioned far away from the system without problems, as long as the pressurized vessels remain close to the system. The only major disadvantage that comes from the use of pressure pumps for PCD is that the fluidic circuit requires more attention to make sure that the hydraulic resistance of every aperture is matched. This is a crucial aspect as the hydraulic resistance scales with the fourth power of the channel radius ($\sim R^4$), which means that a 2% error on radius will induce a $\sim 8\%$ error on the resulting flow rate at a given pressure. With many resistors in parallel, these discrepancies are further multiplied.

Table 7-1 Comparison between system operated with syringe pumps and pressure pumps

Type of pumps	Syringe pumps	Pressure pumps
Flow rate :	Precisely control the flow rate	Control the pressure, flow rate is estimated from $P=R_{\text{hydraulic}}*Q$
Bubble trouble	Increased risk of bubbles (syringes filling and connection)	Low risk of bubbles
Reservoir size	μl to 50 ml	μl to liters
Fluidic circuit	Simple if no manifold are necessary	Resistance must be matched between every aperture
Parallelizable	One reagent per pump	PCD only requires 2 pumps
Cost	Expensive (scale with the number of reagents used)	Low (fixed number of pumps required)
Space required	Large (cluttering problems)	Medium

7.2 Pressure-based PCD design

Pressure-based PCDs use the same PCD chip as their syringe pump counterparts presented in the last chapter. Moreover, aspirations are connected using a manifold or a series of manifold, like in previous version. Every injection injecting the same reagent is grouped through a manifold and connected to the appropriate pressure vessel. The main difference with previous large-scale PCDs is that the hydraulic resistance between injection groups must be matched. When using syringe pumps, matching had to be done only between injection sharing a common manifold. Here, any modification to an injection fluid line will affect the whole system. An easy work around that problem is to create PCDs where all the injection groups have the same number of pixels (for example 4 groups of 3 pixels like in Figure 7.1). If the same tubing and manifold are used, the flow

rate should be matched between the apertures. As previously, the use of small capillaries (250 μm) for the fluidic circuit and manifold connection assures that most of the resistance comes from this part of the circuit. Connection tubes can be seen as precision hydraulic resistors that match the flow rate. It allows the neglect of any variance in hydraulic resistance coming from the PCD chip. While injection groups with equal numbers of pixels are favorable, the matching of groups with different numbers of pixels can theoretically be done using a simple resistor circuit model and matching the resistance. Again, the hydraulic resistance from the chip is negligible, and thus only the tubes between the pressurized vessels and the manifold, and between the manifold and the PCD itself must be considered.

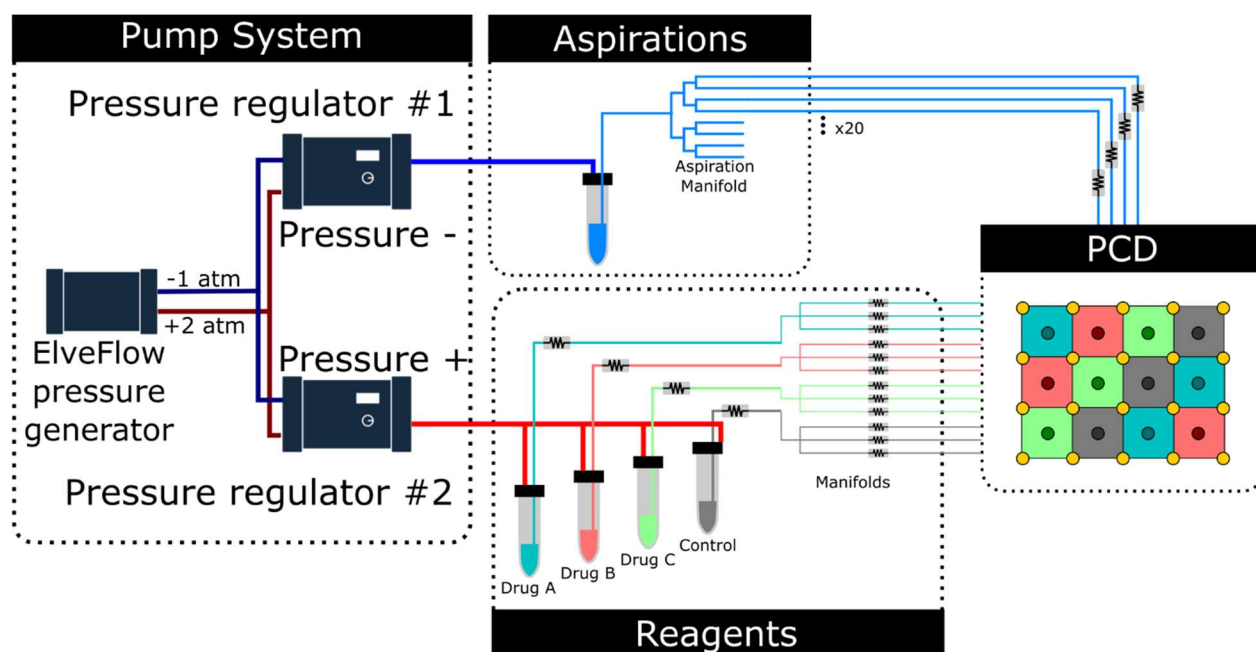


Figure 7.1 Pressure-based PCD. Fluidic circuit schematic of a 12-pixel (4 groups) pressure-based PCD operating with two pressure regulators. The pump system is based on a pressure generator that feeds the inlet pressure of the two-pressure regulator. The aspirations are all connected together through a manifold. Four reagent vessels are connected to a single pressure regulator. Both for the aspirations and the injections, the tubes in between the pressurized flask and the PCD serve as precision hydraulic resistors to match the flow rate.

Pressure-based PCDs fabricated during my project used Elveflow pumps. The pump system was made using a pressure generator and two pressure regulators, one controlling the aspirations, and

the other controlling the injections. Even though microfluidic pressure pumps are sold as pumps, they generally are pressure regulators. The pressure generator fed a 2 atm and -1 atm pressure line to the regulators that then precisely control the pressure output in the range [-700 mBar, 700 mBar] in a line (Figure 7.1). Pressure regulator control was achieved using a custom-made python user interface.

Choosing the value of the hydraulic resistance of the circuit is a compromise in between different factors. Of course, the tube used must be long enough to connect the system, but not too long to become a cluttering problem. The range of the flow rate at which the system will operate must match the range of pressure that the pumps can provide. Someone might think that using the highest possible resistance that can match with the pressure pump range would be optimal, since that would limit the effect of pumps fluctuations. However, this idea neglects the effect of pressure gradients on bubble generation. The higher the pressure gradient between the pressurized flask and the PCD apertures is, the more the fluid at the tip of the PCD will be oversaturated in gas, as it can be understood from Henry's law¹²⁵. Risk of bubble nucleation increase with the oversaturation level. Since bubbles are a far more problematic than a small flow rate mismatch (PCDs can resist up to 20% deviation on flow rates with virtually no effect, as demonstrated in chapter 6), it is more advisable to build PCD with relatively low hydraulic resistance. PCD systems built in this project had group hydraulic resistance in the range of 10^{-12} to 10^{-11} Pa·s/m³. They were designed to operate at their normal flow rate (~ 500 nL/s·aperture) at approximately 100 mBar.

7.3 Results & discussion

9-pixel and 12-pixel PCD were fabricated and tested. Fluorescent micrographs present result similar to what was obtained using syringe pumps (Figure 7.2). Pressure-based PCD could be operated flow rates as low as 100 nL/s. Pressure-based PCDs were tested for 1 hour periods without problem or bubble nucleation.

Most differences with syringe pumps are qualitative and are related to increased simplicity. Pressure-based PCDs have proven themselves to be far more user-friendly. Filling pressurized vessels takes a fraction of the time required to load syringes. Moreover, starting the system is also simpler. Rinsing the system with ethanol before loading the reagents have proven effective to avoid

bubble nucleation. Doing the same protocol with syringes sometimes injected bubbles in the system when changing from an ethanol syringe to a reagent syringe, which is problematic.

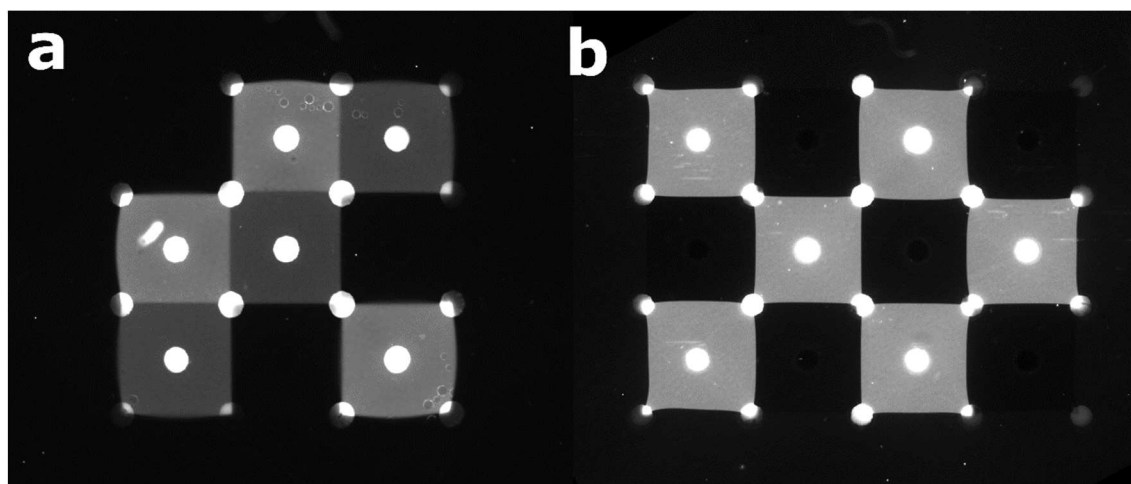


Figure 7.2 Fluorescent micrograph of pressure-based PCD. A) A 9-pixel PCD (3 groups of 3 pixels). B) A 12-pixel PCD. This PCD is organized as 4 groups of 3 pixels and uses the manifolds presented in Figure 7.1.

Using pressure pumps to replace syringe pumps would allow the generation of large-scale PCD, while using a fraction of the cost and equipment that would otherwise be required. Moreover, a generic pump system can be designed and fabricated, and then used for small and large PCDs alike. Moreover, modification to the PCDs or the experiments doesn't require the redesign and modification of the pumps system. Considering the obvious advantages of using pressure pump to operate PCDs, it seems clear that most future PCDs will use such pump systems. Decreasing the cost and complexity of PCD systems might contribute to their adoption in life sciences.

CHAPTER 8 GENERAL DISCUSSION

This thesis main objective was to design, fabricate and evaluate reconfigurable and multiplexable open-space microfluidic systems. This objective led, in the image of the device itself, to a tentacular project with many interconnected subprojects. This chapter will discuss the main results of every chapter and article in relation to the project objective and sub-objectives. In a second time, this chapter presents the limitations of this thesis work, and my recommendations to overcome or circumvent them.

8.1 Discussion on project objectives and results

8.1.1 Multipolar microfluidic system fabrication

The first objective of this thesis work was to develop a fabrication method for MFMs. It was achieved using stereolithography 3D printing as presented in chapter 4. MFMs were designed using Catia as a CAD software, either by direct drawing for simple microfluidic multipole, or by using script-based CAD for complex designs. They were then printed with an Asiga Pico 2 3D printer and then cleaned with isopropanol in a sonicator bath. After post printing UV exposition, MFMs were assembled by gluing the tube in place. For PCDs, custom 3D printed manifolds were used in the system assembly.

This method has proven effective and was used throughout the project. MFMs comprised of up to 313 apertures were fabricated. They could be printed with apertures as small as 160 μm and internal channel of 300 μm . While this resolution doesn't allow the fabrication of MFMs targeted at single cell processing, it is sufficient to fabricate MFMs with confinement patterns in the millimetric scale. This resolution is adequate for most reconfigurable MFM applications we considered. Reconfigurable MFMs are designed to address clusters of cells and to pattern surface areas in parallel rather than to offer an extremely precise fluid confinement area. However, the low resolution of the printing has an important consequence. It prevents the use of manifold directly integrated into the system, which complicates the assembly of large-scale MFMs. It is, in my opinion, the biggest limitation of my work and it will be discussed further in the project's limitations.

The fabrication process I developed has a fast turn-around, as most systems can be designed and fabricated in less than a day's work. Moreover, the positioning of the apertures has no effect on the fabrication protocol. The versatility was extremely useful as it allows the testing and evaluation of different “families” of multipole without having to overthink the fabrication protocol. The method was tested on dipoles, and then extended to work with quadrupoles, radially symmetrical multipoles, staggered and rectangular arrays, and eventually PCDs.

I believe the fabrication process for MFMs I developed in this project shine when compared to other methods that existed at the start of my thesis, as shown in Table 8-1. It is not that 3D printing is a better or worst method to build microfluidic probes, but that the combination of versatility, short turnaround time and low cost fitted the requirements of this project. It also allows the fabrication of systems that would be almost impossible to build by relying on microfabrication processes.

Table 8-1 Comparison between MFM fabrication methods. The most limiting characteristics of each method are highlighted in red.

	PMDS-Silicon ¹³	Silicon laminating ⁵⁶	3D Printing
Minimum aperture diameter	20 μm	1 μm	160 μm
System robustness	Fragile, prone to leakage	robust	robust
MFM geometry limitation	Not limited	Apertures must be positioned on 1 or 2 planes	Not limited
Turnaround time	Slow	Slow	Fast (1 day)
Throughput	Low	High (batch process)	Low
Cost	\$\$\$	\$\$\$	\$

3D printed microfluidic multipoles flow fields showed no important deformation that would have been a sign of important surface deformations. They were evaluated using fluorescence microscopy

measurement to capture the concentration profile and PIV to measure the flow velocity. Experimental results were benchmarked against 2D and 3D simulations, and my colleague Étienne Boulais convection-diffusion analytical model. A good fit was found.

3D printing is becoming more and more accessible, and relatively affordable. Using the fabrication method, I developed, non-specialists should be able to fabricate and operate simple systems.

8.1.2 Small Size reconfigurable multipoles

The second objective of this thesis project was to design, test, and characterize multiplexed open-space systems with a limited number of apertures (<12 apertures). It was achieved by experimenting with reconfigurable multipole, as presented in chapter 5 and the article “Microfluidic multipoles theory and applications” on which I am co-first author.

The first part of this work was an exploratory phase. Geometry of MFM with reconfiguration and multiplexing potential had to be determined. The theory of tracer dispersion in arrays of openings within a 2D flow cell had to be developed. Multiple MFM geometries were tested, and my devices played a key role in validating the theoretical models from my colleagues^{93,126}. Data from this exploratory phase also served to validate my colleague convection-diffusion model. Some geometries of MFMs were found to have a high potential to create reconfigurable MFMs, namely the “flower” or rotationally symmetric multipole, and the translationally symmetric multipoles (tMFMs) based on arrays of apertures.

Chapter 5, presented the first implementation of reconfigurable MFMs. It is a change of paradigm from previously presented work that all relied on scanning system. Three demonstrations of reconfigurable MFMs were presented in this work. The first demonstration was based on the pulsing of an rMFM “petals”, which resulted in a chemical stroboscope. We demonstrated that this system could be used to pulse chemicals on confined areas with various pulse frequency and duty cycle, with a temporal resolution in the order of the second. We envision this device in the study of cellular pathway dynamics. There is a growing interest in the study of cell dynamics¹⁰⁶, however, apart from optogenetics, few methods provide the dynamics required. MFMs allow for the cell medium to be changed in the order of seconds due to their constant streaming. I believe that while the chemical stroboscope doesn’t offer the parallelization of other devices design during this

research project, it remains one with the most potential. Chemical stroboscopes are fairly simple to use, and they offer a temporal resolution matched by few, if any, liquid handling systems in life science. The use of a chemical stroboscope to study cellular pathway dynamics is currently being studied by my colleague Pierre Clapperton-Richard in collaboration with Prof. Laurent Potvin-Trottier. Future results will give more insight on the potential of reconfigurable multipoles in this field.

The second reconfigurable MFM presented based on a tMFM were injections and aspirations were rapidly turned on and off to generate sequence of chemical images on a surface. The main goal of this experiment was to demonstrate the high reconfigurability potential of MFMs. The theoretical number of chemical images that could be produced scale with 2^a , where “a” was the number of apertures. This represented 4096 chemical images for a 12-aperture tMFM. The reconfiguration of the tMFM in 28 patterns during a single experiment was demonstrated experimentally.

The third reconfigurable MFM demonstrated, and the pinnacle of this part of my research was the automation of an immunofluorescent assay using a staggered 12-aperture tMFM. Three overlapping chemical patterns were used to perform the assay on a glass slide coated with antibodies. A binding curve of an antigen was generated, and a limit of detection of 13 pM/ml was found. It corresponds to state-of-the-art limit of detection. The assay was only a proof of concept and was limited to the testing of 6 different concentrations of antigen. Moreover, the volume of analyte and reagent required remain high at around 360 μ L per condition (when considering a 1h incubation time at 100 nL/s), which is around 3.5 time the volume required for an immunoassay in a 96 well plate¹²⁷. However, it is the first implementation of a multistep experiment performed with an open-space microfluidics, and a lot of optimizations could be performed. It is also of notice that it is the first demonstration of an experiment requiring long incubation times (minutes to hours) using an MFM. This proof of concept is, in my opinion, one of the major contributions of my thesis. MFMs were previously limited to single step experiment such as cell staining or localized cell lysis. This experiment showcases the possibility to use MFMs to automatize long multistep experiments, which opens a lot of possibilities.

A main critique that can be addressed to this work remains the low parallelization potential of the multipoles. Moreover, in light of my whole research project and the design of PCDs, it seems obvious to me that the future of reconfigurable MFMs will be based on the switching of the injected

reagent rather than the creation of overlapping patterns as used in this chapter (except in some case for which a fast dynamic is of utmost importance). However, the small reconfigurable MFMs remain an important contribution to my work. The objective behind the design of these devices was to challenge the paradigm that MFMs had to be scanned and used in a serial way. Moreover, these systems enabled me to demonstrate the use of MFMs to automate long and multistep experiments. They showed the possibility to create multiplexable and reconfigurable open-space systems, which opened the way to new applications, such as experiment automation or the study of cell dynamics.

Another aspect to consider is how essential the small reconfigurable MFMs were in the design of PCDs. The combination of polygonal MFMs and tMFMs are what inspired the PCD. Moreover, the use of manifolds in my subsequent work comes from the obvious limitations of connecting each aperture to a pump as performed with small reconfigurable MFM. Even the idea of using two pressure pumps to operate complex systems originally comes from the work of this chapter, since the problems related to the use of arrays of syringe pumps became obvious at this stage of my research project.

8.1.3 Scalable multipole and large scale pixelated chemical display

The last objective, and main achievement, of my project is the design of a scalable MFM architecture we termed the pixelated chemical display. It was presented in chapter 6, which correspond to my article published in PNAS, and in chapter 7, which presents an improvement on the design.

After the work on small size reconfigurable MFMs, it was becoming increasingly clear that to achieve a high multiplexing potential, a repeatable subunit would be the key. The major result of this work is that using an MFM based on an array of apertures, the array can be separated in subunits based on the polygonal MFM geometry. This yield independent confinement areas that we called microfluidic pixels. These pixels have an independent injection but share the aspirations. As long as the architecture is respected, any number of pixels can be added to a system. Large systems allowing the creation of up to 144 pixels were tested during this work.

PCDs and the use of microfluidic pixels have some major implications. Using this architecture, systems comprised of virtually any number of pixels can be fabricated. Moreover, the pixel size, the gap and the flow rate can be modified as long as the flow remains laminar viscous. This makes PCD an extremely versatile architecture.

We demonstrated that the PCD, to the contrary of previous MFM system, could be used on dry surfaces, by using PCD that has a slightly net injection flow rate. It opens the possibility to use PCD for dry surface patterning. We demonstrated that by integrating the PCD with a roll-to-roll system and performing both protein biopatterning and silver patterning on thin plastic films.

While someone might hypothesize that a system formed of more components might be more prone to errors and less stable, we demonstrated that the opposite was true for PCDs. Using Monte Carlo inspired simulations, we demonstrated that errors of up to 20% in the matching in between apertures had not effect on the confinement patterns of the pixels. It is unheard of in other open-space streaming microfluidic devices (such as microfluidic probes), where confinement patterns are directly linked to the ratio of the flow rate between apertures. Moreover, a faulty pixel does not significantly affect the neighboring pixels. Small deformations on the surface were also found to have almost no impact on the pixels. While most of the stability analysis has been pushed in the supplementary material of my article, I believe it is an important result, as it shows that PCDs are robust system that could be used in real-life applications.

An intuition on PCD could be that they require more apertures per pixel or confinement area than a dipole or an array of dipoles. However, a square microfluidic pixel is comprised of an injection and 4 quarters of aspiration apertures, and thus, only 2 apertures. A square pixel PCD is, thereby, per confinement area, not more complicated than a dipole. Using triangle pixels, it is even possible to use 1,5 apertures per pixels. While using the same number of apertures per confinement area, PCDs offer an increased stability and scaling potential.

Just like with small size reconfigurable MFMs, we showed that it is possible to reconfigure the pixels of a PCD. However, it is more complicated in this case as valves must be used to change the reagent injected by the pixels. The transition time is limited to a few tens of seconds due to the Taylor dispersion occurring in the PCD fluidic circuit. The PCD reconfiguration dynamic is thus

much slower than the small reconfigurable MFMs. However, it remains fast enough for most life science applications. PCD could be used to automatize large-scale multistep experiments.

One of my main critics of my own work was that most of the systems I designed relied on an array of expensive syringe pumps. Therefore, in the last few months of my PhD, I decide to fabricate PCDs that can be operated with only 2 pressure pumps, as presented in chapter 7. While it was not essential to present the concept behind PCDs, I believe it is an important contribution to my work. It demonstrates that PCD could be operated with a fairly inexpensive pumping system. It also has the consequence that the pump system doesn't have to be modified depending on the experiment, and thus, a standard pump system can be fabricated. Pressure pumps are not just cost-effective. I saw a great increase in user-friendliness of the PCD system when switching from syringe pumps to pressure pumps. Since most life-science protocols are already long and complicated, having a user-friendly system with a fast setup time is of utmost importance for PCD adoption.

Predicting the future uses of PCDs remains difficult. The PCD designs presented in this thesis would allow the fabrication of devices comprised of tens of thousands of pixels, given the appropriate fabrication method. Furthermore, they could be made with various degrees of reconfiguration. Applications where PCDs could be used are various, but further application-oriented research will be required to determine for which one they would bring a significant advantage compared to current methods. The use of PCD to automate life science assays such as immunoassays and tissue staining are an obvious possibility. However, other applications can be considered. Due to their constant streaming, PCDs might be well adapted to perfuse high density surface plasmon resonance imaging systems (SPRi)¹²⁸. Due to their compatibility with wet and dry surfaces, PCDs could be used in for industrial processes and on manufacturing lines. They could be used to perform localized surface treatment, or localized surface functionalization. For example, PCDs might prove useful to coat surfaces with intricate patterns of proteins that are sensitive to shear stress, temperature change or evaporation.

PCDs differentiate from others parallelizable liquid handling solution by requiring the constant streaming of fluid, and by requiring no physical feature to create segregated fluid confinement areas. Moreover, they can achieve a certain degree of reconfiguration while requiring no moving component. Application considered for the PCDs should take advantages from those particularities.

PCDs answer the objective that was identified at the beginning of my project, which was to design a large scale and reconfigurable open-space microfluidic device. The device I presented in this thesis is, in my opinion, a mature design. PCDs are robust, versatile and scalable. Reconfiguration is possible. Moreover, we have an analytical model to predict convection diffusion under it. However, I am also aware of the limitation of my design. Much work remains to achieve a commercially viable or easily adoptable technology. The application performed with the PCD remains limited and relatively simple. Future projects that focus on more complex life-science applications will be required to fully access PCD potential. Multiple limitations to my work remain. I will address them in the next section.

8.2 Limitations and recommendations

After five years of work on multiplexed open-space systems, I have developed multiple system architectures that I believe has strong potential in the life sciences and surface processing industries. However, a lot of work remains to prove their potential in real life application. In this chapter, I want to develop on the limitations of my project, as well as on my insight concerning the future of PCDs. I also want to discuss some traps and challenges that evaded my articles and thesis chapters, and I feel anyone working on these devices will confront. I hope it will save time and help quick start future projects on PCDs, and, furthermore, reduce the risk of starting unsuccessful projects.

8.2.1 Inherent limitation of hydrodynamic flow confinement

The first limitation of the MFMs is general and can be applied to any open-space system that trades walls and channels for hydrodynamics flow confinement (HFC). Systems based on HFC are in an equilibrium. They allow the generation of confinement patterns as long as the convection remains dominant over diffusion ($Pe \gg 1$). Practically, that means that a low flow rate increases the diffusion length and diminishes the pattern sharpness. On the contrary, perfect chemical patterns can be generated in exchange for a high flow rate. Moreover, MFMs must constantly stream to maintain the fluid patterns on the surface. The consequence is that MFMs are not particularly appropriate for experiments that requires that a minute amount of reagent be kept on a surface for a long amount of time. Dropping a droplet in a well is far more effective in that case. Open-space

microfluidic might not be the appropriate solution if the main objective of a project is to reduce the consumption of reagent.

In general, if walls (from a well or a microsystem) are not a problem, or if there are no advantages to the use of an MFM, using system based on walls and channels will be easier. I believe that future research on applying MFM should focus on applications in which the MFMs have a clear advantage. Advantages can take many forms; MFMs are normally easy to integrate to existing setup, and they might allow an increase in test density. Moreover, MFMs are well suited for experiments requiring constant perfusion (like live cells and spheroids). In some cases, like for chemical stroboscope, MFMs can offer the pulsing of chemical reagent with a fast dynamics.

The reason behind the choice of using an MFM should be clear before the start of a project.

8.2.2 PCDs and MFMs are not compatible with thick tissues.

PCDs are not compatible with thick tissues slices. This limitation is a direct consequence from the previous one. Tissue permeability is extremely low which means that no convection takes place in a tissue slice. Consequently, no convection is present to balance the diffusion (the Péclet number in a tissue goes down to almost 0), which result is the chemical gradient becoming increasingly wide. Pixels can be generated on the surface of a thick tissue, but they will not be conserved inside of it. This effect becomes more and more important as the tissue thickness increases. Simulation I made toward the end of my PhD showed that working on 20 to 100 μm -thick slices might be possible depending on the parameters, but that an important contamination between pixels is inevitable in thicker slices in the order of 400 μm .

8.2.3 Fabrication method

The fabrication method developed in this project has been of tremendous help in the fast prototyping of microfluidic multipole. However, the method was developed to fabricate relatively small MFMs. As the MFMs and PCDs are becoming bigger and more complex, this method raises many other challenges. One of them is linked to the relatively low resolution of the 3D printer and the large internal channel size ($\sim 160\text{-}300\ \mu\text{m}$) that can be fabricated with it. The low reproducibility between printed channels prevents the fabrication of integrated manifolds, as the flow rate between channels would not be matched (since hydraulic resistance varies in $1/r^4$, where r in the channel

radius¹¹⁷). Consequently, channels must all be individually addressed, and an external manifold used. The assembly can take from a few hours to a few days of work (depending on if assembling 9-pixel or 144-pixel display). It is also a step prone to human errors. In my opinion, it is currently the biggest limitation of my work. The low fabrication throughput limits the application of PCDs for case in which they must be used as a single-use device (for example if working with cytotoxic drugs).

I believe that changing the fabrication method should be one of the next steps for a PCD related projects. I would recommend keeping 3D printing as a fabrication method, but I would suggest switching to a 3D printer designed for microfluidics. Nanoscribe (based on two photon polymerisation) would be an option. It has already been used to fabricate microfluidic probes for single cell analysis¹²⁹. However, this fabrication method is slow and expensive. I would rather recommend keeping the stereolithography 3D printing approach, but to use a printer with optics optimized to give a better resolution. Greg Nordin's group demonstrated the use of a 7.5 μm xy resolution printer to fabricate channels of 20 μm of diameter⁶⁹, integrated valves of around 200 μm ¹³⁰, and interconnection systems⁸³. Using a similar technology would allow the fabrication of a new generation of microfluidic multipoles with integrated manifold and valves, without important variations to the fabrication workflow presented in chapter 4. I have been aware of this limitation for a few years and had planned an internship in Nordin's research group to advance this concept, but it was canceled due to Covid19. I believe a collaboration with this research group would still be of interest. A microfabrication approach could also be considered as it would allow mass production of PCDs. However, it would require a complete reengineering of the fabrication workflow. I would only suggest this method after further proof of concept for applications are made.

8.2.4 Bubble nucleation.

From my experience, and by watching some of my colleagues and interns experiments, dealing with bubbles in PCDs remains a challenge. PCDs are vulnerable to air bubbles since they are comprised of an intricate system of channels. Bubbles can clog or change the hydraulic resistance of a channel, or they can get stuck in between the PCD and the surface. In both cases, that can make some pixel unusable. Of course, having a design that minimizes sharp corners, pre-filling the

systems with ethanol and making sure that no air is aspirated mitigate part of the problem, but it is not enough to completely remove the risk of bubbles. People working on PCD or other MFMs should have a good understanding of bubble nucleation in microfluidic device¹²⁵.

From my experience, the best way to avoid bubble nucleation is to make sure that gases solubilized in the fluids remain at equilibrium or undersaturated. The two factors that mainly affects gas solubility in microfluidic systems are the pressure difference in the system, and the change of temperature. This relation is described by Henry's law as $c_s = H(T)P_s$, where c_s is the equilibrium concentration, $H(T)$ is the Henri's law solubility constant that decreases with temperature, and P_s is the pressure of the gas in the vapor phase. A fluid at equilibrium in the reservoir will reach the end of the channel with a lower pressure, thus reducing gas solubilities and being oversaturated¹²⁵. In a similar manner, microfluidic systems are often heated. Gas solubilities decrease with an increase in temperature¹²⁵. If the reservoirs are colder than the microsystem, fluids will be oversaturated in gas.

When designing a PCD and an experiment, the pressure to flow the fluid should be kept low. Moreover, reservoirs should be kept at the same temperature that the PCD, or even a few degree higher if possible. Further experimentations, and some modification such as the addition of bubble traps might be required to make the PCD compatible with experiments in which the reagent must be kept cold, and the system be kept in an incubator.

8.2.5 Fluid compatibility and clogging

Some attention should be taken to assess the compatibility of the reagent used during an experiment. It is something that was overlooked in my articles, but that someone working with PCDs should consider. While the pixels are mostly isolated, a thin gradient is present in between pixels. Moreover, all aspirations are usually connected, which means that all the reagents are mixed in the aspiration fluid lines, and in the waste flask. Most of the time, it has no consequences. However, in some cases, it might lead to a reaction. An example of that was that while perfusing phloxine B and hematoxylin during a tissue staining experiment, the two reagents formed a slurry compound in the aspiration line that eventually clogged the PCD used.

Using the gradient and reaction in between pixels is also something I have tried to use during my PhD. One example is the use of Tollen's reagent and an aldehyde to pattern silver lines on a surface. A problem with that experiment was that both Tollen's reagent and aldehyde are mixed in the aspiration, which means that there was silver deposition in the system. The experiment worked. However, the system eventually failed due to clogging. Solutions to this problem could be found, for example by changing the PCD and fluid line material, or by injecting a solution that neutralizes the reaction. However, I would advise against reactive material deposition without the appropriate action taken.

8.2.6 Total reconfiguration vs minimum useful reconfiguration.

While doing my research, multiple discussions about the possibility of creating a fully reconfigurable PCD took place. However, despite looking great and have the potential to make a high-impact article, I don't think there is much point in doing a fully reconfigurable PCD. A fully reconfigurable 100-pixel PCD with reconfiguration between 3 reagents would require more than 300 valves and a countless number of connections. It would end up being extremely complicated, but not necessarily useful. I believe designing PCDs for specific applications is a lot more promising. For example, companion diagnostic PCDs could be designed to tests around a dozen drugs and drug concentration conditions. It could be partially reconfigurable in such way that the same readout marker can be injected in every pixel. It would only require only a handful of valve and control lines, while being clinically relevant. With an improvement in our fabrication method, I believe such PCDs could be routinely fabricated.

8.2.7 Checklist to access future experiment viability

From my experience on this project, I would say that we have sometimes used gross simplifications of PCDs to help us explain the device to nonexperts, but that those simplification caused problems later during tests for applications in which these simplifications finally mattered. However, most problems and dead ends could have been prevented by answering those next questions:

- 1) How to prevent contamination when installing and removing the MFM?
- 2) What will happen when the reagents mix in the aspirations tube?

- 3) Does the large velocity difference between a point under an injection and a stagnation point will affect my results?
- 4) Will my experiment setup generate bubbles in the systems?
- 5) In these exact experimental conditions, what will the confinement areas look like?
- 6) What will be the reagent consumption for this experiment?

These six simple questions encompassed most of the problems I was confronted to during my PhD. I would suggest that during experiment design, these questions should be answered before any further steps to access the experiment viability.

CHAPTER 9 CONCLUSION

9.1 Multiplex open-space microfluidics and the tyranny of numbers

I believe there is striking resemblance between some of the problems I face in my research, and the tyranny of number that thwarted computer design the '60s¹³¹. Engineers at Bell Laboratory, IBM and Texas Instruments could design computer and complex circuits but had no reliable way to fabricate those devices. Computers were fabricated from custom modules that were soldered by hand. As the circuit grew larger, the probability of a component with a defect or a bad solder joint increased, which make systems past a certain complexity almost impossible to produce and debug. Moreover, the amount of wiring became a reliability issue in itself.

I found myself in the same kind of position during my PhD. I had a certain level of frustration at being able to design the connection circuit of large scale and reconfigurable PCD, but being nowhere near close to being able to fabricate them. In other cases, I could fabricate the systems and perform a proof of concept. However, as long as the fabrication remains a bottleneck, experiment with PCD in life science will be limited and it will be impossible for the PCDs to become mainstream.

I see a clear parallel between the PCD and the tyranny of numbers, and I believe the comparison is also applicable to other highly multiplex microfluidic systems. Microfluidic researchers have developed various modules over the years, such as the gradient generator, mixer or integrated valves. However, the use of those modules (except valves) in multiplex microfluidic remains limited. A solution that emerged from the tyranny of number is the integrated circuit that allow the mass production of small, standardized, reliable and easy-to-assemble components. It is difficult to predict what the solution for multiplex microfluidic will be. Fluidic and electronics are two distinct fields, and it might not be an ideal way to separate a microfluidic system in subpart as fluidic connections are a source of problems, and the control of resistance is more complicated in fluidic than electronics. However, a certain standardization and improvement in chip interconnection would certainly help the creating of more complicated system. Improvement in high resolution 3D printing with both an increase in resolution and in build size could be another

approach. While I don't have the solution, it seems obvious to me that the microfluidic tyranny of numbers will have to be addressed if we ever are to see highly multiplex microfluidic systems used as mainstream tools.

9.2 Outlook

In this thesis, I proposed a new approach to liquid handling based on scalable and reconfigurable open-space microfluidic systems. The MFMs presented in this work are built upon the concept of the microfluidic probe, but they address the lack of parallelization of this device. The results are systems that are both highly scalable and compatible with immersed open surfaces, which is currently a gap in liquid handling system capabilities. The development of these new MFMs was based on three main steps. The first one was to identify a cheap, versatile and user-friendly fabrication method: stereolithography 3D printing. The exploration of MFM geometries and the design of small reconfigurable MFMs followed. The final step was the design of the PCD, a scalable multipolar architecture that allows the control of fluid in a large number of confinement areas.

In my opinion, two results really stand out of my PhD by their potential and originality. The first one is the use of small reconfigurable MFM as chemical stroboscope. These simple devices allow a reconfiguration in the order of the second, which is something few liquid handling systems can achieve. Chemical stroboscope could be used to pulse chemicals in the study of cellular pathway dynamics. A collaboration in progress should assess the chemical stroboscope potential.

The other result that stands out is the pixelated chemical display. While much work remains to improve its fabrication and ease of use, I believe that this system has a lot of potential. It offers a parallelization that is unprecedented in open-space microfluidics. At the start of my project, open-space microfluidic systems were seen as probe-like devices that must be scanned on a surface. PCD offers a new way to automatize parallel experiments on surfaces using a constant streaming flow, without the need for physical features such as wells. This architecture can be scaled up to any number of pixels, and the pixel size can be varied to fit the experiment requirement. Moreover, we demonstrated that this device is highly stable and that a faulty pixel would not jeopardize an entire experiment.

I believe my work was well received by the microfluidic community. I published three articles during this thesis, two of which in prestigious journal (PNAS and Nature Communications). I also had the chance to give two talks at the microTAS conference. Moreover, in our lab, two projects rely on devices that I designed during this thesis (the chemical strobe and the PCD). I am impatient to see the result of those projects as they will give more insight on the future of reconfigurable MFMs.

I think this thesis succeeded at establishing the basis for parallel open-space microfluidics devices. Systems from this thesis, however, may remain hard to use by non engineers in their current version, and they lack a high-throughput production method. A new generation of more user-friendly system combined with advance in 3D printing might just be the missing elements that would allow use MFMs to their full potential.

REFERENCES

1. Marx, V. Pouring over liquid handling. *Nat. Methods* **11**, 349 (2014).
2. Kong, F., Yuan, L., Zheng, Y. F. & Chen, W. Automatic liquid handling for life science: a critical review of the current state of the art. *J. Lab. Autom.* **17**, 169–85 (2012).
3. Bellavance, L., Burbaum, J. & Dunn, D. Miniaturisation of HTS assays. *Innov. Pharm. Technol.* 12–17 (2000).
4. Verch, T. & Bakhtiar, R. Miniaturized immunoassays: Moving beyond the microplate. *Bioanalysis* **4**, 177–188 (2012).
5. Nickischer, D. *et al.* *High Content Screening. High Content Screening: A Powerful Approach to Systems Cell Biology and Phenotypic Drug Discovery, Methods in Molecular Biology* vol. 1683 (Springer New York, 2018).
6. Neuzil, P., Giselbrecht, S., Länge, K., Huang, T. J. & Manz, A. Revisiting lab-on-a-chip technology for drug discovery. *Nat. Rev. Drug Discov.* **11**, 620–632 (2012).
7. Quake, S. Solving the Tyranny of Pipetting. *arxiv.org/abs/1802.05601* (2018).
8. Manz, A., Widmers, H. M. & Graber, N. Miniaturized total chemical analysis systems: A novel concept for chemical sensing. *Sensors Actuators B Chem.* **1**, 244–248 (1990).
9. Teh, S.-Y., Lin, R., Hung, L.-H. & Lee, A. P. Droplet microfluidics. *Lab Chip* **8**, 198 (2008).
10. Thorsen, T., Maerkl, S. J. & Quake, S. R. Microfluidic Large-Scale Integration. *Science* (80-.). **298**, 580–584 (2002).
11. Meister, A. *et al.* FluidFM: Combining Atomic Force Microscopy and Nanofluidics in a Universal Liquid Delivery System for Single Cell Applications and Beyond. *Nano Lett.* **9**, 2501–2507 (2009).
12. Tavana, H. *et al.* Nanolitre liquid patterning in aqueous environments for spatially defined reagent delivery to mammalian cells. *Nat. Mater.* **8**, 736–41 (2009).
13. Juncker, D., Schmid, H. & Delamarche, E. Multipurpose microfluidic probe. *Nat. Mater.* **4**, 622–8 (2005).

14. Lovchik, R. D., Kaigala, G. V., Georgiadis, M. & Delamarche, E. Micro-immunohistochemistry using a microfluidic probe. *Lab Chip* **12**, 1040 (2012).
15. Khartchenko, A. F. *et al.* QUANTITATIVE MICROIMMUNOHISTOCHEMISTRY (μ IC). 79–81 (2018).
16. Queval, A. *et al.* Chamber and microfluidic probe for microperfusion of organotypic brain slices. *Lab Chip* **10**, 326–334 (2010).
17. Sarkar, A., Kolitz, S., Lauffenburger, D. A. & Han, J. Microfluidic probe for single-cell analysis in adherent tissue culture. *Nat. Commun.* **5**, 3421 (2014).
18. Taylor, D. P., Zeaf, I., Lovchik, R. D. & Kaigala, G. V. Centimeter-Scale Surface Interactions Using Hydrodynamic Flow Confinements. *Langmuir* **32**, 10537–10544 (2016).
19. Banks, M. N., Cacace, A. M., O’Connell, J. & Houston, J. G. High-Throughput Screening: Evolution of Technology and Methods. *Drug Discov. Handb.* 559–602 (2005) doi:10.1002/0471728780.ch13.
20. Hasell, J. *et al.* A cross-country database of COVID-19 testing. *Sci. Data* **7**, 1–7 (2020).
21. C., S., N., A., Cui, J., Low, J. & Che, T. Practical Considerations of Liquid Handling Devices in Drug Discovery. in *Drug Discovery* (ed. El-Schemy, H. A.) 177–200 (InTech, 2013). doi:10.5772/52546.
22. McClymont, D. W. & Freemont, P. S. With all due respect to Maholo, lab automation isn’t anthropomorphic. *Nat. Biotechnol.* **35**, 312–314 (2017).
23. Ekins, S., Olechno, J. & Williams, A. J. Dispensing Processes Impact Apparent Biological Activity as Determined by Computational and Statistical Analyses. *PLoS One* **8**, 8–13 (2013).
24. Hadimioglu, B., Stearns, R. & Ellson, R. Moving Liquids with Sound: The Physics of Acoustic Droplet Ejection for Robust Laboratory Automation in Life Sciences. *J. Lab. Autom.* **21**, 4–18 (2016).
25. Ellson, R. *et al.* Transfer of low nanoliter volumes between microplates using focused acoustics - Automation considerations. *JALA - J. Assoc. Lab. Autom.* **8**, 29–34 (2003).

26. Delaney, J. T., Smith, P. J. & Schubert, U. S. Inkjet printing of proteins. *Soft Matter* **5**, 4866 (2009).
27. Li, J., Rossignol, F. & Macdonald, J. Inkjet printing for biosensor fabrication: combining chemistry and technology for advanced manufacturing. *Lab Chip* **15**, 2538–2558 (2015).
28. Squires, T. M. & Quake, S. R. Microfluidics: Fluid physics at the nanoliter scale. *Rev. Mod. Phys.* **77**, 977–1026 (2005).
29. Unger, M. A., Chou, H., Thorsen, T., Scherer, A. & Quake, S. R. Monolithic microfabricated valves and pumps by multilayer soft lithography. *Science (80-.)*. **2**, 8–11 (2000).
30. Liu, J., Hansen, C. & Quake, S. R. Solving the ‘world-to-chip’ interface problem with a microfluidic matrix. *Anal. Chem.* **75**, 4718–4723 (2003).
31. Einav, S. *et al.* Discovery of a hepatitis C target and its pharmacological inhibitors by microfluidic affinity analysis. *Nat. Biotechnol.* **26**, 1019–1027 (2008).
32. Lagus, T. P. & Edd, J. F. A review of the theory, methods and recent applications of high-throughput single-cell droplet microfluidics. *J. Phys. D. Appl. Phys.* **46**, (2013).
33. Brouzes, E. *et al.* Droplet microfluidic technology for single-cell high-throughput screening. *Proc. Natl. Acad. Sci. U. S. A.* **106**, 14195–14200 (2009).
34. Kaigala, G. V., Lovchik, R. D. & Delamarche, E. Microfluidics in the “Open Space” for Performing Localized Chemistry on Biological Interfaces. *Angew. Chemie Int. Ed.* **51**, 11224–11240 (2012).
35. Chen, D. *et al.* The chemistode: A droplet-based microfluidic device for stimulation and recording with high temporal, spatial, and chemical resolution. *PNAS* (2008).
36. Donovan, A. J., Liu, Y. & Donovan, A. J. Chap18 Chemistode for High Temporal- and Spatial- Resolution Chemical Analysis. in *Open-SpaceMicrofluidics: Concepts, Implementations, and Applications* (eds. Delamarche, E. & Kaigala, G. V.) 391–410 (Wiley-VCH Verlag GmbH & Co., 2018).
37. Piner, R. D., Zhu, J., Xu, F., Hong, S. & Mirkin, C. A. Dip-Pen nanolithography. *Science* **283**, 661–3 (1999).

38. Ginger, D. S., Zhang, H. & Mirkin, C. A. The Evolution of Dip-Pen Nanolithography. *Angew. Chemie Int. Ed.* **43**, 30–45 (2004).
39. Guillaume-Gentil, O. *et al.* Force-controlled manipulation of single cells: from AFM to FluidFM. *Trends Biotechnol.* **32**, 381–388 (2014).
40. Dörig, P. *et al.* Force-controlled spatial manipulation of viable mammalian cells and microorganisms by means of FluidFM technology. *Appl. Phys. Lett.* **97**, 023701 (2010).
41. Guillaume-Gentil, O., Mittelviehhaus, M., Dorwling-Carter, L., Zambelli, T. & Vorholt, J. A. Chap15 FluidFM Applications in Single-Cell Biology. in *Open-Space Microfluidics: Concepts, Implementations, Applications* (eds. Delamarche, E. & Kaigala, G. V.) 325–354 (Wiley-VCH Verlag GmbH & Co., 2018). doi:10.1002/9783527696789.ch15.
42. Ying, L. *et al.* The scanned nanopipette: a new tool for high resolution bioimaging and controlled deposition of biomolecules. *Phys. Chem. Chem. Phys.* **7**, 2859 (2005).
43. Bruckbauer, A. *et al.* Writing with DNA and Protein Using a Nanopipet for Controlled Delivery. *J. AM. CHEM. SOC* **124**, 8810–8811 (2002).
44. Bruckbauer, A. *et al.* Nanopipette Delivery of Individual Molecules to Cellular Compartments for Single-Molecule Fluorescence Tracking. *Biophys. J.* **93**, 3120–3131 (2007).
45. Seger, R. A. *et al.* Voltage controlled nano-injection system for single-cell surgery. doi:10.1039/c2nr31700a.
46. Fujii, T. *et al.* Direct metabolomics for plant cells by live single-cell mass spectrometry. *Nat. Protoc.* **10**, 1445–1456 (2015).
47. Saha-Shah, A., Green, C. M., Abraham, D. H. & Baker, L. A. Segmented flow sampling with push–pull theta pipettes. *Analyst* **141**, 1958–1965 (2016).
48. Saha-Shah, A. *et al.* Nanopipettes: probes for local sample analysis. *Chem. Sci.* **6**, 3334–3341 (2015).
49. Shiku, H. *et al.* A microfluidic dual capillary probe to collect messenger RNA from adherent cells and spheroids. *Anal. Biochem.* **385**, 138–142 (2009).

50. Delamarche, E., Bernard, A., Schmid, H., Michel, B. & Biebuyck, H. Patterned delivery of immunoglobulins to surfaces using microfluidic networks. *Science* (80-.). **276**, 779–781 (1997).
51. Ziegler, J., Zimmermann, M., Hunziker, P. & Delamarche, E. High-performance immunoassays based on through-stencil patterned antibodies and capillary systems. *Anal. Chem.* **80**, 1763–1769 (2008).
52. Routenberg, D. A. & Reed, M. A. Microfluidic probe: a new tool for integrating microfluidic environments and electronic wafer-probing. *Lab Chip* **10**, 123–127 (2010).
53. Søe, M. J. *et al.* HistoFlex—a microfluidic device providing uniform flow conditions enabling highly sensitive, reproducible and quantitative in situ hybridizations. *Lab Chip* **11**, 3896 (2011).
54. Kim, M. S. *et al.* Breast Cancer Diagnosis Using a Microfluidic Multiplexed Immunohistochemistry Platform. *PLoS One* **5**, e10441 (2010).
55. Chang, T. C. *et al.* Parallel microfluidic chemosensitivity testing on individual slice cultures. *Lab Chip* **14**, 4540–4551 (2014).
56. Kaigala, G. V., Lovchik, R. D., Drechsler, U. & Delamarche, E. A Vertical Microfluidic Probe. *Langmuir* **27**, 5686–5693 (2011).
57. Cors, J. F., Lovchik, R. D., Delamarche, E. & Kaigala, G. V. A compact and versatile microfluidic probe for local processing of tissue sections and biological specimens. *Rev. Sci. Instrum.* **85**, 034301 (2014).
58. Cors, J. F., Kashyap, A., Fomitcheva Khartchenko, A., Schraml, P. & Kaigala, G. V. Tissue lithography: Microscale dewaxing to enable retrospective studies on formalin-fixed paraffin-embedded (FFPE) tissue sections. *PLoS One* **12**, e0176691 (2017).
59. Kashyap, A., Autebert, J., Delamarche, E. & Kaigala, G. V. Selective local lysis and sampling of live cells for nucleic acid analysis using a microfluidic probe. *Sci. Rep.* **6**, 29579 (2016).
60. Sarkar, A., Kolitz, S., Lauffenburger, D. A. & Han, J. Microfluidic probe for single-cell

- analysis in adherent tissue culture. *Nat. Commun.* **5**, (2014).
61. Qasaimeh, M. A., Astolfi, M., Pyzik, M., Vidal, S. & Juncker, D. Neutrophils migrate longer distance in moving microfluidic concentration gradients compared to static ones. in *17th International Conference on Miniaturized Systems for Chemistry and Life Sciences* (2013).
 62. Qasaimeh, M. a, Gervais, T. & Juncker, D. Microfluidic quadrupole and floating concentration gradient. *Nat. Commun.* **2**, 464 (2011).
 63. Cors, J. F. *et al.* Chap 2 Hierarchical hydrodynamic flow confinement: Efficient use and retrieval of chemicals for microscale chemistry on surfaces. in *Open-Space Microfluidics: Concepts, Implementations, and Applications* (eds. Delamarche, E. & Kaigala, G. V.) 21–45 (Wiley-VCH Verlag GmbH & Co., 2018). doi:10.1021/la500875m.
 64. Safavieh, M., Qasaimeh, M. A., Vakil, A., Juncker, D. & Gervais, T. Two-Aperture Microfluidic Probes as Flow Dipole: Theory and Applications. *Sci. Rep.* **5**, 11943 (2015).
 65. Amin, R. *et al.* 3D-printed microfluidic devices. *Biofabrication* **8**, 1–16 (2016).
 66. Comina, G., Suska, A. & Filippini, D. Lab on a Chip PDMS lab-on-a-chip fabrication using 3D printed templates. **14**, (2014).
 67. Kamei, K. *et al.* 3D printing of soft lithography mold for rapid production of polydimethylsiloxane-based microfluidic devices for cell stimulation with concentration gradients. *Biomed. Microdevices* **17**, 36 (2015).
 68. Brunet, A., Labelle, F., Wong, P. & Gervais, T. Reconfigurable Microfluidic Magnetic Valve Arrays: Towards a Radiotherapy-Compatible Spheroid Culture Platform for the Combinatorial Screening of Cancer Therapies. *Sensors* **17**, 2271 (2017).
 69. Gong, H., Bickham, B. P., Woolley, A. T. & Nordin, G. P. Custom 3D printer and resin for $18\ \mu\text{m} \times 20\ \mu\text{m}$ microfluidic flow channels. *Lab Chip* **17**, 2899–2909 (2017).
 70. Au, A. K., Lee, W. & Folch, A. Mail-order microfluidics: evaluation of stereolithography for the production of microfluidic devices. *Lab Chip* **14**, 1294–1301 (2014).
 71. Bhattacharjee, N., Urrios, A., Kang, S. & Folch, A. The upcoming 3D-printing revolution in microfluidics. *Lab Chip* **16**, 1720–1742 (2016).

72. Becker, H. It's the economy... *Lab Chip* **9**, 2759–2762 (2009).
73. Au, A. K., Huynh, W., Horowitz, L. F. & Folch, A. 3D-Printed Microfluidics. *Angew. Chemie Int. Ed.* **55**, 3862–3881 (2016).
74. Beauchamp, M. J., Nordin, G. P. & Woolley, A. T. Moving from millifluidic to truly microfluidic sub-100- μm cross-section 3D printed devices. *Anal. Bioanal. Chem.* **409**, 4311–4319 (2017).
75. Anderson, K. B., Lockwood, S. Y., Martin, R. S. & Spence, D. M. A 3D Printed Fluidic Device that Enables Integrated Features. doi:10.1021/ac4009594.
76. Farsari, M. & Chichkov, B. N. Materials processing: Two-photon fabrication. *Nat. Photonics* **3**, 450–452 (2009).
77. Dehaeck, S., Scheid, B. & Lambert, P. Adaptive stitching for meso-scale printing with two-photon lithography. *Addit. Manuf.* **21**, 589–597 (2018).
78. Gong, H., Beauchamp, M., Perry, S., Woolley, A. T. & Nordin, G. P. Optical approach to resin formulation for 3D printed microfluidics. *RSC Adv.* **5**, 106621–106632 (2015).
79. Kotz, F. *et al.* Three-dimensional printing of transparent fused silica glass. *Nature* **544**, 337–339 (2017).
80. Shallan, A. I., Smejkal, P., Corban, M., Guijt, R. M. & Breadmore, M. C. Cost-effective three-dimensional printing of visibly transparent microchips within minutes. *Anal. Chem.* **86**, 3124–3130 (2014).
81. Au, A. K., Bhattacharjee, N., Horowitz, L. F., Chang, T. C. & Folch, A. 3D-printed microfluidic automation. *Lab Chip* **15**, 1934–1941 (2015).
82. Lee, Y.-S., Bhattacharjee, N. & Folch, A. 3D-printed Quake-style microvalves and micropumps. *Lab Chip* **18**, 1207–1214 (2018).
83. Gong, H., Woolley, A. T. & Nordin, G. P. 3D printed high density, reversible, chip-to-chip microfluidic interconnects. *Lab Chip* **18**, 639–647 (2018).
84. Takenaga, S. *et al.* Fabrication of biocompatible lab-on-chip devices for biomedical applications by means of a 3D-printing process. *Phys. status solidi* **212**, 1347–1352 (2015).

85. Melin, J. & Quake, S. R. Microfluidic Large-Scale Integration: The Evolution of Design Rules for Biological Automation. *Annu. Rev. Biophys. Biomol. Struct.* **36**, 213–231 (2007).
86. Hua, Z. *et al.* A versatile microreactor platform featuring a chemical-resistant microvalve array for addressable multiplex syntheses and assays. *J. Micromechanics Microengineering* **16**, 1433–1443 (2006).
87. Lee, D. W. & Cho, Y.-H. High-radix microfluidic multiplexer with pressure valves of different thresholds. *Lab Chip* **9**, 1681 (2009).
88. Grover, W. H., Ivester, R. H. C., Jensen, E. C. & Mathies, R. A. Development and multiplexed control of latching pneumatic valves using microfluidic logical structures. *Lab Chip* **6**, 623 (2006).
89. Rhee, M. & Burns, M. A. Microfluidic pneumatic logic circuits and digital pneumatic microprocessors for integrated microfluidic systems. *Lab Chip* **9**, 3131 (2009).
90. Hele-Shaw, H. S. The Flow of Water. *Nature* **58**, 34–36 (1898).
91. Kirby, B. J. *Micro- and Nanoscale Fluid Mechanics: Transport in Microfluidic Devices*. (Cambridge University Press, 2010).
92. Goyette, P.-A. *et al.* Microfluidic multipoles theory and applications. *Nat. Commun.* **10**, 1781 (2019).
93. Boulais, E. & Gervais, T. Two-dimensional convection–diffusion in multipolar flows with applications in microfluidics and groundwater flow. *Phys. Fluids* **32**, 122001 (2020).
94. Cummings, Li. m., Hohlov, Y. E., Howison, S. D. & Kornev, K. Two-dimensional solidification and melting in potential flows. *J. Fluid Mech.* **378**, 1–18 (1999).
95. Safavieh, M., Qasaimeh, M. A., Vakil, A., Juncker, D. & Gervais, T. Two-Aperture Microfluidic Probes as Flow Dipole: Theory and Applications. *Sci. Rep.* **5**, 11943 (2015).
96. Lovchik, R. D., Drechsler, U. & Delamarche, E. Multilayered microfluidic probe heads. *J. Micromechanics Microengineering* **19**, 115006 (2009).
97. Ho, C. M. B., Ng, S. H., Li, K. H. H. & Yoon, Y. J. 3D printed microfluidics for biological applications. *Lab Chip* **15**, 3627–3637 (2015).

98. Boulais, É. & Gervais, T. Chap 4 Hele-Shaw flow theory in the context of open microfluidics: from dipoles to quadrupoles. in *Open-Space Microfluidics. Concepts, Implementations, Applications* 63–82 (2016).
99. Brimmo, A., Goyette, P., Alnemari, R., Gervais, T. & Qasaimeh, M. A. 3D Printed Microfluidic Probes. *Sci. Rep.* **8**, 10995 (2018).
100. Autebert, J., Kashyap, A., Lovchik, R. D., Delamarche, E. & Kaigala, G. V. Hierarchical hydrodynamic flow confinement: efficient use and retrieval of chemicals for microscale chemistry on surfaces. *Langmuir* **30**, 3640–5 (2014).
101. Qasaimeh, M. A., Gervais, T. & Juncker, D. Microfluidic quadrupole and floating concentration gradient. (2011) doi:10.1038/ncomms1471.
102. Juncker, D., Bergeron, S., Laforte, V. & Li, H. Cross-reactivity in antibody microarrays and multiplexed sandwich assays: Shedding light on the dark side of multiplexing. *Curr. Opin. Chem. Biol.* **18**, 29–37 (2014).
103. Choi, H. M. T. *et al.* Third-generation in situ hybridization chain reaction: multiplexed, quantitative, sensitive, versatile, robust. *Development* **145**, dev165753 (2018).
104. Eng, C. H. L., Shah, S., Thomassie, J. & Cai, L. Profiling the transcriptome with RNA SPOTs. *Nat. Methods* **14**, 1153–1155 (2017).
105. Zambrano, S., de Toma, I., Piffer, A., Bianchi, M. E. & Agresti, A. NF- κ B oscillations translate into functionally related patterns of gene expression. *Elife* **5**, 1–38 (2016).
106. Purvis, J. E. & Lahav, G. Encoding and decoding cellular information through signaling dynamics. *Cell* **152**, 945–956 (2013).
107. Hersen, P., McClean, M. N., Mahadevan, L. & Ramanathan, S. Signal processing by the HOG MAP kinase pathway. *Proc Natl Acad Sci U S A* **105**, 7165–7170 (2008).
108. Li, P. & Elowitz, M. B. Communication codes in developmental signaling pathways. *Development* **146**, dev170977 (2019).
109. Nandagopal, N. *et al.* Dynamic Ligand Discrimination in the Notch Signaling Pathway. *Cell* **172**, 869–880.e19 (2018).

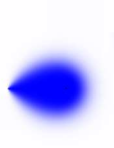
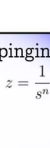
110. Ainla, A., Jeffries, G. D. M., Brune, R., Orwar, O. & Jesorka, A. A multifunctional pipette. *Lab Chip* **12**, 1255 (2012).
111. Chen, D. *et al.* The chemistode: a droplet-based microfluidic device for stimulation and recording with high temporal, spatial, and chemical resolution. *Proc. Natl. Acad. Sci. U. S. A.* **105**, 16843–8 (2008).
112. Mao, S. *et al.* Microchemical Pen: An Open Microreactor for Region-Selective Surface Modification. *ChemPhysChem* **100084**, 1–6 (2016).
113. Ainla, A., Jeffries, G. & Jesorka, A. Hydrodynamic Flow Confinement Technology in Microfluidic Perfusion Devices. *Micromachines* **3**, 442–461 (2012).
114. Taylor, D. P., Zeaf, I., Lovchik, R. D. & Kaigala, G. V. Centimeter-Scale Surface Interactions Using Hydrodynamic Flow Confinements. *Langmuir* **32**, 10537–10544 (2016).
115. Bazant, M. Z. Conformal mapping of some non-harmonic functions in transport theory. *Proc. R. Soc. A Math. Phys. Eng. Sci.* **460**, 1433–1452 (2004).
116. Shenoy, A., Rao, C. V. & Schroeder, C. M. Stokes trap for multiplexed particle manipulation and assembly using fluidics. *Proc. Natl. Acad. Sci.* **113**, 3976–3981 (2016).
117. Bruus, H. *Theoretical microfluidics*. (Oxford University Press, 2008).
118. Metropolis, N. & Ulam, S. The Monte Carlo Method. *J. Am. Stat. Assoc.* **44**, 335–341 (1949).
119. Phipps, C. A. *Fundamentals of Electrical Control*. (1999).
120. Hitzbleck, M., Kaigala, G. V., Delamarche, E. & Lovchik, R. D. The floating microfluidic probe: Distance control between probe and sample using hydrodynamic levitation. *Appl. Phys. Lett.* **104**, 263501 (2014).
121. Ebina, W., Rowat, A. C. & Weitz, D. A. Electrodes on a budget: Micropatterned electrode fabrication by wet chemical deposition. *Biomicrofluidics* **3**, 1–6 (2009).
122. Rajesh, P. S. M. *et al.* Continuous and selective-area coating of silver on fiber-reinforced polymer composites for aerospace applications. *Mater. Today Commun.* **18**, 206–212 (2019).

123. Lee, J. Y., An, J. & Chua, C. K. Fundamentals and applications of 3D printing for novel materials. *Appl. Mater. Today* **7**, 120–133 (2017).
124. Kawamoto, H. The history of liquid-crystal displays. *Proc. IEEE* **90**, 460–500 (2002).
125. Iago Pereiroa, Anna Fomitcheva Khartchenkoa, Lorenzo Petrinia, G. V. K. Nip the bubble in the bud: a guide to avoid gas nucleation in microfluidics. *J. Mater. Chem. B* **6**, 1–3 (2018).
126. Boyadjian, O., Boulais, É. & Gervais, T. Experiments on transformation microfluidics: cloaking flow and transport without metamaterials. *im*, 1–8 (2020).
127. Cox, K. L. Immunoassay Development, Optimization and Validation Flow Chart. in *ImmunoAssay Methods* (eds. Markossian, Grossman & Brimacombe) 1–38 (2011).
128. Ouellet, E. *et al.* Parallel microfluidic surface plasmon resonance imaging arrays. *Lab Chip* **10**, 581–588 (2010).
129. Brimmo, A. Microfluidic Probe for Multiphysics Enabled Single Cell Manipulation. in *Proceedings of MARSS* (2020). doi:10.1109/MARSS49294.2020.9307910.
130. Gong, H., Woolley, A. T. & Nordin, G. P. 3D printed selectable dilution mixer pumps. *Biomicrofluidics* **13**, 014106 (2019).
131. J., A., M. & W., J., P. The Technological Impact of Transistors. *Proc. IRE* 955–959 (1958).
132. Batchelor, G. K. *An introduction to fluid dynamics*. (Cambridge University Press, 2000).
133. Driscoll, T. A. & Trefethen, L. N. *Schwarz-Christoffel Mapping*. vol. 466 (Cambridge University Press, 2002).

APPENDIX A LIST OF CONFORMAL TRANSFORMS AND THE LINK BETWEEN DIFFERENT GEOMETRIES OF MICROFLUIDIC MULTIPOLES

This table, originally presented in the supplementary information of Goyette & al. Nat. Commun. (2019), present a list of conformal transformation and the MFMs that can be generated. The left column are solutions in streamline coordinates. The middle group represents simple MFM units that can be generated from the left column. The right column represents advanced MFM families that can be generated from transforming the unit from the middle column.

Table A-9-1. Microfluidic multipole transformation list

Semi-infinite line in plane flow $C = 1/2 \left(1 \pm \operatorname{erf} \left(\operatorname{Im} \left(\sqrt{\operatorname{Pe} (w - w_{\text{stag}})} \right) \right) \right)$ 	Microfluidic dipole $w = \log(z) - \alpha \log(z+1)$ 	Flower multipole $z = s^n - 1$ 
		Homogeneous multipole $z = 1/2 (s^n - 1)$ 
		Polygonal multipole $z = s^n$ 
		Impinging flows $z = \frac{1}{s^n} - 1$ 
	Single-petal flower $w = -2\alpha \cdot \log(z) + \log(z-1) + \log(z+1)$ 	Alternating petal flower $z = s^n$ 
	Confined dipole $w = \left(\frac{\alpha-1}{2} \right) (\log(z-1) + \log(z+1)) + \log(z) - \alpha \log(z + \tanh \pi)$ 	Multipole array $z = \frac{e^{\pi s} + 1}{e^{\pi s} - 1}$ 
Two semi-infinite lines in plane flow $C \approx 1/2 \left(1 \pm \left(\operatorname{erf} \left(\operatorname{Im} \sqrt{\operatorname{Pe} (\log(w) - w_{\text{stag}})} \right) + \operatorname{erf} \left(\operatorname{Im} \sqrt{\operatorname{Pe} (\log(w) - \pi i)} \right) \right) \right)$ 	Microfluidic quadrupole $w = \log(z-1) + \log(z+1) - \alpha \log(z-i) - \alpha \log(z+i)$ 	Alternating multipoles $z = s^n$ 
One semi-infinite and one finite line in plane flow Numerical results See Choi 2004	Nested dipoles $w = \beta \log(z-1) + \log(z) - \log(z+1) - \alpha \beta \log(z+2)$ 	

APPENDIX B CHEMICAL STROBOSCOPE FLOW RATE CORRECTION

To keep the “petals” of an rMFM at a constant width while pulsing the system and using it as a chemical probe, the ratio between aspiration and injection (that we define as α) must be varied depending on the number of apertures in operation. The reason behind the need for this correction can be understood from the conformal mapping of a rMFM. The advection-diffusion solution of a rMFM with only one aperture operating is a microfluidic dipole. When a second aperture is turned on, the advection diffusion of a petal follows still follow the dipole solution but compressed in half the complex plane. It results in a compressed petal width. A similar effect is observed for any number of injections turned on. The advection diffusion of a petal in an 8-petal rMFM follows the dipole solution but compressed in one eighth of the complex plane. Using the convection-diffusion model, the aspiration to injection ratio α can be calculated to compensate the width compression for each number of petals turned on. It allows the creation of a chemical stroboscope with constant petals width. The following table presents the alpha correction for 1 to 8 petals working for an initial $\alpha = 2$.

Table C-9-2 α correction for a constant pattern width using the rMFM

Nb pumps ON	α Correction Factor	α_{eff} (example for $\alpha=2$)	Qaps (example for $Q_{inj}=0.2\mu\text{L/s}$)
		$\alpha_{eff} = \alpha_8 \cdot correction\ factor$	$Q_{asp} = (Nb\ pumps)\alpha_{eff}Q_{inj}$
8	1.00	2.00	3.20
7	1.06	2.12	2.97
6	1.15	3.00	3.60
5	1.25	2.50	2.50
4	1.42	4.00	3.20
3	1.76	3.52	2.11
2	2.44	5.00	2.00
1	4.72	9.44	1.89

APPENDIX C RECONFIGURABLE MFMS EXTENDED DATASET

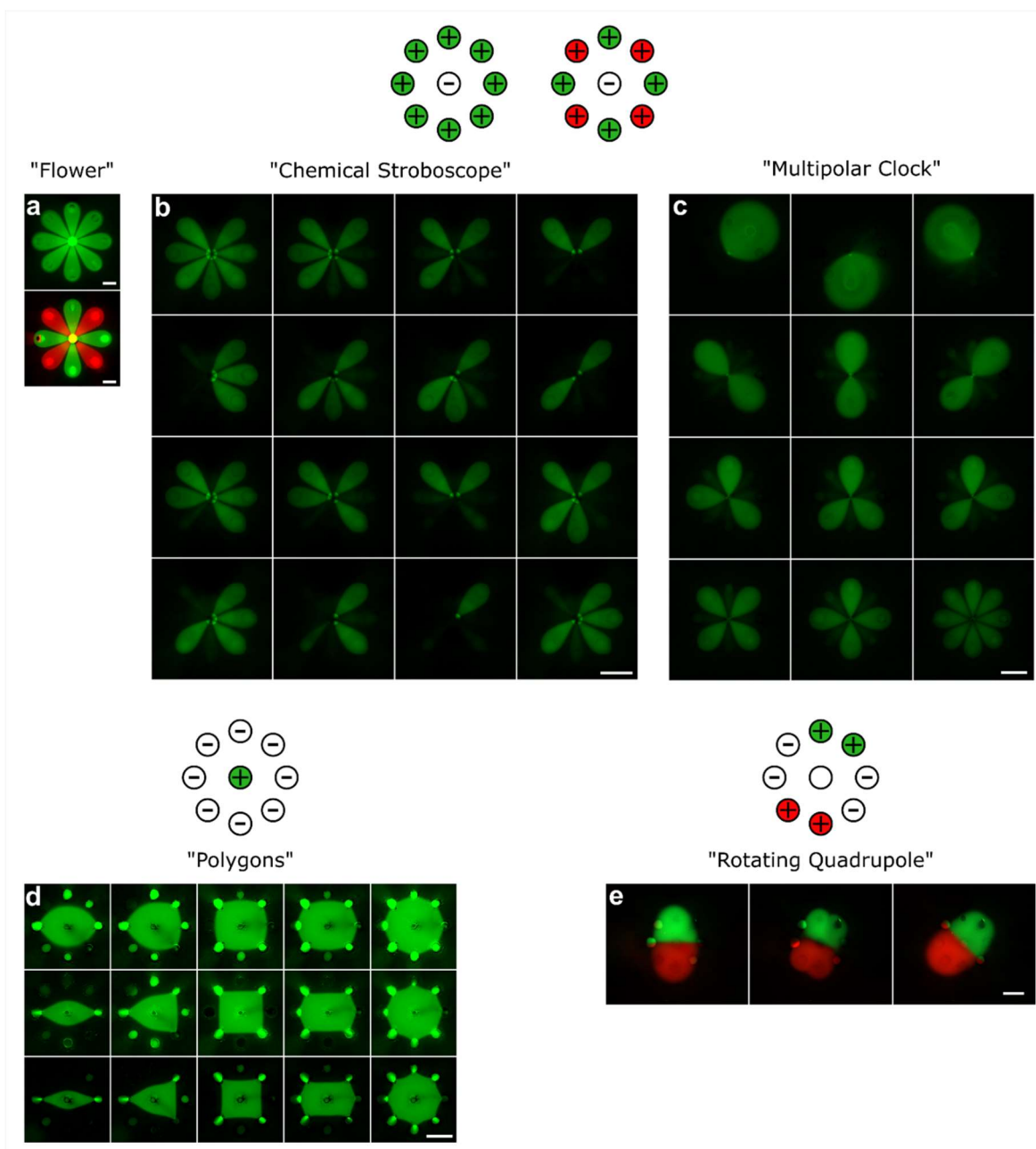


Figure B.9.1 Multiple injection/aspiration configurations and fluorescent micrograph made using an rMFM. All images from a set were taken in a single experiment except for (a). a) Flower, b) Chemical Stroboscope, c) Multipolar Clock, d) Polygon, e) Rotation Quadrupole. All scale bars are 500 μm . This figure is reproduced with permission from the supplementary information of Goyette & al. Nat. Commun. (2019).

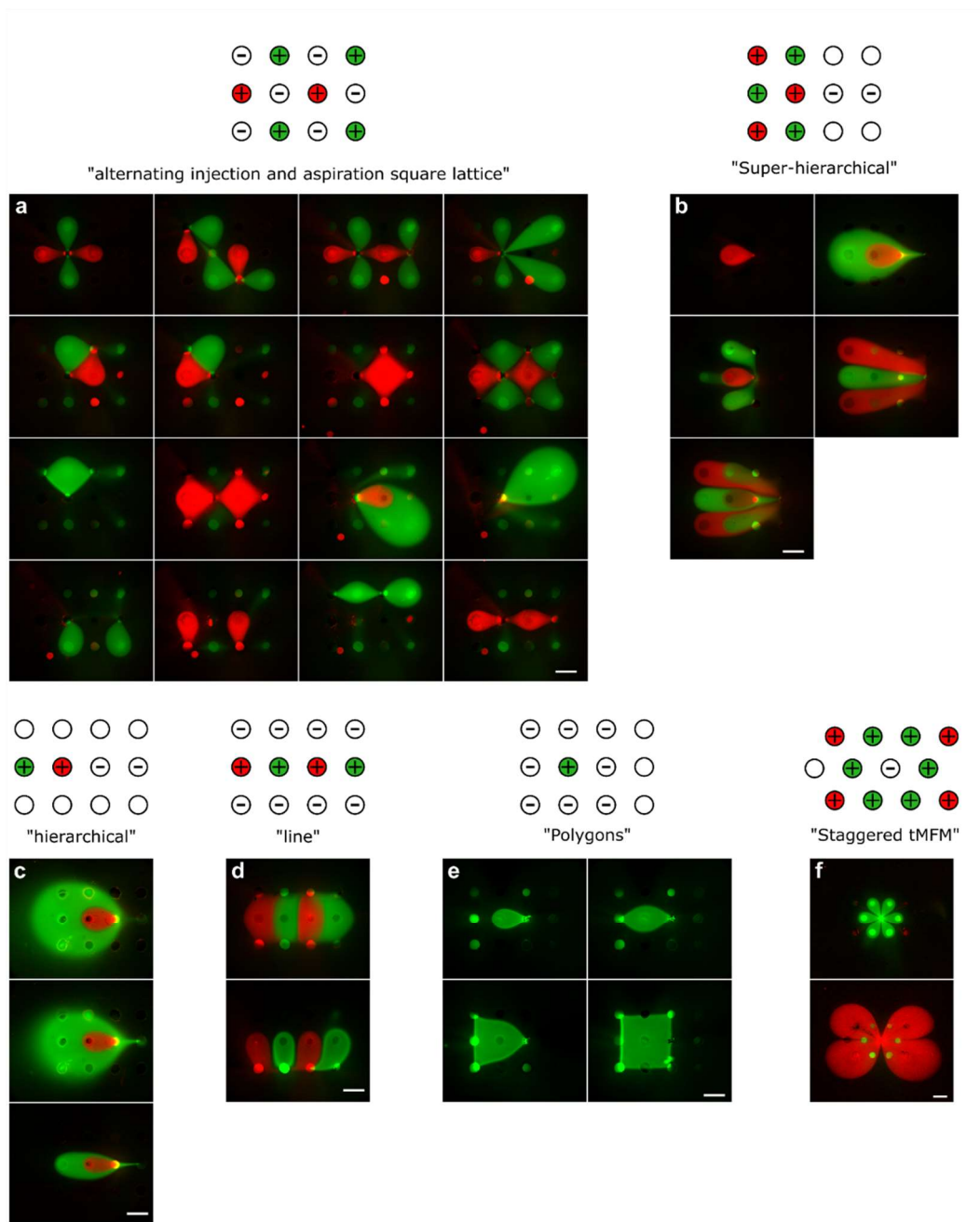


Figure B.9.2 Multiple injection/aspiration configurations and fluorescent micrograph made using a 12-aperture tMFM. All images from a set were taken in a single experiment. a) Alternating square lattice, b) Super-hierarchical, c) hierarchical, d) line, e) Polygons, f) Staggered tMFM. All scale bars are 500 μm . This figure is reproduced with permission from the supplementary information of Goyette & al. Nat. Commun. (2019).

APPENDIX D IMMUNOFLUORESCENT BACKGROUND COMPARISON WITH A NULL CONCENTRATION CONFINEMENT AREA

This appendix presents the comparison in between the fluorescence level of a “petal” injecting a solution with an analyte concentration = 0, and the background level. The background level was considered in regions where no analytes were injected, but in an area where detection antibody overlapped. In this regard, the petal with $c=0$ and the background undergo the exact same process. It is then not surprising that they have equal fluorescent level. We perform this experiment to confirm that the background could be considered as a data point with $c=0$, thus allowing us to test one more analyte level with the petal.

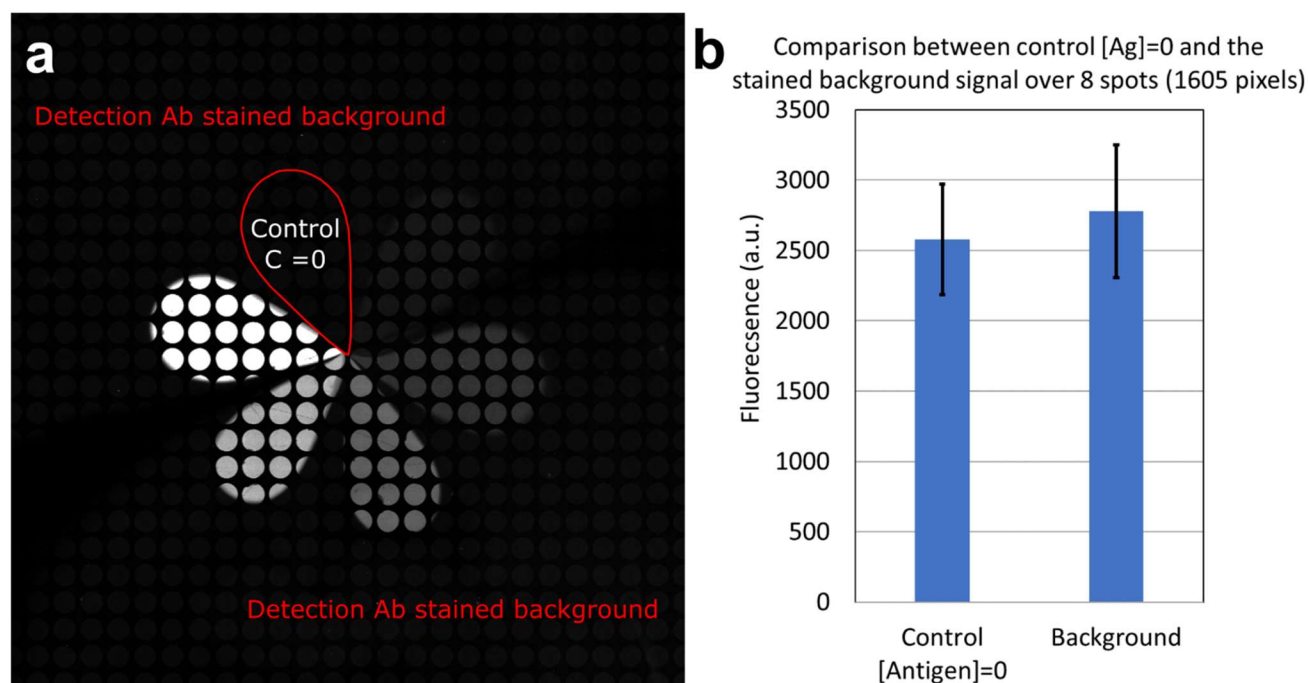


Figure D.9.3 a) *Fluorescent micrograph of an immunoassay experiment with one confinement area with a null concentration of antigen.* b) *Fluorescent level of a petal injecting a solution with null concentration of analyte and of the detection Ab stained background. Measurement made on 8 spots and 1605 pixels.* This figure is reproduced with permission from the supplementary information of Goyette & al. Nat. Commun. (2019).

APPENDIX E SUPPLEMENTARY INFORMATION, PIXEL-BASED OPEN-SPACE MICROFLUIDICS FOR VERSATILE SURFACE PROCESSING

Pierre-Alexandre Goyette, Étienne Boulais, Maude Tremblay, Thomas Gervais

Corresponding author: Thomas Gervais

Email: thomas.gervais@polymtl.ca

Table of Content

Pixel-based open-space microfluidics for versatile surface processing

1. Supplementary figures

2. Transport analytics

2.1 Transport model

2.2 Details on Schwarz-Christoffel transformation

3. PCD stability analysis

3.1 Stability analysis overview

3.2 Stability analysis visual protocol

3.3 Stability analysis detailed results

4. Reagent switching time

4.1 Reagent switching model

4.2 Characterisation of experimental reagent switching time

4.3 Reagent switching video frames

5. References

1. Supplementary figures

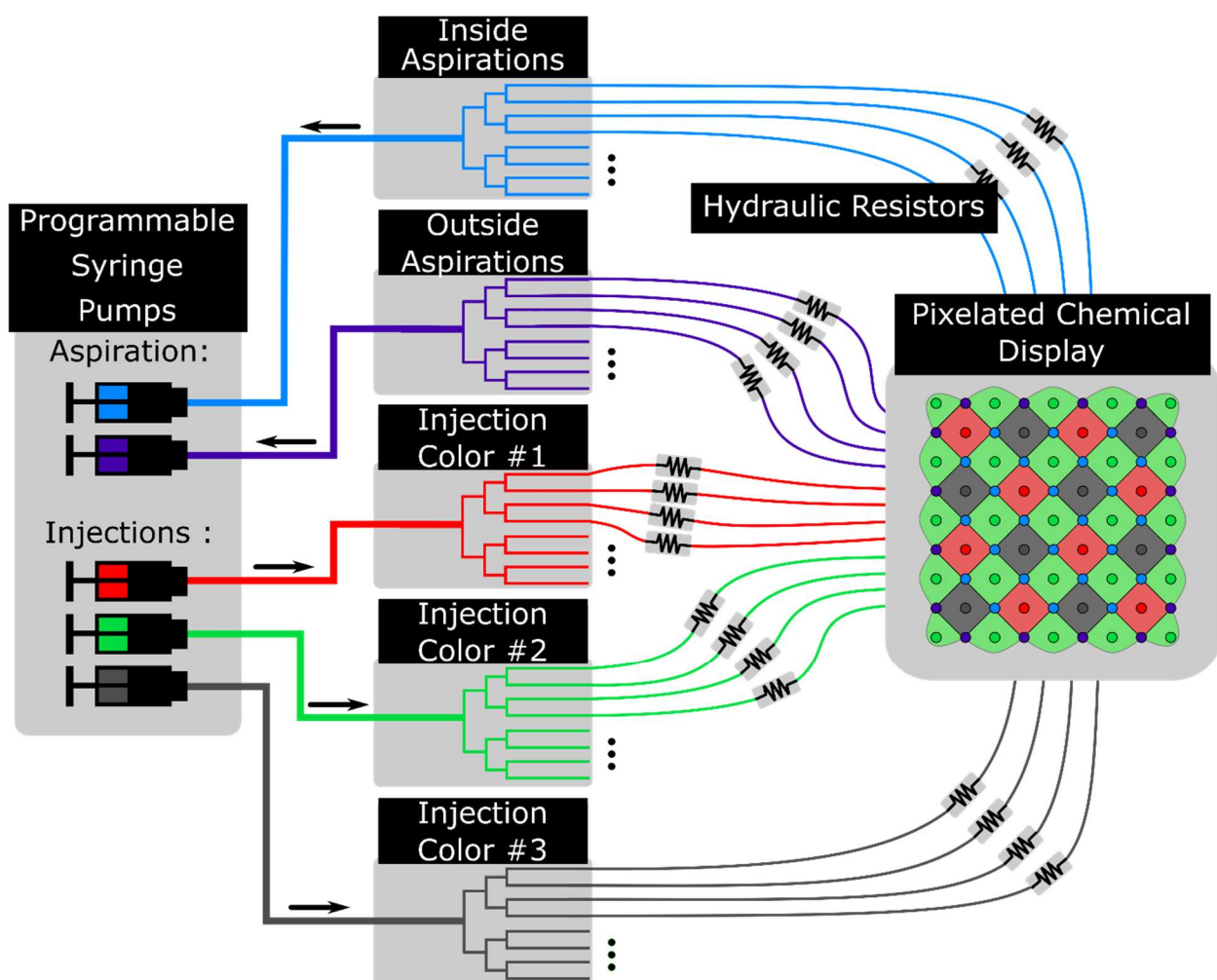


Fig. S1. Pixelated chemical display (PCD) manifold schematic for static experiments. For a static experiment, the number of pumps required is the number of reagents used plus two. Only one pump per color is used. All injections injecting the same color are routed to a single programmable pump using a custom-built manifold. PCD can be fabricated to generate any fixed chemical patterns by connecting the injections to the appropriate manifolds. The aspirations are separated in two groups, the inside aspirations, aspirating at the same absolute rate than the injections, and the outside aspirations, which serve to tune the total net flow rate of the PCD. By changing their aspiration rate, the PCD can be used in a globally confined or unconfined way. The tubes between the manifold and the PCD serve as precision hydraulic resistors to match the flow rates.

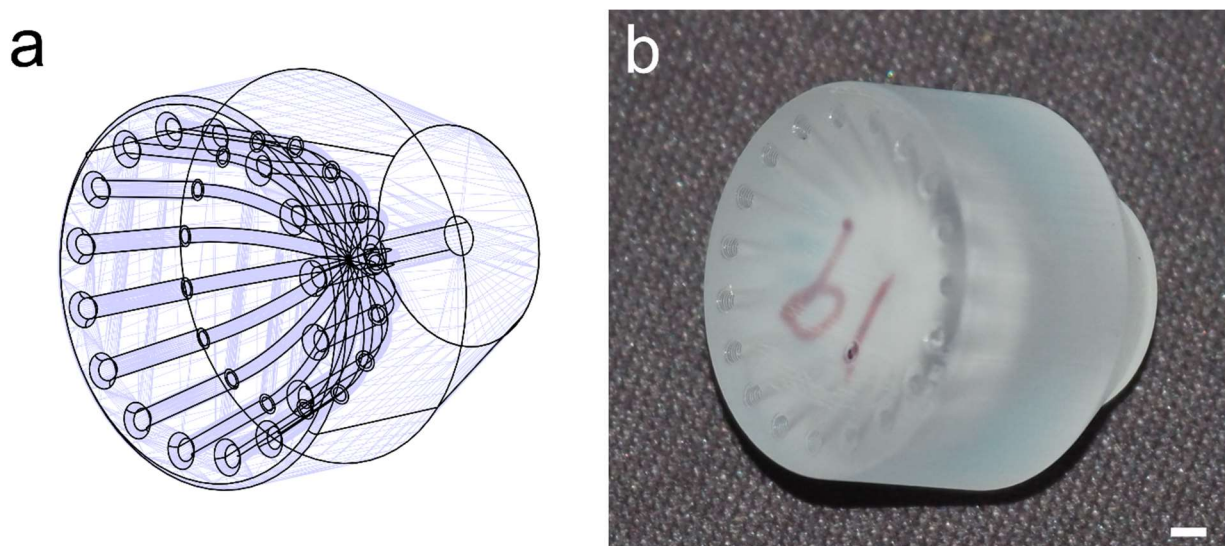


Fig. S2. Custom built manifolds. a) CAD of a 16:1 manifold that allows to connect 16 PCD aperture to one pump or valve. Manifold use a radial architecture to make sure that the flow is separated equally between every channels. The same basic architecture was used to make manifold allowing from 2 to 32 tube connections. To create larger manifold, for example a 64:1, we used multiple layer of manifolds, for example a 4:1 and a second layer of 4 16:1 manifold. b) A 3D printed manifold. Scale bar represent 1 mm.

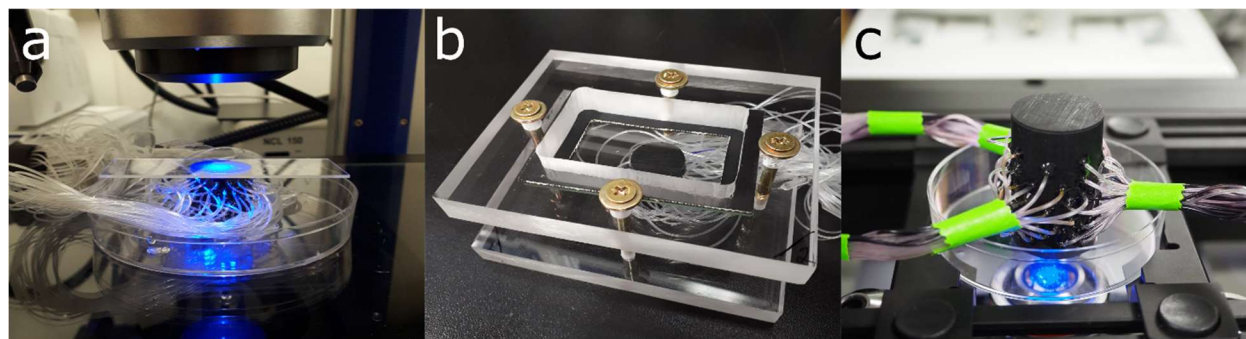


Fig. S3. Type of experimental setup used. a) Upright setup: the glass slide is simply positioned over the PCD. b) Second upright setup: a rigid setup holds the glass slide in place over the PCD. c) Immersed sample setup: the PCD is positioned and operated in a petri dish. Its own weight is sufficient to hold it in place.

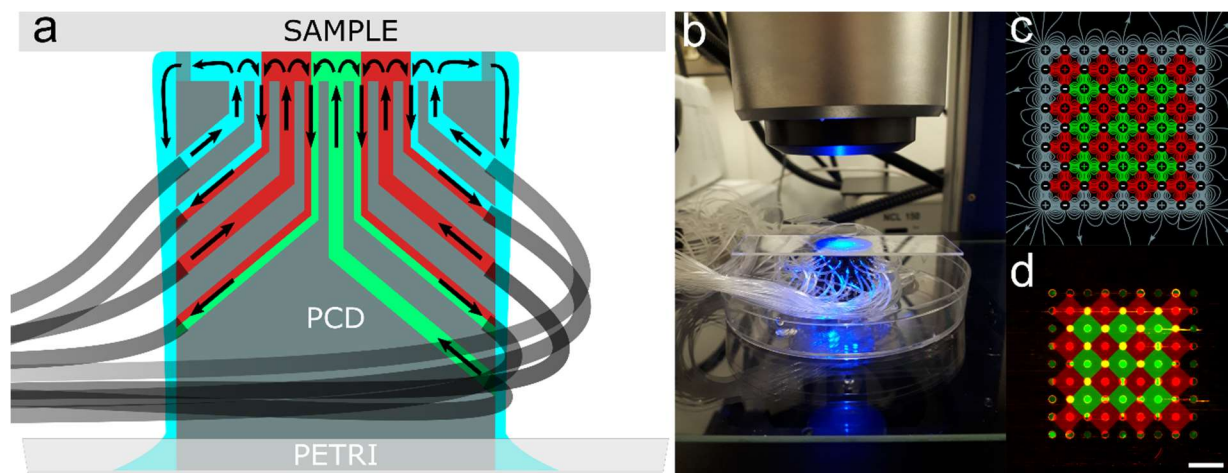


Fig. S4. Using a globally unconfined PCD in an upright configuration. (a) Schematic of a PCD working in an upright configuration on a dry surface. In this configuration, the PCD is unconfined and has a positive net flow rate. The excess of fluid is collected in the petri dish. (b) Photograph on a PCD being used in an upright configuration. (c) Theoretical flow lines of an unconfined PCD. When using a globally unconfined PCD, the outmost injection can inject a neutral solution. (d) Fluorescence micrograph of an unconfined PCD used in an upright configuration and injecting a neutral solution (here water) by its outmost injections. Scale bar represents 1 mm.

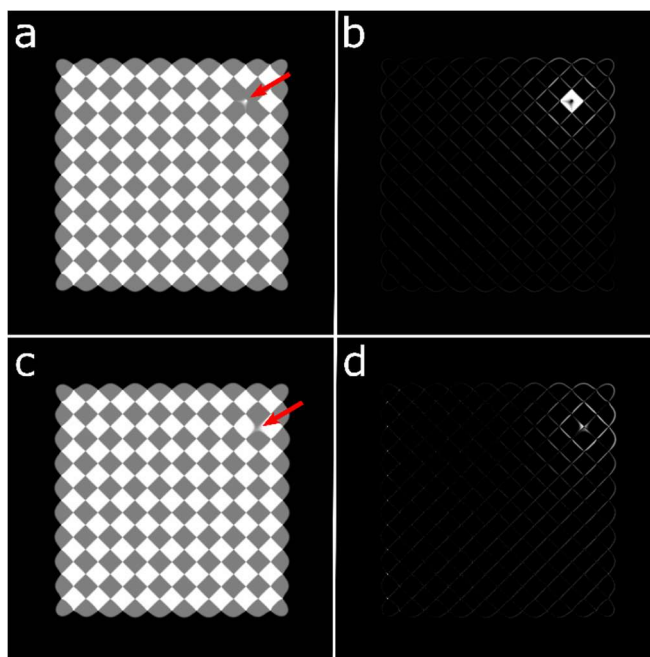


Fig. S5. Effect of faulty pixels. a) Simulation of a faulty injection. b) Error map created by a faulty injection. c) Simulation of a faulty aspiration. b) Error map created by a faulty aspiration.

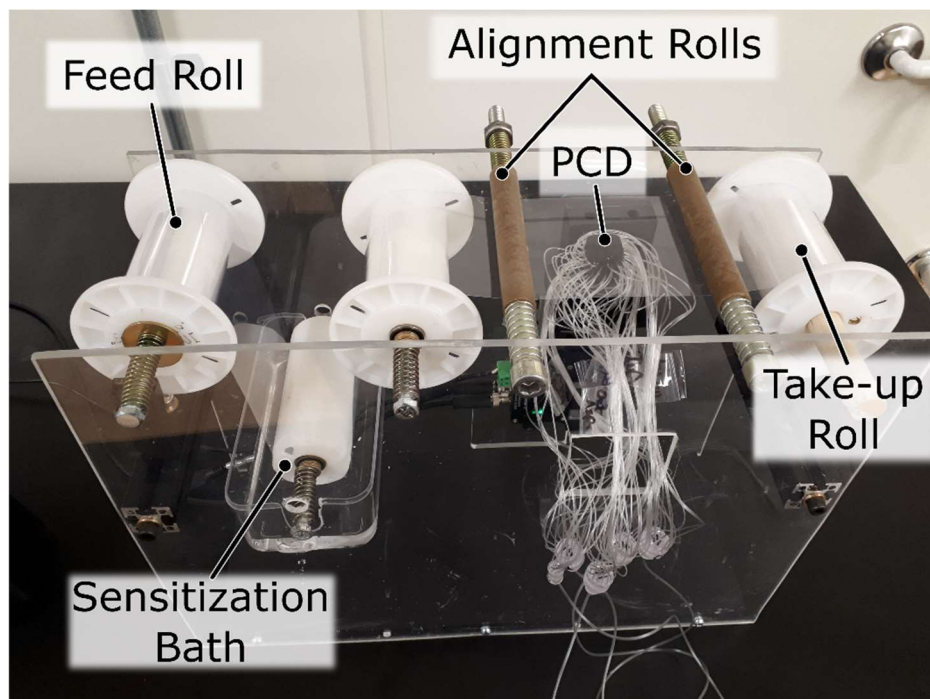


Fig. S6. Roll-to-roll custom setup for PCD integration.

2. Transport analytics

2.1 Transport model

Convective transport in the microfluidic pixel can easily be determined using Hele-Shaw formalism⁹⁰. We can show that the flow generated by the array of apertures is equivalent to the product of a 2D electric field generated by an infinite array of point sources, multiplied by a parabolic flow in the vertical direction¹³². Once the flow profile is known, we can obtain the concentration profile by solving the 2D convection-diffusion equation.

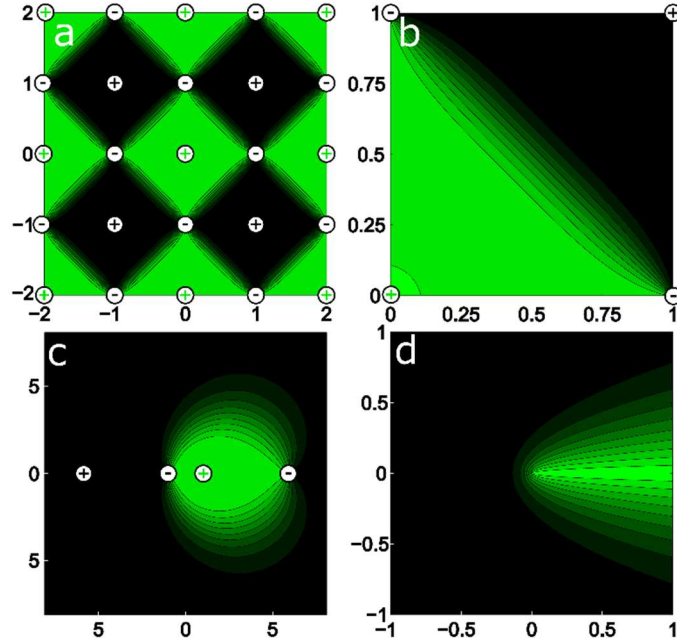


Fig. S7. Analytical model of convection-diffusion in a PCD (a) Concentration map of a PCD comprised of an infinite number of apertures. (b) Simplification of the problem into a quarter of a pixel using the problem symmetries. (c) The complex upper plain domain where the quarter pixel is unfolded on the real axis of the complex plane using a Schwarz-Christoffel transformation. (d) The semi-infinite obstacle domain obtained using the streamline coordinate transformation.

Since the PCD is periodic and using the problem symmetries, the PCD (Fig. S7a) can be simplified to a domain consisting of a unit square with unit aspirations in two opposite corners and unit injection in the other two (Fig. S7b). One of the injection apertures has a fixed concentration of one while the other has null concentration. The edges of the square represent symmetry conditions for both the flow and concentration profiles. The convection-diffusion equation in this geometry takes quite a complicated form, but we can simplify the problem using conformal transforms, following previous work by our group⁹². In this case we use a two-step process, first going from the pixel geometry to an unconfined flow using the Schwarz-Christoffel transformation for a square¹³³ (Fig. S7).

$$w = \text{SN}(z) \quad (\text{S1})$$

where $z = x + yi$ is the pixel domain, $w = u + vi$ is the unwrapped domain and $\text{SN}(z)$ is the Jacobi elliptic function. In this open geometry, alternating injections and aspirations are placed at the image of the square's vertices, namely $u = \pm 1$ and $u = \pm m^{-0.5}$, where $m \approx 0.02943$ (Fig. S7c).

From this geometry, we can then go to the streamline coordinate domain using the complex potential

$$\Phi = \log(w - 1) + \log(w + 1) + \log\left(w + m^{-\frac{1}{2}}\right) - \log\left(w - m^{-\frac{1}{2}}\right) \quad (\text{S2})$$

In the streamline coordinate domain (Fig. S7d), the problem is equivalent to one of straight flow around semi-infinite obstacles, and we can show that the solution can be obtained by using a piecewise assembly of the concentration around a semi-infinite absorber^{92,94}.

The solution thus obtained is

$$c = \begin{cases} 0.5(1 - \operatorname{erf}|\operatorname{Im}\sqrt{\operatorname{Pe}(\Phi - \Phi_0)}|), & y < 1 - x \\ 0.5(1 + \operatorname{erf}|\operatorname{Im}\sqrt{\operatorname{Pe}(\Phi - \Phi_0)}|), & y \geq 1 - x \end{cases} \quad (\text{S3})$$

where $\operatorname{Pe} = Q_0/2\pi GD$ is the ratio of diffusive to convective time scales, Q_0 is the injection flow rate of an aperture, G is the gap between the PCD and the surface, and D is the diffusion coefficient. By mirroring this solution with the edges' symmetry conditions, we get the profile for the entire microfluidic pixel array (Fig. S7a). This solution presupposes an infinite display, and pixels at the border of the PCD will inherently be distorted due to edge effects. However, experimental result shows that it mainly affects the first layer of pixels. While the concentration map of a square pixel was generated here, a similar method can be applied to triangular or hexagonal pixels. **Fig. S8** presents a comparison between analytical concentration maps and experimental images at equal Péclet Number.

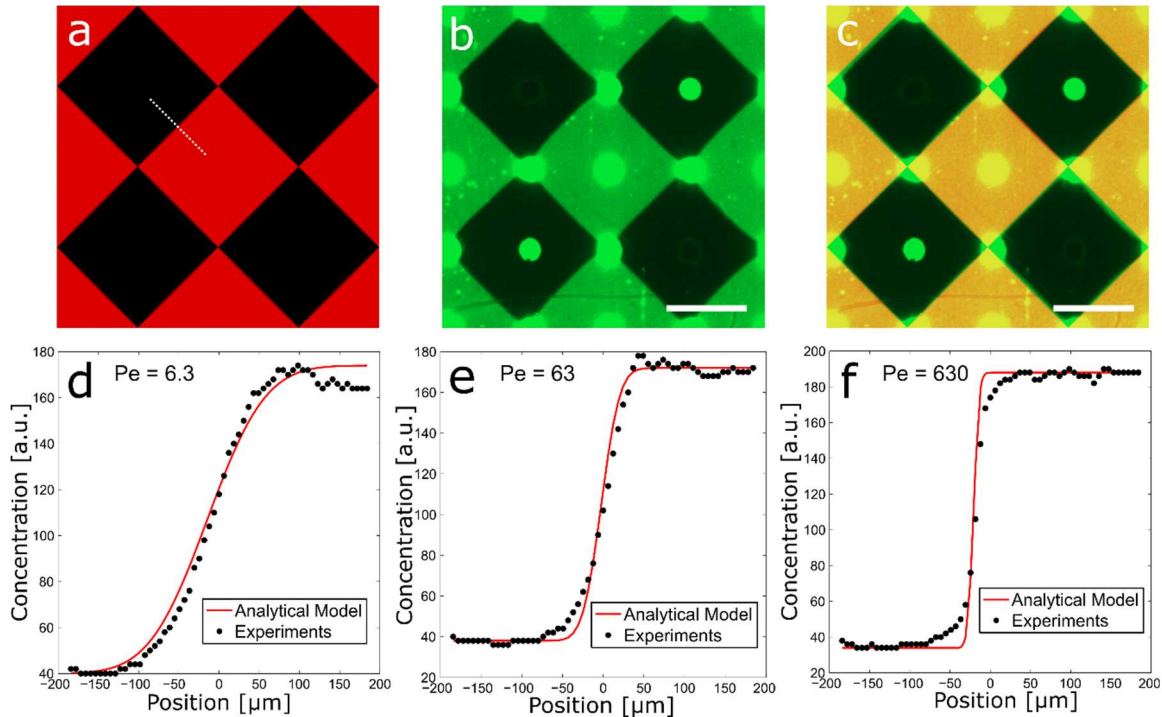


Fig. S8. Comparison between the analytical model and experimental data. (a) Analytical concentration map of a PCD for $\operatorname{Pe} = 630$. (b) Experimental concentration map of PCD for a $\operatorname{Pe} = 630$. Scale bar represents $500 \mu\text{m}$. (c) Overlay of the analytical and the experimental concentration map. Comparison of the concentration between the analytical model and the experiments at the interface between two pixels on the white dashed line from (a) for (d) $\operatorname{Pe} = 6.3$, (e) $\operatorname{Pe} = 63$, (f) $\operatorname{Pe} = 630$.

2.2 Details on Schwarz-Christoffel transformation

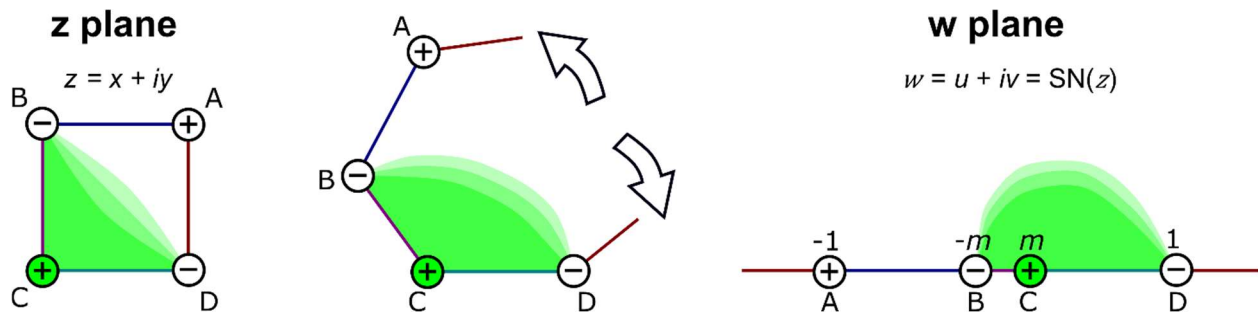


Fig. S9. From the pixel domain to a line of apertures. Using the Schwarz-Christoffel transformation for a square, the pixel domain (z plane) can be unfolded to a line of apertures (w plane) using the Jacobi elliptic function¹³³. The inside of the pixel is mapped on the complex upper plane. The vertices of the unit square in the z plane are transformed to the u axis at $u = \pm 1$ and $u = \pm m^{-0.5}$, where $m \approx 0.02943$. The transformation opens the pixel in the A-D segment and unfolds the pixel on the u axis.

3. PCD stability analysis

3.1 Stability analysis overview

Due to its architecture comprised of several manifolds and parallel channels, the PCDs will be subject to flow rate mismatch. Fabrication errors, but also partial clogging during operation and bubble trapped in the systems will all add-up creating flow rate variations between the channels. The following analysis was made to test the viability and robustness of PCDs in real life, in a context with fabrication errors and channel clogging. It also aims at giving insight on fabrication tolerance required to fabricate PCDs with high yield.

The stability analysis of the PCD was based on Monte-Carlo method¹¹⁸ and 2D finite element simulations. To study the effect of the flow rate errors, PCDs where every aperture has a stochastic error between a certain limit were simulated. The limit on flow rate errors was changed from [-5%, 5%] to [-75% 75%] to represent the effect of different fabrication tolerance (Fig. S10a). A thousand simulations were made for every condition. Multiple metrics were used for the analysis. The first one is the standard deviation of the pixels area which serve as a quantitative measurement of the pixel's deformation due to errors. The second metric is a usability threshold. It is defined as such as if the middle 60% of the microfluidic pixels area is unaffected by errors and deformation, the pixel is usable. Error heatmaps presenting the error distribution were also made (more details in the next section: Stability analysis visual protocol).

PCDs exhibited a low propagation of errors and a high stability, as stochastic errors of up to 30% on the flow rate leads to a relative standard deviation of approximately 10% on the microfluidic pixels areas for both a square-pixel and triangle-pixel PCD (Fig. S10c). Furthermore, errors on the flow rate of up to 20% lead to more than 97% of pixels respecting the usability threshold (Fig. S10d). The error heatmap (Fig. S10b) shows that errors are always located at the border between pixels. In other words, the effect of flow rate errors is a small shift in the microfluidic pixel positions. We found that the relative standard deviation of pixels area follows a quadratic function of the limit on the flow rate error.

Using the same method, the effect of the number of apertures on its stability was also measured. The bound on the flow rate errors was kept constant, but the number of apertures of the PCD was varied between 25 and 361 (Fig. S10e). The results show that the number of apertures has no significant effect on the stability of the PCD. These results are in agreement with the idea that the PCD is based on the periodicity, and thus its size have no effect on its stability. It confirms that large-scale PCDs with hundreds of apertures can be fabricated.

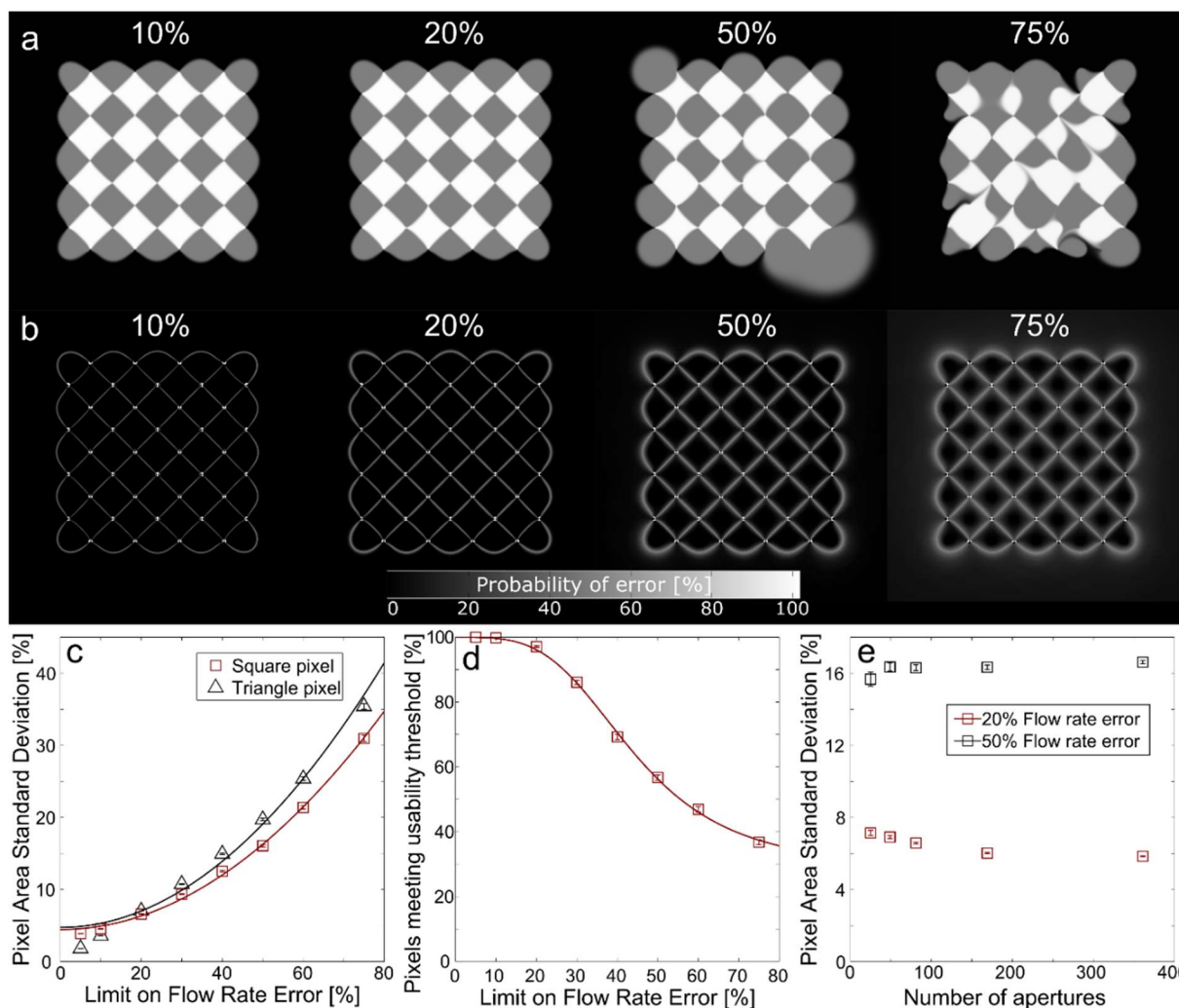


Fig. S10. Pixelated chemical display stability analysis. a) Examples of simulation results obtained for limits on the stochastic flow rate error between 10% and 75%. Figures were chosen to represent the typical result. b) Error heatmap for an 81-aperture square pixels PCD with limits on the flow rate error between 10% and 75%. Heatmaps were generated from 1000 simulations for all cases. White (255) represents a 100% probability of errors and black (0) represents 0% probability of errors. These heatmaps show that the errors are located at the border between pixels. c) Plot of the microfluidic pixel area relative standard deviation as a function of the limit on the flow rate error for an 81-aperture square pixel and a 92-aperture triangle-pixel PCD. For both the square-pixel and triangle-pixel PCD, the pixel area standard deviation closely follows a quadratic function. d) Proportion of microfluidic pixels respecting the usability threshold as a function of the limit on the flow rate error for an 81-aperture square-pixel PCD. As expected for a pass-fail test, the ratio of pixels meeting the threshold follows a logistic curve. Pixel meeting threshold = $100 - 72 / (1 + 0.023\varepsilon^{-3.6})$, where ε is the bound on flow rate errors. e) Plot of standard deviation of microfluidic pixels area as a function of the number of apertures of a square-pixel PCD for a limit on the flow rate error of 20% and 50%. Results c-e are based on 1000 simulations per conditions. Error bars are the bilateral 95% confidence interval.

3.2 Stability analysis visual protocol

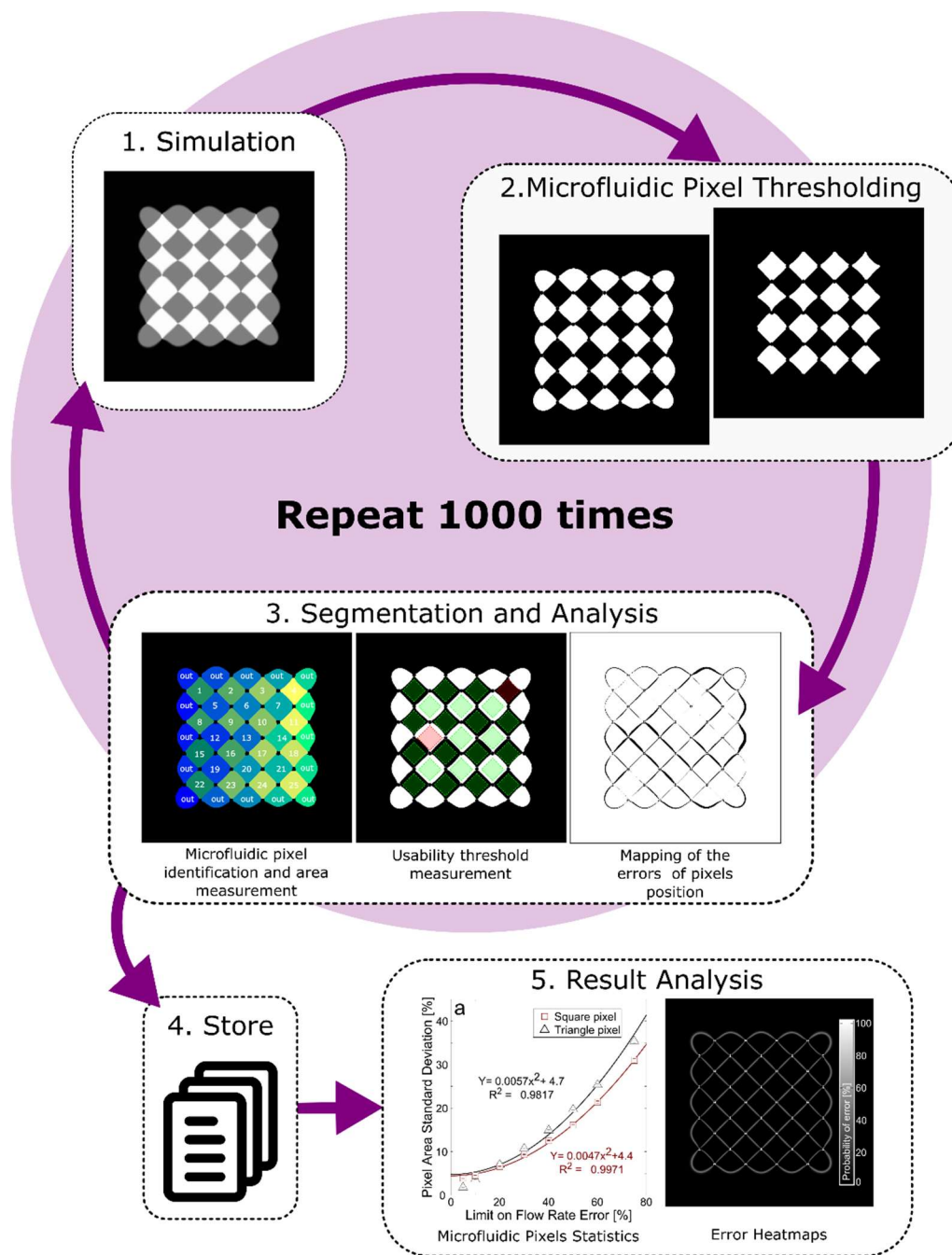


Fig. S11. PCD stability analysis methodology. (1) PCDs with stochastic bounded error on the flow rate were simulated using 2D finite element simulations. (2) Image resulting from simulation result were thresholded to isolate the different pixels. (3) Microfluidic pixels were segmented from black and white images. Microfluidic pixels were enumerated and data such as position and areas were measured. The usability threshold and the mapping of the error compared to a perfect simulation was calculated. (4) These results and the original simulation result were stored. (5) After generating more than a thousand simulations for each case, the results were analyzed. The relative standard deviation on pixel area, the usability threshold probability, and the error heatmaps were calculated.

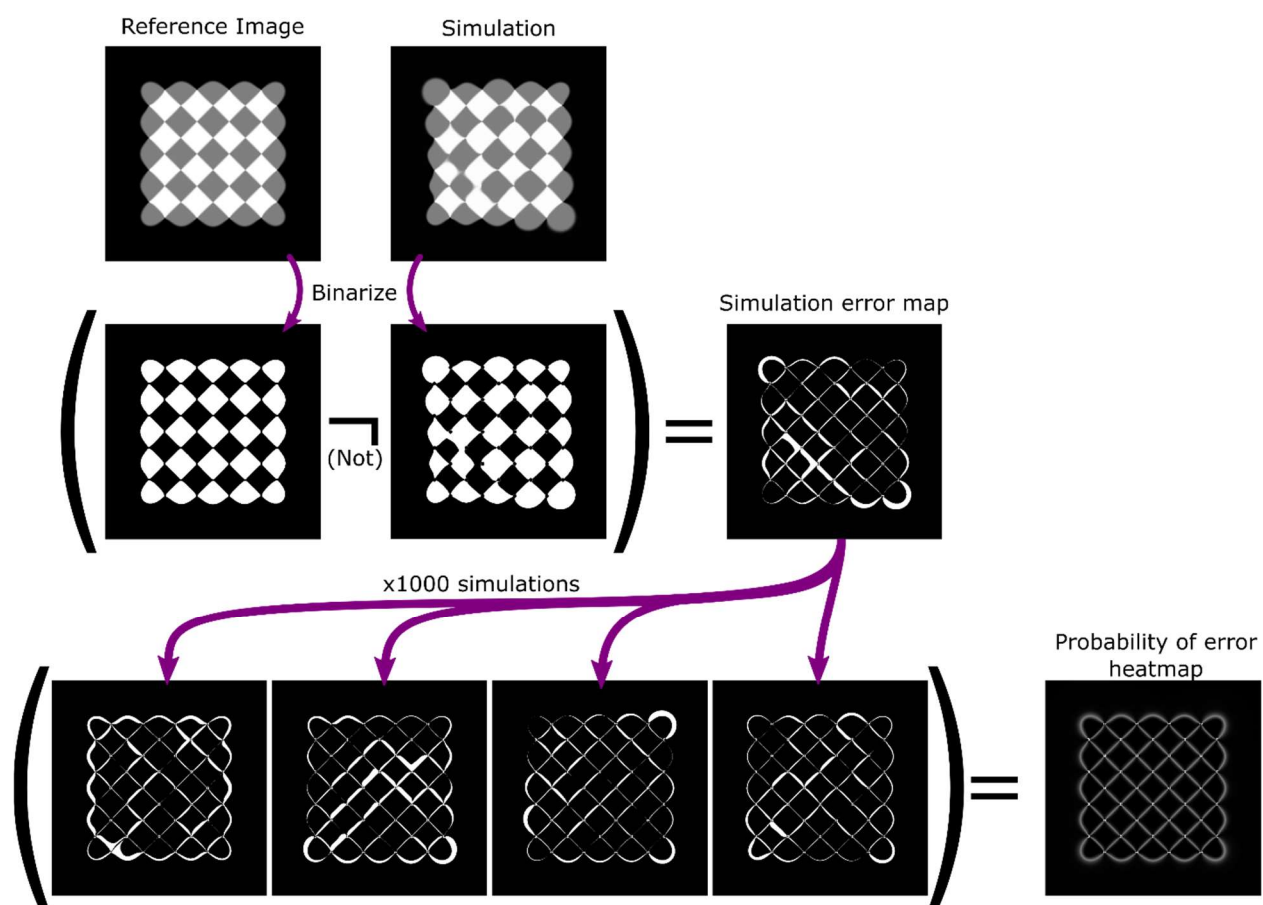


Fig. S12. Error heatmap methodology. Binarized simulation images are compared with a reference binarized image to generate error map of the simulations. The percentage of error maps containing an error is calculated for every pixel of the error heatmap.

3.3 Stability analysis detailed results

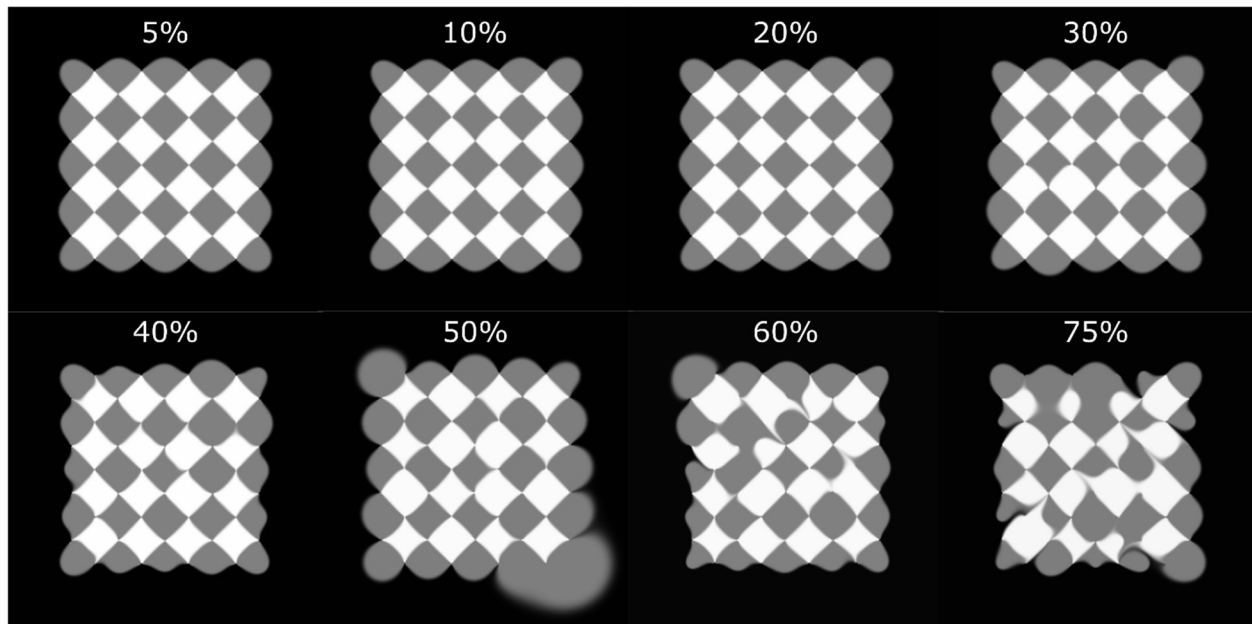


Fig. S13. Examples of results obtained for different bounds on the stochastic error flow rate for an 81-aperture square-pixel PCD. Images were chosen to represent the typical average result. However, because of the randomness generated by the stochastic errors on the 81 apertures, a single simulation can't represent all the simulations of a condition.

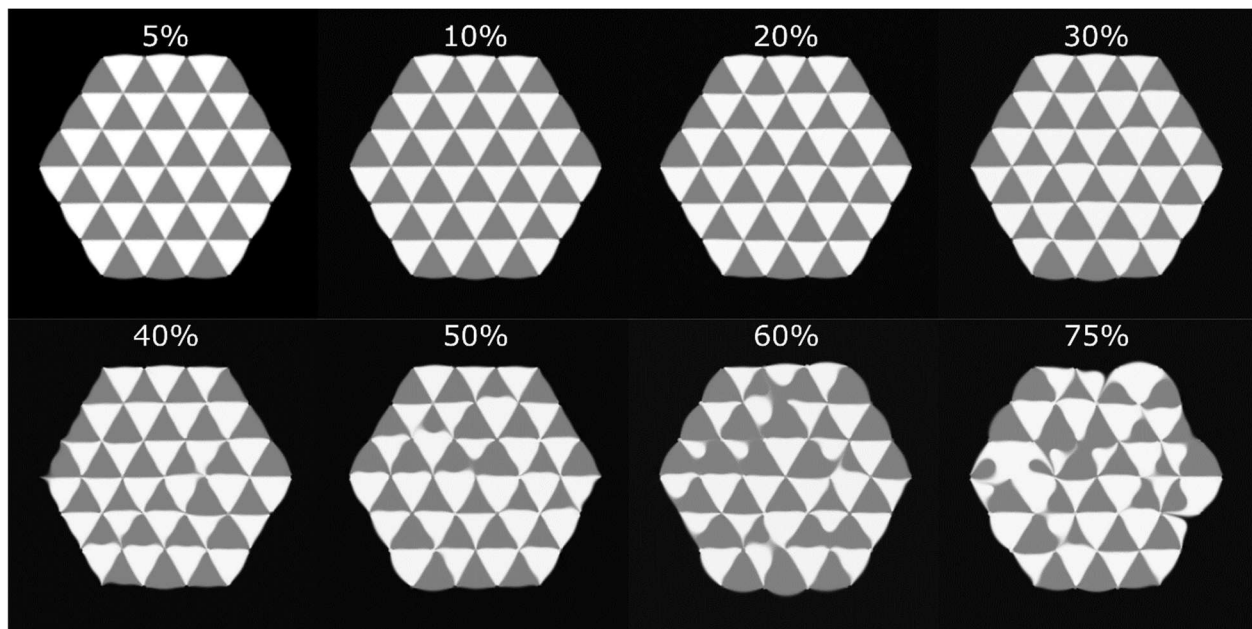


Fig. S14. Examples of results obtained for different bounds on the stochastic error flow rate for a 92-aperture triangle-pixel PCD. Images were chosen to represent the typical average simulation for every condition.

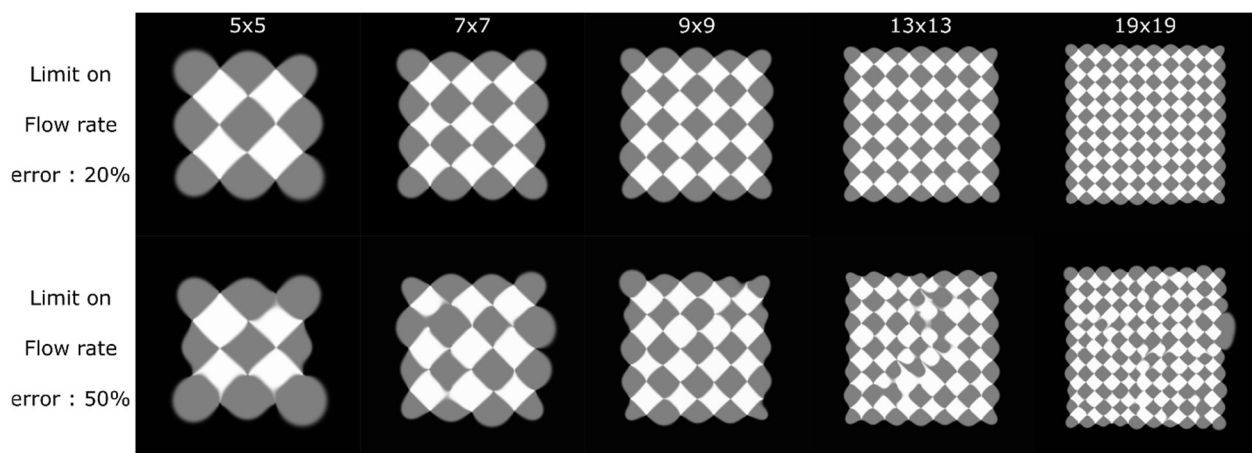


Fig. S15. Examples of results obtained for different size of PCDs with bounds on the stochastic error flow rate of 20% and 50%. Images were chosen to represent the typical average result.

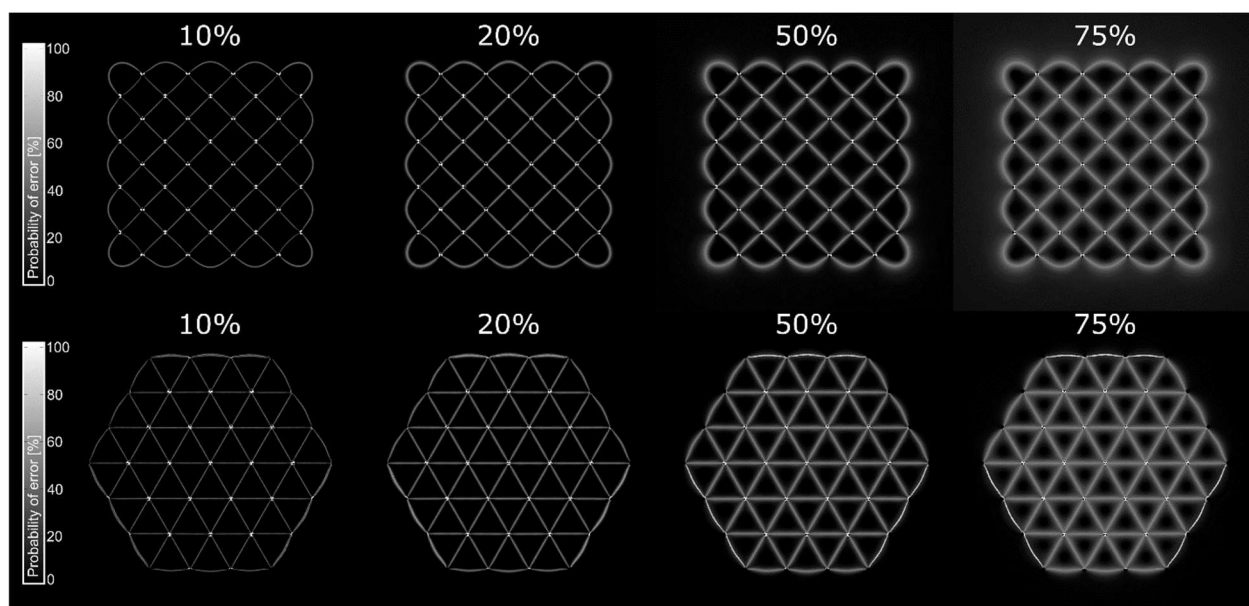


Fig. S16. Errors heatmaps for different limits on the flow rate error for a square-pixel and triangle-pixel PCD. Heatmaps were generated from 1000 simulations for all cases. White (255) represents 100% chance of errors and black (0) represents 0% chance of errors.

4. Reagent switching time

4.1 Reagent switching model

The PCD, being based on continuous convection, has the potential to allow fast switching time between reagents. It also removes the need for lengthy washing steps normally required working with wells and pipette-based liquid handling automation. For an PCD, the media change is mainly limited by the Taylor-Aris Dispersion taking place from the valve to the aperture of the PCD. We assume here a reagent of concentration equal to one and a reagent of null concentration. After a switch between the two reagents, the concentration of reagent in a channel at a distance L from a valve and of radius r is⁹¹:

$$c(L, t) = \frac{1}{2} \left(1 + \operatorname{Erf} \frac{L - \frac{Qt}{\pi r^2}}{2\sqrt{t * D_{eff}}} \right) \quad (\text{S4})$$

where Q is the flow rate, and D_{eff} is the Taylor-Aris effective diffusion coefficient. D_{eff} , for a circular channel of radius r , is defined as¹¹⁷:

$$D_{eff} = \left(1 + \frac{Q^2}{48\pi^2 r^2 D^2} \right) D \quad (\text{S5})$$

From equation S4, we can find that, for a PCD, the switching time to change from a concentration $1 - C_{switch}$ to C_{switch} is defined by:

$$t_{switch} = \frac{4\pi^2 r^4 \sqrt{D_{eff}^2 (\operatorname{Erf}^{-1}(2C_{switch} - 1))^4 + \frac{LQ}{\pi r^2} D_{eff} (\operatorname{Erf}^{-1}(2C_{switch} - 1))^2}}{Q^2} \quad (\text{S6})$$

The most efficient way to decrease the switching time is to diminish the radius of the channels¹¹⁷. Increasing the flow rate and decreasing the distance between the valves and the apertures has also an effect.

As an example, a PCD with a flow rate of 100 nL/s per aperture using tubes with a diameter of 250 μm and a length of 10 cm takes 40 s to change a reagent from a 1% to a 99% concentration. The same PCD, if using tubes of smaller diameter of 100 μm would take 6 s to change a reagent (from a 1% to a 99% concentration).

Next section presents a comparison between the analytical transition time and the experimental results.

4.2 Characterisation of experimental reagent switching time

The experimental switching time was measured for a microfluidic pixel in the experiment of Fig. 4. and Supplementary video 1.

Fig. S17 present the concentration curve of a microfluidic pixel as the PCD change from the “P” state to the “O” state (see also supplementary video 1 or Fig. S18). This pixel was chosen because it is individually connected to one of the pumps, which simplify the analysis. The theoretical model considers the switching in a channel with a constant diameter and flow rate, which prevent us from directly comparing the model with the concentration change in most pixels (most valves are connected to injections through manifolds).

The result shows us a switching time which is in the same order of magnitude as the model. The model predicted a switching time (from a 5% to a 95% concentration) of 16.4s using the experiment parameters. The experimental data estimate the switching to 13s. This analysis only gives information on the analyzed pixel. Other pixels connected differently (in groups through manifold) have different switching time. However, it confirms that the switching time is mainly limited by the Taylor-Aris dispersion.

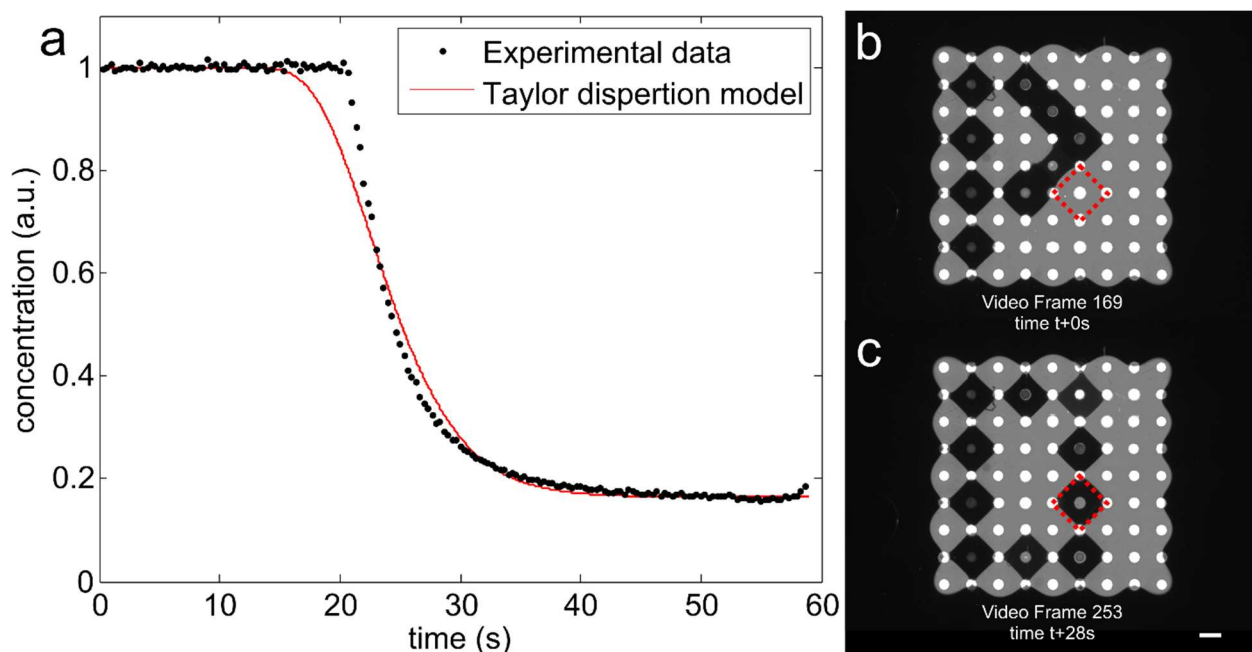


Fig. S17. Experimental reagent switching time in a pixel. a) Concentration curve of a microfluidic pixel between the PCD state “P” and “O”, in comparison with the model. The curve was made from the frames of supplementary video 1. The concentration is the median of 25 neighbors pixels. b) PCD in the state “P”. The red square represents the pixel for which the concentration curve from a) was made. d) PCD in the state “O”. Scale bar represents 500 μm .

4.3 Reagent switching video frames

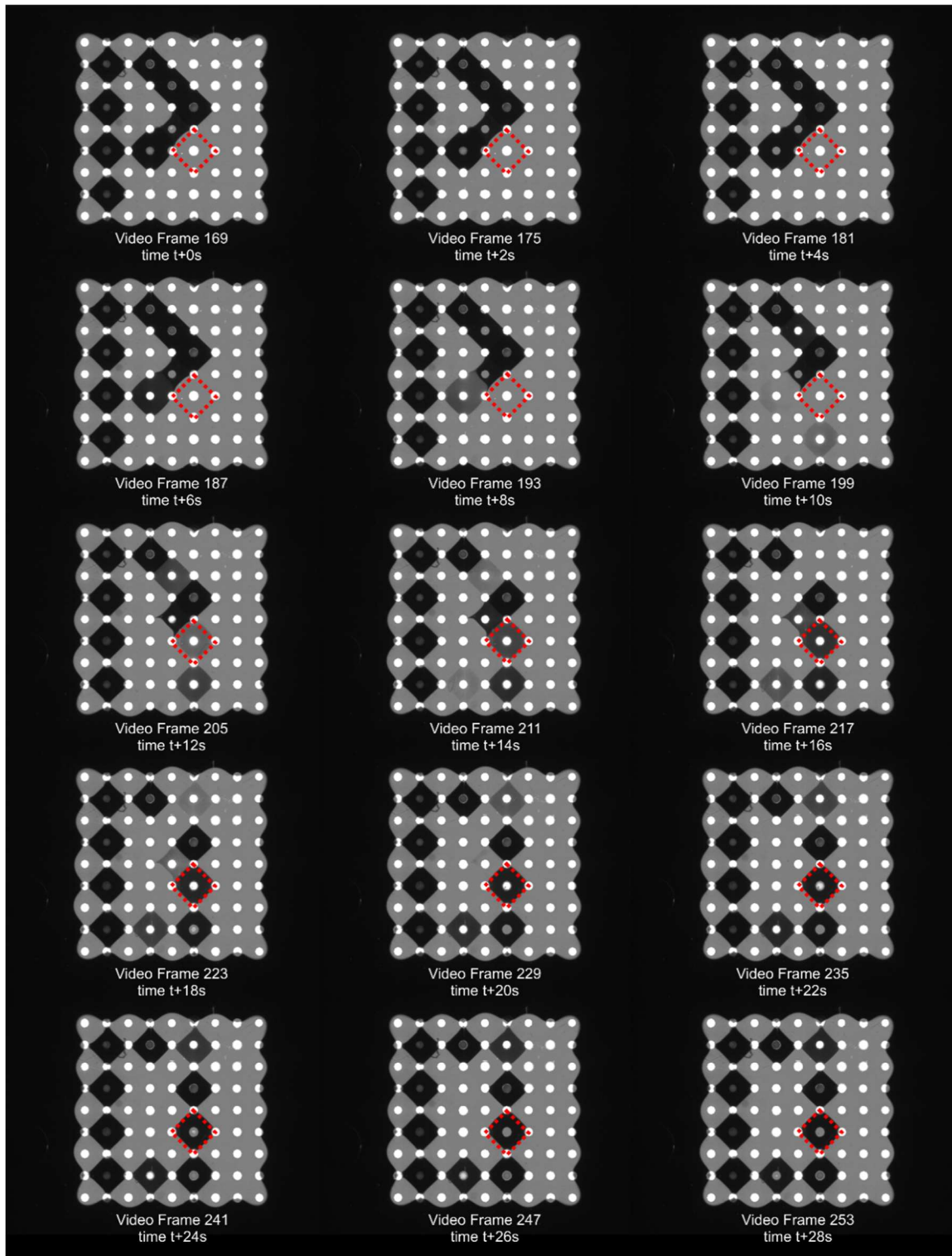


Fig. S18. A set of *supplementary video 1* frames that show the PCD switching from state “P” to “O”. The red square is the pixel analysed in the previous section.

APPENDIX F LIST OF CONTRIBUTION

Articles:

1. Brimmo, A., **Goyette, P.**, Alnemari, R., Gervais, T. & Qasaimeh, M. A. 3D Printed Microfluidic Probes. *Sci. Rep.* **8**, 10995 (2018). (Published as co-first author)
2. **Goyette, P.-A.** *et al.* Microfluidic multipoles theory and applications. *Nat. Commun.* **10**, 1781 (2019). (Published as co-first author)
3. **Goyette, P.**, Boulais, É., Tremblay, M. & Gervais, T. Pixel-based open-space microfluidics for versatile surface processing. *Proc. Natl. Acad. Sci.* **118**, e2019248118 (2021).

Oral Presentations:

1. **Goyette, P-A.** Gervais, T. *Pixelated Chemical Display: Toward massively parallel dynamic surface processing*. Oral presentation for microTAS 2019, Basel, Switzerland
2. **Goyette, P.**, Boulais E., Normandeau F., Laberge, G., Juncker, D., Gervais T. *Reconfigurable multipolar open space microfluidics*. Oral presentation for microTAS 2018, Kaohsiung, Taiwan.

Scientific posters:

1. **Goyette, P-A.** *Pixelated chemical display for dry surface patterning in industrial roll-to-roll processes*. Poster for microTAS 2020 (Online).
2. **Goyette, P.**, Gervais T. *3D printed microfluidic probes and streaming displays*. Poster for microTAS 2018, Kaohsiung, Taiwan.
3. Boulais E., **Goyette, P.**, Laberge, G., Gervais T. *Understanding convection-diffusion in open-space microfluidics via conformal mapping*. Poster for microTAS 2018, Kaohsiung, Taiwan.